THEORETICAL STUDY OF CLUSTER EMISSION AND FISSION DYNAMICS USING BINARY FRAGMENTATION APPROACH

A THESIS

Submitted in the partial fulfillment of the requirement

for the award of degree of

DOCTOR OF PHILOSOPHY

under the guidance of

Dr. Manoj K. Sharma
(Professor)

by

Kanishka Sharma

(Regn. No: 901412002)

School of Physics and Materials Science

Thapar Institute of Engineering and Technology

Patiala-147004, INDIA

AUGUST, 2019

Dedicated to

The Supreme Divine

and My Family

who has been my strongest support and always been there for me

CERTIFICATE

This is to certify that the thesis entitled "**Theoretical study of cluster emission and fission dynamics using Binary Fragmentation Approach**" being submitted by **Kanishka Sharma** for the fulfillment of the requirements for the award of Degree of Doctor of Philosophy in the School of Physics and Materials Science, Thapar Institute of Engineering and Technology, Patiala, is a record of the candidate's own work carried out by her under my supervision. The matter presented in this thesis has not been submitted in part or full for the award of any degree in any university or institute.

Supervisor

16.12.19

Dr. Manoj K. Sharma

Professor

School of Physics and Materials Science

Thapar Institute of Engineering and Technology (TIET)

Patiala- 147004

Punjab (India)

Acknowledgements

"Real life isn't always going to be perfect or go our way, but the recurring acknowledgement of what and who is involved in our lives can help us not only to survive but surmount our difficulties."

All praises in the name of GOD, the Most Gracious and the Most Merciful, and His blessings for the completion of this thesis. I thank God for all the opportunities, trials and strength that He has showered on me to accomplish the objectives of this thesis. He granted me the serenity to accept the things I cannot change, the courage to change the things I can, and the wisdom to know the difference. My humblest gratitude to the Divine who always helped me to stay positive throughout this journey. I wish to express my sincere appreciation to those who have contributed to this thesis and supported me in one way or the other during this amazing journey.

First of all, it is difficult to overstate my gratitude to my PhD supervisor, Prof. Manoj Kumar Sharma. With his enthusiasm, his inspiration, and his great efforts to explain things clearly and simply, I have earned a great deal of scientific knowledge which has shaped my research skills and encouraged me to pursue in research field. I have been extremely lucky to have a supervisor who cared so much about my work, and who responded to my questions and queries so promptly. His careful editing contributed enormously to the production of this thesis. Throughout my thesis-writing period, he provided encouragement, sound advice, good teaching, and lots of good ideas. His creativity and wisdom are inspirational. It is matter of pride and pleasure to have worked under his generous and able supervision. I hope that I could be as lively, enthusiastic, and energetic as him and I wish to make him proud through my future work. A special word of thanks to Mrs. Sonam Sharma for her motherly affection and care.

I gratefully appreciate the collaborative effort of Late Prof. Raj K. Gupta from Physics Department, Panjab University, Chandigarh who provided me the great opportunity to work with him. It is fortunate enough to work with him. I have reserved my sincere gratitude for Professor Gupta for his invaluable insights and suggestions in my research

work. I really appreciate his willingness to meet me at short notice every time and going through several drafts of my research articles. He was, and will be the greatest source of inspiration for me. Thank you very much Sir, for helping me with everything; it had been an honor to work with you.

I express my sincere thanks to Prof. O. P. Pandey, Head, School of Physics and Materials Science, TIET, Patiala and Ex-TIET Dean, Research and Sponsored Projects, for providing me the necessary facilities in the department and for his affectionate behavior throughout my research period. I thank him for providing me the fellowship as a Teaching Associate well in time. My advisory doctoral committee members Dr. Alka Upadhyay, Dr. Soumendu Jana and Dr. A.K. Lal deserve many thanks for their useful suggestions during the progress report presentations. I am also extremely thankful to Dr. Debabrata Deb and Dr. Bhaskar Chandra Mohanty for helping me to curb the plagiarism. My sincere thanks also goes to Prof. Rafat Siddique, present Dean, Research and Sponsored Projects, TIET, Patiala for providing the grants to attend the conferences and necessary resources to accomplish my research work. Special thanks to Prof. Kulvir Singh for his encouragement and constant moral support throughout my PhD. I also wish to express my gratitude to all the faculty and staff of the School for their help and kind support.

I deeply appreciate the moral and academic support of Dr. Gudveen Sawhney in the accomplishment of the objectives of this thesis. Her sweet and polite words made me feel relaxed every time when I got stuck in any research problem. Thank you Di for all your help and support. I will take all your professional advices with me. I am also grateful to my lab seniors Dr. Manpreet Kaur, Dr. Gurvinder Kaur, Dr. Kirandeep Sandhu, Dr. Mahesh Kumar Sharma, Dr. Manjeet Singh Gautam and Ms. Amandeep Kaur for introducing me to my research field in nuclear physics. My special thanks to Dr. Rajni for her love and affection as an elder sister. From the bottom of my heart, I thank you Di for always motivating me throughout this journey. I am thankful to you for sharing such a wonderful bonding with me.

This acknowledgement will never be complete without the special mention of my fellow

lab mates Gurjit Kaur, Ishita Sharma, Nitin Sharma and Vishal Parmar for their cooperation and jovial company. Words cannot express how grateful I am to three of my best friends Neha, Shivani and Aman for their indispensable support. Thanks for sharing an awesome and crazy friendship that always makes me smile and never let me down. You were always there to hear me whether I was cracking a stupid joke, complaining about life or just blabbering. We have been sharing a strong bond that nothing can make untie. I am extremely thankful to my very good friend Mr. Pradeep Kumar Singh for constantly supporting me during this amazing journey. You motivated me during the difficult times when I needed words of encouragement. Thanks for being a non-judgmental listener and a true friend. Thank you for always being my biggest support. I may not be able to list all the names running in my mind, but I thank all my friends Pallavi, Saloni, Sangeeta, Navjot Kaur Virk, Deepshikha, Neeraj, Kundan, Shoaib, Jagroop, Jaspreet, Bharti, Raveena, Chhavi, Nikhil, Vijay and Pulak for having the doors open to any of my questions and problems, for invaluable help and the jovial company.

Finally, but by no means least, I would love to acknowledge my family for almost unbelievable support. I concede my heartiest admiration and gratitude for my parents (Mr. Sanjiv Sharma and Mrs. Savita Sharma) for the countless blessings. They always keep me in their prayers and always let me chase my dreams whatever they may be. Thank you for helping me to shape my life with positivity and passion. Please accept my heartfelt thanks for the best gift you could ever have given me: a wonderful education. I am who I am today because of your effort, guidance, and support. I couldn't have done it without you. Thank you for your endurance and for never giving up on me. I don't think I can ever repay my parents but I think "What you are is Parents' gift to you, what you become is your gift to Parents". They are the most important people in my world and I dedicate this thesis to them. A special note of thanks to my younger siblings (Smriti and Shivansh) for being my best friends since childhood. Whether I am just looking for some company or need a friend to talk to, I know that there is always someone there for me. Thank you both for being you, and thank you for giving me the privilege of being your elder sister

no matter how mad you guys make me. You always gave me the gift of smile, h encouragement in the difficult times. Thank you for your support and cordiality. to have you both! My thanks also goes to my Bua Ms. Deepshikha and Uncle M Bedi for their innumerable blessings. I would also love to thank my grandmother paternal uncle for their love and affection.

The financial assistance from Thapar Institute of Engineering and Technology in the form of Teaching Associate is gratefully acknowledged.

Patiala

August, 2019.

(Kanishka Sharma)

List of Publications

I. International Journals:

1. Fragmentation analysis and α-decay half-lives of trans-Sn nuclei,
   Kanishka Sharma, and Manoj K. Sharma, Nucl. Phys. A **986**, 1-17 (2019).

2. Analysis of competing ground state channels observed in decay of Cm isotopes,
   Kanishka Sharma, and Manoj K. Sharma, Int. J. Mod. Phys. E (IJMPE) **28**, 7 (2019).

3. Fission dynamics and related aspects of $^{181}Re^{*}$ nucleus formed in ^{12}C induced reaction,
   Kanishka Sharma, and Manoj K. Sharma, Brazilian Journal of Physics **49**, 887 (2019).

4. Collective clusterization approach to investigate the relevance of deformation effects in Sn-radioactivity,
   Kanishka Sharma, Gudveen Sawhney, Manoj K. Sharma, and Raj K. Gupta, Eur. Phys. J. A **55**, 30 (2019).

5. Decay of Plutonium isotopes via spontaneous and heavy-ion induced fission paths,
   Kanishka Sharma, Gudveen Sawhney, Manoj K. Sharma, and Raj K. Gupta, Nucl. Phys. A **972**, 1-17 (2018).

6. Study of spontaneous fission and competing ground state decay modes of actinide and trans-actinide nuclei,

Kanishka Sharma, Gudveen Sawhney, and Manoj K. Sharma, Phys. Rev. C **96**, 054307 (2017).

7. Effect of deformations and orientations in ^{100}Sn daughter radioactivity,
   Gudveen Sawhney, **Kanishka Sharma**, Manoj K. Sharma, and Raj K. Gupta, EPJ Web of Conferences **117**, 04013 (2016).

8. Dynamics of $^{47}V^{*}$ formed in ^{20}Ne+^{27}Al reaction in view of fusion fission and DIC mechanism,
   Neha Grover, **Kanishka Sharma**, and Manoj K. Sharma, Eur. Phys. J. A **53**, 239 (2017) [Not part of this thesis].

9. Analysis of various decay modes of radioactive nucleus ^{242}Cm,
   Kanishka Sharma, and Manoj K. Sharma, Submitted in Bulletin of the Russian Academy of Sciences: Physics.

II. International and National Conferences, Symposiums and Workshops:

(a) **International:**

1. Analysis of ER and fission in decay of ^{210}Rn formed in ^{16}O + ^{194}Pt reaction, Manpreet Kaur, **Kanishka Sharma**, and Manoj K. Sharma, DAE Symp. on Nucl. Phys. BARC (Mumbai), Vol. **58**, 440 (2013).

2. Effect of deformations and orientations in ^{100}Sn daughter radioactivity, Gudveen Sawhney, **Kanishka Sharma**, Manoj K. Sharma, and Raj K. Gupta, 12th International Conference on Nucleus-Nucleus Collisions, Catania (Italy), **C-15**-06-21.1 (2015).

3. Analysis of various emission modes in the ground state decay of ^{240}Pu nucleus, **Kanishka Sharma**, Gudveen Sawhney, and Manoj K. Sharma, International conference in nuclear physics with energetic heavy ion beams, Panjab University (Chandigarh), Page **84**, (2017).

4. Fission fragment distribution of $^{181}Re^{*}$ nucleus formed via ^{12}C induced reaction, **Kanishka Sharma**, Neha Grover, and Manoj K. Sharma, DAE Symp. on Nucl. Phys. BARC (Mumbai), Vol. **63**, 400 (2018).

5. Analysis of various decay modes of radioactive nucleus ^{242}Cm, **Kanishka Sharma**, and Manoj K. Sharma, Nucleus-2019, JINR, Dubna (Russia), Sec. **4**, 283 (2019).

(a) **National:**

1. Analysis of Fission versus Quasi-Fission in $^{16}O+^{194}$ Pt reaction, **Kanishka Sharma**, Manpreet Kaur and Manoj K. Sharma, National conference on emerging challenges in nuclear and many body physics (ECNMP), Jammu University (Jammu) 2014.

2. Dynamics of ^{92}Zr and $^{108,110}Sn$ nuclei formed in $^{16,18}O$-induced reactions, Rajni, **Kanishka Sharma**, Gurvinder Kaur, and Manoj K. Sharma, DAE Symp. on Nucl. Phys., Banaras Hindu University (BHU), (Varanasi) , Vol. **59**, 562 (2014).

3. Cluster decay of various Gd isotopes from the trans-tin region, **Kanishka Sharma**, Gudveen Sawhney, Manoj K. Sharma, and Raj K. Gupta, DAE Symp. on Nucl. Phys., Sri Sathya Sai Institute of Higher Learning, Prasanthi Nilayam, (Andhra Pradesh), Vol. **60**, 176 (2015).

4. Fission decay analysis of ^{242}Pu using the clusterization process, **Kanishka Sharma**, Gudveen Sawhney, Manoj K. Sharma, and Raj K. Gupta, DAE Symp. on Nucl. Phys., Saha Institute of Nuclear Physics (SINP), Kolkata, (West Bengal), Vol. **61**, 372 (2016).

5. Alpha radioactivity of the A=110 isobars near N=Z line, **Kanishka Sharma**, Neha Grover, Kirandeep Sandhu, and Manoj K. Sharma, DAE Symp. on Nucl. Phys., Thapar Institute of Engineering and Technology, Patiala, (Punjab), Vol. **62**, 246 (2017).

Contents

List of Figures

List of Tables

Abstract

The principal objective of the present work is to explore the various ground state decay processes having different disintegration mechanisms on the basis of their structural properties. These radioactive decay modes include α-radioactivity, cluster emission, heavy particle decay and spontaneous fission of parent nuclei. The study has been carried out using the methodology of Preformed Cluster Model (PCM). Beside this, predictions on Sn-radioactivity and Heavy-Particle Radioactivity (HPR) have been made for the validation of the present calculations via future experiments. Furthermore, an extensive analysis on heavy-ion induced fission of heavy nuclei is carried out in view of their mass distribution and the cross-sectional analysis. The calculations of excited state decays are accomplished within the framework of Dynamical Cluster-decay Model (DCM), the extended version of PCM with temperature and ℓ-effects included. The role of center of mass energy, angular momentum, deformations and orientations is investigated comprehensively in order to gain the useful information on induced fission phenomenon. Additionally, a comprehensive analysis has been done so as to compare the ground state and excited state decay mechanisms in view of their respective structural and barrier profiles.

Chapter 1 begins with the explanation of the emergence of "Radioactivity" in research field. The physical interpretation of various radioactive decay processes such as α-decay, cluster radioactivity and spontaneous fission is described in this chapter. The favorable regions of the periodic table, which are most prominent for different kinds of radioactive decays are illustrated by depicting the island of stability. The applicability

of these decay modes in our daily life is described by considering examples of various radionuclides. Furthermore, an introduction to heavy-ion induced fission phenomenon is discussed in the same chapter. A brief discussion on deformations and orientation effects is presented along with the relevance and motivation of the work carried out in this thesis.

Chapter 2 provides the relevant information on the methodology used to fulfill the objectives of present work. Here, Preformed Cluster Model (PCM) has been described to study the ground state decay processes (i.e. α-decay, cluster and heavy-cluster radioactivity and spontaneous fission) and the Dynamical Cluster-decay Model (DCM) is explained in order to explore the induced decay process (i.e. heavy-ion induced fission). It is worth mentioning here that DCM is the extended version of PCM, with temperature and ℓ-effects included in it. Basically, both the PCM and DCM are based on the Quantum Mechanical Fragmentation Theory (QMFT), which deals with the two kinds of probabilities viz. preformation probability P_0 and penetration probability P. The deformation and orientation effects are appropriately included within this formalism. In comparison to statistical models (which apply different methodologies to treat different mechanisms), PCM and DCM considers all the decay phenomena on equal footing. Each emitting channel in the decay process is assumed to be preborn inside the parent nucleus and possesses an unique preformation probability. After the formation of a fragment along with the complementary daughter nucleus, the tunnelling process initiates, where the decaying products penetrate across the potential barrier before achieving scission configuration. Thus, with the help of preformation and penetration probabilities, the decay half-lives/emission times and the reaction cross-sections are determined and the corresponding expressions are elaborated in this chapter.

In **Chapter 3**, the triple α-decay chain $^{114}\mathrm{Ba} \xrightarrow{\alpha} {}^{110}\mathrm{Xe} \xrightarrow{\alpha} {}^{106}\mathrm{Te} \xrightarrow{\alpha} {}^{102}\mathrm{Sn}$ has been studied which gives three new α-emitters ^{114}Ba, ^{110}Xe and ^{106}Te. In order to explore the excited state α-decays, the dynamics of ^{58}Ni(^{58}Ni,2n) reaction forming $^{116}\mathrm{Ba}^*$ is studied

at the beam energy E_{Lab}=210 MeV. The half-lives of the nuclei formed in successive α-decay chain are calculated using Dynamical Cluster decay Model (DCM). In addition to this, the α-decay half-lives of some trans-Sn Te, I, Xe, Cs and Ba isotopes, lying near the super-allowed region of α-decay, have been addressed within PCM in view of ground state α-radioactivity. The role of various proximity potentials having different isospin dependence is investigated to extract the useful information about the barrier characteristics in decay of trans-Sn region nuclei. The preformation probability distribution, which gives an account of potential energy surfaces, is analyzed for the relative comparison of spontaneous and induced α-emission processes.

In **Chapter 4**, the role of deformations and orientations is studied in view of cluster decay of various radioactive nuclei leading to doubly magic ^{100}Sn or ^{132}Sn daughter nucleus, using the PCM. This model treats the cluster emission process via tunnelling across the potential barrier, the cluster/fragment being preformed with a relative probability P_0. With the incorporation of deformation and orientation effects, the fragmentation potential, the penetration path and related barrier characteristics get significantly modified, due to which both the preformation probability P_0 and penetrability P of the emitting cluster get influenced. The half-lives of the decaying clusters calculated using PCM are found out to be within the upper limits of the present experiments. The influence of deformations and orientations on Sn-radioactivity is also investigated in terms of barrier characteristics such as barrier modification, barrier height, etc. Moreover, the role of different nuclear proximity potentials, i.e., Prox77, Prox88 and Prox00, is analyzed in context of potential energy surfaces (PES) in the ground-state decay of parent nucleus. The behavior of PES is explored with, as well as without, including the shell corrections in the binding energies, which in turn help to explore the importance of doubly magic closed shell configuration of daughter and cluster nuclei. The possible role of higher order multipole deformations (i.e., upto β_{4i}) is also analyzed in view of the fragmentation path and barrier tunnelling characteristics.

In **Chapter 5**, PCM has been employed to carry out a comprehensive theoretical study on the decay paths of ground state actinide and trans actinide nuclei, specifically from ^{232}U to ^{264}Hs exhibiting the phenomenon of spontaneous fission (SF). This is an extension of earlier studies on alpha decay, exotic cluster emission and heavy particle radioactivity, where an effort is made to identify the most probable fragments in SF process. These observations in turn, could provide a testing ground for the future SF half-life measurements. In order to obtain a clear picture of the dynamics involved, the variation in fragmentation potential, preformation factor, and decay barrier height has been examined. The calculated potential energy surfaces (PES) show a change from a predominantly asymmetric fission to a symmetric fragmentation with the increase in the N/Z ratio of parent nuclei. In addition, an exclusive analysis of SF with alpha and other possible cluster emissions for the ^{232,234,236,238}U parents has been made in order to have better insight of nuclear structure and related dynamics. In other words, the comparative nature of alpha, cluster, heavy fragment and SF decay paths is analyzed in view of shell closure property of the decay fragments. Interestingly, the calculated decay half-lives for ^{82}Ge heavy cluster are in fact shown to lie within the limits of experiments, thereby presenting some exciting new possibilities which may be validated via future experiments.

In **Chapter 6**, the heavy ion induced fission of two heavy compound nuclear systems is investigated within the framework of Dynamical Cluster Model (DCM). Firstly, the fission of ^{181}Re* nucleus formed via ^{12}C+^{169}Tm reaction is studied at E_{Lab}=77-89 MeV within DCM for the choices of spherical as well as deformed fragments originated in binary decay channels of collective clusterization approach. The mass distribution of the compound nucleus ^{181}Re* is analyzed for both the choices and compared with the available data, and consequently the probable fission fragments are identified. The barrier height, barrier modification and barrier penetrability of the fission fragments are investigated. The total fission cross-sections are calculated for spherical as well as deformed choices of

fragmentation, which find nice agreement with the experimental data. In addition, the fission emission times and the decay widths of the fission fragments are predicted which may be validated via future experiments. Finally, the preformation behavior of fission paths are compared at T=0 and T≠0 to have better insight of decay mechanism of ^{181}Re nucleus.

Secondly, in order to look for the exclusive role of heavy-ion induced fission, the dynamics of ^{6}He+^{238}U reaction forming ^{244}Pu* is studied over the center of mass energy range of $E_{c.m.}$=15.0-28.8 MeV, using the DCM. The β_2-deformed fragments of ^{244}Pu* in the mass range A_2=106-113 (plus their complementary heavy fragments), corresponding to asymmetric fission peaks, are found contributing towards the fission cross-sections. Due to the availability of spontaneous fission half-lives of some neighboring Pu isotopes, we have extended our study to the spontaneous fission (SF) in decays of even mass $^{234-246}$Pu nuclei. The calculations for the SF half-lives of these Pu-isotopes have been made within the framework of preformed cluster model (PCM), both for spherical as well as β_2-deformed choices of decay fragments, and a comparison is made with the corresponding experimental data. The importance of the orientation degree of freedom (hot compact or cold elongated configurations) is also explored. Finally, the potential energy surfaces and barrier modification effects are analyzed in view of spontaneous and the heavy-ion induced fission processes.

Chapter 7 summarizes the results obtained in the present work. A brief description of the conclusions drawn is presented in this chapter. The applicability and the possible future extension of this work is also discussed at the end.

Chapter 1

Introduction

The early universe acts as the ideal particle accelerator where the quantitative properties of the particles such as energy, density, etc. were beyond what we can ever expect to accomplish with artificially built reactors. After its evolution, it was assumed that many chemical elements were released in the Supernovae and the Stellar interiors. An extensive study [1] on gamma ray emission from the ^{26}Al in the central regions of the Galaxy was carried out by the team led by Roland Diehl of the Max Planck Institute in Garching, Germany. This study gave an estimation of the amount of ^{26}Al in the Galaxy, which is expected to decay spontaneously. It was stated that the total quantity of ^{26}Al in the Galaxy is comparable to 3 solar masses and consequently ^{26}Al was considered to be the prime constituent for the emergence of planets of the copernican system; since the heat produced during such decays is an essential component to unfreeze the cometary matter in the formation of rocks. Moving towards the inner side of our Milky Way Galaxy, it is evident that some spontaneous energy-producing processes are also occurring in our solar system.

Since, scientists love to anatomize, so it would not be unnatural for them to admire the composition of our planet earth's crust, mantle and core. Studies on crustal decay reveal that the delightful conditions, we enjoy on earth's surface are basically due to the spontaneous decay processes taking place in its crust. At the end of nineteenth century,

scientists were unaware of the fact that most of the heat energy required for human's survival is liberated by the disintegrations which occur in the rocks that are responsible for the formation of Earth's crust. However, the mantle is highly attenuated and there are rare decompositions in the core. At the moment, in the earth's crust, there is large abundance of the three most ample heat producing elements- Uranium, Thorium and Potassium. All these universal spontaneous decay processes lead to the generation of endless curiosity in the minds of the scientists which encourages them to extract further knowledge about such disintegrations. Later on, in 1896 and 1898 respectively, Becquerel and the Curies made a significant development in the world of subatomic structure of a substance, by discovery of 2 new elements i.e. Polonium and Radium. While working on pitchblende, Marie Curie herself fabricated this activity of emission of rays from any element as the idiom "Radioactivity". This discovery answered many queries regarding the various decays taking place in this galaxy, in the Sun, in the Earth's crust, etc., which led to a conclusion that mostly everything in this universe is radioactive. The food and water we intake, the things we use in our daily life and everything we see around ourselves is radioactive. During the Hiroshima atomic bomb blast, it was estimated that less than 2% of the people died because of the radiation-induced cancer, which means that the junks in the blast were too much radioactive and were strong enough to induce cancer in the living beings. Ernest Rutherford in 1899 [2] identified the emission of α and β particles from a radioactive source. Therefore, between the "Miraculous Decade"-1895 to 1905, nuclear physics laid its foundation when practically most of the modern physics phenomena were established. In 1911 [3] and 1919 [4] respectively, the first experimental detection of atomic nucleus and the discovery of the nuclear reaction was made, which was proved to be the another milestone in the journey of understanding a novel branch of physics called nuclear physics. In 1920, it was discovered that the key source of the production of stellar energy in Stars and Sun is the Nuclear Fusion. Arthur Eddington [5] proposed that hydrogen and helium are two major sources in production of such energies in stars. This discovery of nuclear fusion phenomenon commenced a scientific advancement in the

area of nuclear physics. Later on, George Gamow [6] quantum mechanically explained the theory of α-decay in 1928, which describes the relation between energy of ^{4}He-nucleus and its barrier penetration probability. The discovery that revolutionize the nuclear physics and further resulted in many applications such as energy production, security, etc., was carried out experimentally by the nuclear physicists Lise Meitner, Otto Frisch and Otto Hahn [7] in 1938. They concluded that something wonderful, which previously assumed to be unimaginable was actually taking place i.e. Uranium nucleus was splitting into two. Since biologists used to refer the term binary fission for the cell division, Meitner named the division of a nucleus as Nuclear Fission. Just after an year, physicists Bohr and Wheeler [8] theoretically explained the mechanism of nuclear fission which finds its basis on Liquid Drop Model of the nucleus. To analyze the effect of internal energies acquired by a nucleus, scientist G. N. Flerov, in 1940 [9] observed a new kind of transmutation named Spontaneous Fission which contributed immensely in overall development of nuclear physics. In the same year, Martin Kamen found the radiocarbon isotope ^{14}C [10] which was further worked out by Willard Libby in 1946 to propose a novel technique to estimate the life of carbon based contents from the living creatures. Since then, this technique is known as Radiocarbon Dating and is still applied by scientists to determine the age of fossils and other organic materials. Apart from the emission of α, β, γ and fission fragments from a parent nucleus, possibility of another kind of radioactivity, was explored in late 20^{th} century by A. Sandulescu, D. N. Poenaru & W. Greiner [11], known as Cluster Radioactivity that deals with the spontaneous decay of clusters heavier than ^{4}He (α-particle). This discovery provoked scientists H. J. Rose and G. A. Jones to perform a systematic study for the observation of this new form of natural radioactivity from ^{223}Ra [12]. Up to date, ^{34}Si is the heaviest cluster observed experimentally; although clusters heavier than this range are predicted by Poenaru *et al.* from the emission of super-heavy parent systems in 2011 [13, 14], and the process is termed as Heavy Particle Radioactivity (HPR). Due to the discoveries of all these phenomena, it is unbelievable to circumvent nuclear physics from a scientific curriculum since it is linked to Quantum

Mechanics through Rutherford's planetary atomic model and the theory of hydrogen spectrum. The prime characteristic quantity in nuclear physics that describe the spontaneous emission phenomenon, theoretically or experimentally is its half-life ($T_{1/2}$). $T_{1/2}$ of a radioactive nuclide refers to the time needed to decay the unstable radioactive nucleus to the half of its initial mass. Due to the fact that different parent nuclei have different half-life properties with respect to their channel of the decay, the nuclear physics has its vast implementation in various practical fields. Today's most demanding advancements in medicines, defence, archeology and tens of other everyday uses are emerged from the field of nuclear physics. Especially, in the field of medical sciences, it has led to the remarkable ground-breaking progresses to diagnose several critical diseases and their therapy techniques. The type of the therapy required for a particular disease basically depends on the concentration of the radiation needed to completely kill the injured cells/tumors. In order to do the same, half-life of a nucleus plays a vital role since the typical range of the $T_{1/2}$ for radionuclides (used for therapy purposes) is between six hours and seven days [15]. As an instance, to cure hyperthyroidism and thyroid cancer, the radionuclide ^{131}I is used which has a physical β-decay half-life of 8.02 days. The radiation emitted from ^{131}I completely destroys the thyroid cancer cells in the specified period of time. Hence, one can say that the chief ingredient for the implementation of nuclear physics in our daily survival is the half-life of a nucleus. Beside the half-life data, other nuclear structure properties such as transition energies, intrinsic quadrupole moments, yrast spectra, etc. are of extreme importance to understand properly the nature of the nucleus and its subsequent decay channels/modes. One of the major contribution in deciding the decay mode of a specified ground state parent nucleus is its binding energy, which is directly associated with the stability of the parent and daughter system. Hence, a comprehensive study is carried out on the possibilities of various decay modes of a ground state parent nucleus. It includes α-decay, cluster radioactivity (CR), heavy particle emission (HPR) and spontaneous fission (SF), in terms of their structural properties and the corresponding half-life data. The mentioned possible decay modes in ground state parent nuclei are

explained in the upcoming section 1.1.

1.1 Spontaneous decay mechanisms

Ground state radioactivity refers to the decay of a ground state parent nucleus after the completion of its half-life. The most expected question regarding the spontaneous decays can be speculated easily; if the nucleus is already in its ground state, then why is it decaying further? This type of decay generally occurs to attain the stability of the daughter product and the nucleus will continue to decay until it achieves a stable configuration such as magic daughter. According to a French axiom-"All roads go to Rome", it is inferred that a radioactive nucleus (person) can undergo various decay mechanisms (roads) to reach a stable daughter nucleus (Rome), which means that to acquire the stability, nucleus may experience different/various radioactive decay modes like α-radioactivity, cluster emission, spontaneous fission, etc. An informative description of these decay mechanisms is presented in Fig. 1.1 and are discussed in the forthcoming subsections.

1.1.1 Alpha Decay

Before 1895, nobody imagined that the matter can radiate, except if it is inflamed, or subjected to a high voltage. However, after the revolutionary discovery of X-rays by Henri Becquerel [16], Ernest Rutherford gave evidence of the emission of α-radiation from a radioactive source. He interpreted these α-particles as ionized He-atoms. According to him, the helium nuclei which have an exit velocity around 10^7 m/s (energy range 4-9 MeV) and acquire a positive charge are termed as α-particles. Later on, in 1920s, George Gamow quantum mechanically explained this emission process in terms of the potential barrier. According to him, the α-decay occurs even when a potential barrier of repulsive nature is present. This theory of alpha-emission is popular as tunnelling effect. The principal reason for such kind of barrier tunnelling is based on the fact that although amplitude of wave function in interior of such a barrier decreases exponentially, but in

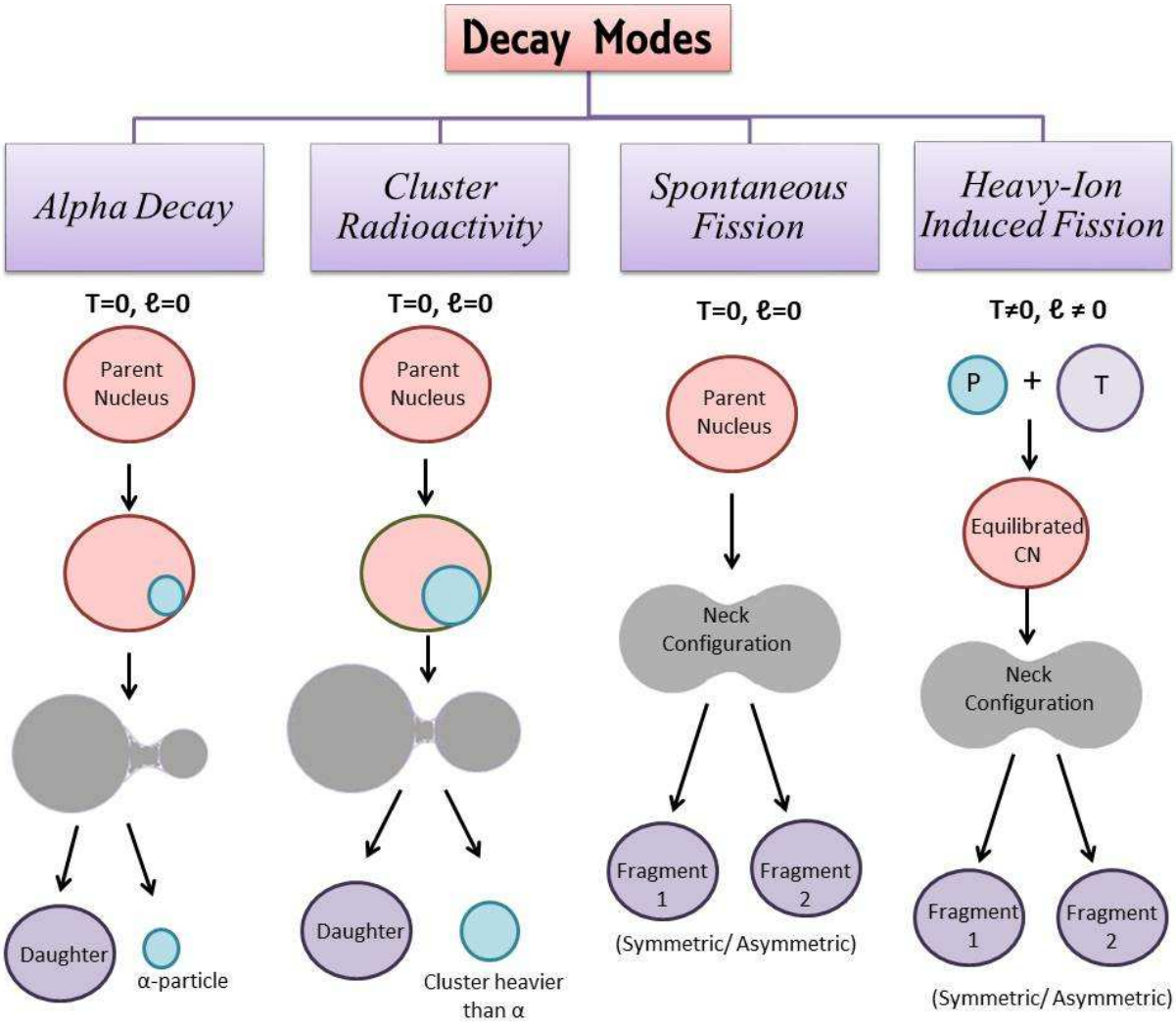

Figure 1.1 A flowchart illustrating the mechanism of α-decay, cluster emission, spontaneous fission and heavy-ion induced fission studied in the present thesis.

case of α-decay, the wave function does not diminish completely due to the small area of limited repulsive potential. As a consequence of this, the probability of finding the particle outside the potential barrier is not zero.

There are two arguments which justify that the α-emission is a fundamental decay mode in heavy and super-heavy nuclear systems. One is the pairing of two neutrons and two protons inside the parent, which leads to the formation of α-cluster due to the saturated nuclear forces. Secondly, with the increase in charge number of parent system, Coulomb repulsion increases in heavy nuclear systems as compared to nuclear binding force, as a result of which the Q-value of α-decay channel becomes more positive (negative in case of separation energy). Due to the above mentioned reasons for the dominance of α-decay in heavy systems, it is proved that this decay mode imparts important information about the nuclear properties like half-life times, clustering, shell closure effects, shape of nucleus, etc. However, in super-heavy mass region, it is usually applicable experimentally in the synthesis and identification of new nuclides either via direct decay mechanism or via successive α-decay chains. If we concentrate on the heavy α-emitters [17], the range starts from Lead (Pb having Z=82) to Oganesson (Og having Z=118). The lowest α-decay half-life is 1.2x10^{-7} seconds for ^{218}Th, having Q-value=9.849 MeV. Beside the heavy and super-heavy mass regions, the second most favorable domain to study α-decay is the northeast of ^{100}Sn in the island of stability. Because of the proximity interactions of completely filled shell closure property of its elements i.e. N=Z=50, the energy available for such decays is adequate to overcome the Coulomb barrier. This leads to the emergence of an island of α-decay above ^{100}Sn which ranges from Te (Z=52) to Ba (Z=56) and N$\leq$60. This domain is usually referred as Super-allowed alpha-decay region near doubly magic ^{100}Sn. This is due to the fact that this region lies near the proton drip line, so protons and neutrons are believed to settle in alike orbital, which in turn results in an increase in the α preformation factor inside the parent nucleus. α preformation factor here corresponds to the probability of an α-cluster to preborn in the parent nucleus. Hence, it is important to note that in addition to penetration factor, preformation probability is also found to be

a crucial parameter in the description of nuclear structure and related nuclear properties. Apart from the phenomenon of ground state α-radioactivity, various experimental [18–20] as well as theoretical [21] evidences obtained on α-decay chains in this Superallowed α-emission region make it an exciting prospect for further investigations regarding nuclear behavior. These chains are generally initialized through the collision of projectile having specific beam energy on a target nucleus. The compound system formed, then decays via such α-chains along with a significant release of energy.

Several experimental and theoretical groups studied α-decay extensively in order to obtain the various nuclear properties such as nuclear spin, lifetimes, nuclear structure, binding energies and deformations, etc. In the rare earth region, studies in [22–24] synthesized different artificial α-emitters such as isotopes of Au, Hg, Gd and Dy which have a very short half lifetimes. In the experiments of [25] and [26] respectively, the scientists identified the α-radioactivity half-lives and the partial widths of ^{209}Bi. Oganessian *et al.* performed a number of experiments on the α-decay chains of super-heavy systems ranging from Z=113 to Z=118. On the other hand, in lighter mass region (Sn-island), the α-decay chains were spotted by Capponi *et al.* [20] for Z=56 and by Liddick *et al.* [18] for Z=54 using spectacular experimental techniques. While moving towards the theoretical explanation of α-radioactivity, various models have been developed to describe this nuclear phenomenon. These theories include the double folding potential model [27], microscopic universal decay formulae [28], Generalized Liquid Drop Model (GLDM) [29–31], relativistic mean field approaches [32], UMADAC [33], Coulomb and Proximity Potential Model (CPPM) [34], Preformed Cluster Model (PCM) [35, 36], etc. Some of the mentioned theories consider α-preformation probability as the equally contributing factor along with the respective penetration probability while others do not. In the present work, collective clusterization approach is employed to explore spontaneous and excited state α-decays of some trans-Sn nuclei ranging from Tellurium (Z=52) to Barium (Z=56) whose chains are observed experimentally [20]. Since, α-decay is the lightest cluster decay mode among all the decay mechanisms studied in present work, therefore in the next subsection, we

proceed towards the detailed explanation of heavier cluster mechanisms such as cluster emission, heavy particle radioactivity and spontaneous fission which are worked out in the following sub-sections of this chapter.

1.1.2 Cluster Radioactivity

After giving an outline of super-asymmetric α-decay channel, now this thesis is focussed on relatively symmetric decay channel called as cluster radioactivity (CR). In CR process, the outgoing fragment is heavier than α-particle (^{4}He) but much smaller than fission fragments. The predictions on cluster decay, were first of all, given by Sandulescu *et al.* in 1980 [11] presenting a new kind of exotic decay that basically acts as a bridge between α-radioactivity and spontaneous fission (SF). As far as its experimental detection is concerned, this phenomenon was observed by Rose & Jones [12] in 1984 where ^{223}Ra emitted ^{14}C cluster with complementary fragment ^{209}Pb. As mentioned earlier, cluster radioactivity captivates an intermediate position between α-emission and SF, the explanation of such exotic decays can be described in terms of two different formalisms. One (fission) can be considered as the "adiabatic" [37–39] phenomenon since it incorporates the pre-scission stage where product fragments are in the overlapping zone. On the other hand, α-particle emission consists of the overlapping of the mother nucleus wave function with the emitting fragments following the immediate formation of a cluster (α-particle). This may be termed as "non-adiabatic" [40, 41] formalism. The radioactive decays via cluster emission are usually observed experimentally in the parent nuclei having mass A>220 with the complementary daughter fragment in the vicinity of doubly magic ^{208}Pb nucleus. Most of the earlier theoretical studies revealed that cluster radioactivity generally leads to the emergence of either cluster or daughter fragment involved in the magic numbers; thereby advocating the importance of shell effects in such radioactive decays. Up to date, the experimentally observed clusters [42] are in mass range A_2=14 to 34 i.e. from ^{14}C to ^{34}Si emitted from radioactive parents ^{221}Fr to ^{242}Cm. While on the theoretical front, clusters lighter than C (like ^{8}Be) and heavier than Si (like ^{46}Ar and ^{48}Ca) are also predicted having

the half-life values ranging within the upper limits of experiments. Currently, the largest half-life known in the cluster decay is 10^{29} seconds for Ne cluster. Also, it is observed that the cluster emission in odd mass parent systems is relatively difficult as compared to the even-even nuclei [43]. Therefore, even isotopes are considered to be the preferable cluster emitters which are, in actual, more in number than the odd ones.

The exotic phenomenon of cluster radioactivity usually takes place in two islands of periodic table. One is the region around doubly magic ^{208}Pb whose evidence is well established experimentally as well as theoretically in several studies. A key role in experimental study of cluster decay processes is played by Buford Price [44], Eid Hourany and Michel Hussonnois [45, 46], Svetlana Tretyakova [47], and Bonetti [42] and their coworkers. The theoretical studies on cluster decay around ^{208}Pb were successfully accomplished by various models like Analytical Super-Asymmetric Fission Model (ASAFM) [11, 48, 49], universal decay formula [28, 50], GLDM [51], Coulomb and Proximity Potential Model (CPPM) [52], Preformed Cluster Model (PCM) [53–62], etc. Two kinds of approaches are implemented generally to investigate cluster radioactivity. One of them is the Unified Fission Model (UFM) approach which is further applied in ASAFM [48,49] of Sandulescu, Poenaru and Greiner where internal barrier penetration is extremely important. Here, the probability of emergence of a particle/cluster in the interior of the parent is always counted as unity; whether it is an α-particle or a cluster. The second one refers to the cluster models like Preformed Cluster Model (PCM) of Gupta and co-workers where cluster is supposed to be preformed inside the mother nucleus and hence, its probability of being preborn inside the parent is known as preformation probability. Barrier penetrability is considered to be a different quantity here which is calculated via WKB approximation. Another region for possible occurrence of cluster radioactivity exists in the territory of doubly magic ^{100}Sn (neutron deficient) and ^{132}Sn (neutron rich) nuclei. Some attempts [63] were made experimentally to detect the ^{100}Sn-radioactivity from ^{114}Ba nucleus produced via ^{58}Ni+^{58}Ni reaction. In addition, some theoretical works predicted that Ba is a favorable parent system for cluster decay, but all such attempts ended with only the upper

limits. Extensive studies on Pb-radioactivity [58–62] and Sn-radioactivity [54,55,64] have been carried out within PCM so as to obtain the information about the structure of parent nuclei which in turn helped to understand the relevance of emergence of different decay channels.

Beside the cluster radioactivity, another kind of ground state decay was predicted by Poenaru *et al.* [13,14] in 2011 using ASAFM which explained the emission of heavy cluster (heavier than normal cluster and smaller than fission fragment) from the super-heavy element region (Z>110). This phenomenon was termed as Heavy Particle Radioactivity (HPR). Although HPR is very much similar to cluster decay, but its out-coming fragments are similar to the asymmetric fission fragments. After the discovery of HPR, a number of theories attempted to address such exotic phenomenon of heavy clusters. Work of Santhosh *et al.* described HPR for the super-heavy elements Z=116-124 within CPPM approach and compared the results with universal decay formula given by Poenaru and universal decay law (UDL) of Qi *et al.* Within the approach of PCM, this work has been carried out for Z=113, 115 and 117 [65] to probe the role of different nuclear proximity interactions in spontaneous decays of super-heavy nuclei. In the present study, the collective clusterization formalism is applied within PCM in order to explore the cluster radioactivity (and HPR) in the trans-Pb region, particularly for U (Z=92) isotopes. Additionally, the predictions on cluster decay of trans-Sn neutron-deficient as well as neutron-rich nuclei ranging from Xe (Z=54) to Gd (Z=64) are made. The deformation effects of binary fragments in decay channel are duly incorporated in Pb as well as Sn-region cluster radioactivity. Beside α-decay, CR and HPR, spontaneous fission is a major contributor for ground state decay mechanism of heavy and super-heavy nuclei. This decay path is briefly discussed in the next subsection.

1.1.3 Spontaneous Fission

Meitner and Frisch [7] spotted nuclear fission for the very first time on the basis of Liquid Drop Model (LDM) approach. LDM approach highlighted a fact that a nucleus is

similar to a liquid drop which splits into two droplets under the influence of any external perturbation. Just as similar to the concept of surface tension, the mutual repulsive forces present in the heavy nuclei overcome the nuclear short range interactions in the phenomenon of fission. The mechanism of nuclear binary fission had been thoroughly explained by Bohr and Wheeler [8] in terms of critical energies required, dependence of cross-sections on excitation energies, etc. Further, to validate the fissioning of a nucleus spontaneously, Petrzhak and Flerov [9] discovered the spontaneous fission (SF) of ^{238}U nucleus with half-life of approximately 10^{16} years. After this discovery, various experiments were performed to estimate the SF half-lives for other isotopes of U and other heavier actinide elements. It is important to mention here that the process of SF primarily occurs in elements greater than Z=90 due to the dominance of Coulomb forces which are further responsible in making the nucleus unstable. The SF half-lives from Thorium (Z=90) to Fermium (Z=100) vary significantly i.e. it ranges from 10^{18} years to 10^{-10} years approx. In other words, it can be said that the SF half-life values usually decrease with the increasing charge of the parent nucleus. In terms of isotopic analysis, it varies substantially from 12 minutes to 10^3 years for ^{256}Cf to ^{246}Cf parent nuclei. On analyzing the SF half-life data [66] enormously, one can notice that odd isotope of any element exhibit longer half-life value in comparison to those of even neighboring isotopes. Thus, spontaneous fission is proved to be a fundamental factor in estimating the stability and structural behavior of nuclei heavier than thorium. Because of the absence of external excitation energy, the spontaneous fission is more sensitive to shell closure effects in comparison to induced fission. Generally, one of the emitting fragment in spontaneous fission always corresponds to the doubly magic ^{132}Sn nucleus. In heavy and super-heavy mass nuclei, the shell-effects are found to be the key source of all barrier as well as structural surprising characteristics taking place in fission. Shell effects, in ground state phenomena, lead to some important characteristics such as potential energy surfaces (PES) and other related fission barrier properties, which further affect the decay half-lives of nuclei. As an instance, the time taken by a nucleus to travel from saddle point to its scission

configuration depends upon the nature/structure of the PES [67]. In other words, PES provide the qualitative description about the range of spontaneous fission half-lives.

Spontaneous fission eventuates quantum mechanically where the nucleus tunnelling occurs through the potential barrier to reach its scission point. Theoretical fission approaches such as Unified Fission Model (UFM) [68, 69], Saddle-Point Fission model (SPF) [70], etc. successfully explained this crucial phenomenon of nuclear physics. The UFM considers the fragment formation probability always equal to one, on the other hand, within SPF approach, such probabilities are calculated at their respective saddle points. The mother nucleus is assumed to penetrate the potential barrier, and arrive the saddle shape, as a unit. Evidently, the potential used in SPF is somewhat similar to the ones used in two-centre shell model approach (TSCM) [72,73] where scission configuration always locates outside the barrier. In contrast to SPF, Scission-Point Fission Model [74] also came into picture which explained the penetration of a nucleus which is already in its touching state and the complete scissioning happens after the tunnelling process. Here, the potential employed is identical to UFM approach. Beside these fission models, several empirical relations were derived to calculate the fission barriers and corresponding SF half-lives. In 1955, Swiatecki proposed that to calculate more reasonable values of fission barriers, shell correction energy term should be added to the respective liquid drop energy barrier [75]. This additional term in potential barrier energies improvised the outcomes obtained in terms of SF half-lives. As an extension to this, Strutinsky [76] suggested the idea of calculating this shell correction term theoretically with incorporation of deformations of the parent and the daughter fragments. Above approaches were proved be quite efficient in addressing various characteristics of ground state fission. Later, other macroscopic-microscopic models were developed to determine the heights of fission barriers for heavy and super-heavy parent systems. In addition to above methodologies applied for the investigation of spontaneous fission properties, cluster models such as GLDM [71], ATCSM [72, 73], CPPM [78, 79] and PCM [77] made significant developments in addressing the phenomenon of spontaneous fission thoroughly. The work on such ground

state phenomenon, particularly for spontaneous fission is accomplished in [77] within the methodology of PCM in terms of identification of emitting fragments and their corresponding half-lives. In this work [77], we have used PCM to address the spontaneous fission of ground state parent nuclei ranging from Z=92 to 108 and the comparison of SF with other spontaneous decay mechanisms like α-decay, cluster emission and heavy particle radioactivity is also worked out. In view of the decay modes explained in the above sub-sections, the island of stability is illustrated in Fig. 1.2 to specify the regions of the occurrence of different decay mechanisms. Apart from α-decay, cluster emission and spontaneous fission, other decay modes like proton radioactivity, neutron decay, etc. are also highlighted in the figure. Furthermore, the another kind of binary fission mode through which a nucleus can disintegrate is the Induced Fission. The difference between spontaneous and induced fission is basically due to the external excitation energies and angular momenta acquired by the parent/compound nucleus. A brief introduction to the mechanism of induced fission is discussed in the next section.

1.2 Induced Fission

Besides the above discussed spontaneous fission, another process through which fission is observed, is via collision of projectile and target nuclei with some center of mass energy. The amalgamated nucleus, thus formed, is known as compound nucleus, acquiring some excitation energy and angular momentum value. In induced fission, this projectile may be a neutron, proton, α-particle or heavy-ions. Heavy-ions here refer to the projectile nuclei heavier than ^{4}He. In the collision of heavy-ion projectile and target nucleus, the repulsive Coulomb force and attractive nuclear potential establish a barrier through which both the long range and short range forces balance each other. This barrier is known as Coulomb barrier, which acts as an extremely essential characteristic in forming the compound system. However, in the cases where Coulomb repulsion becomes immensely high, compound nucleus formation is forbidden even when the system overcomes fusion barrier. Analogous

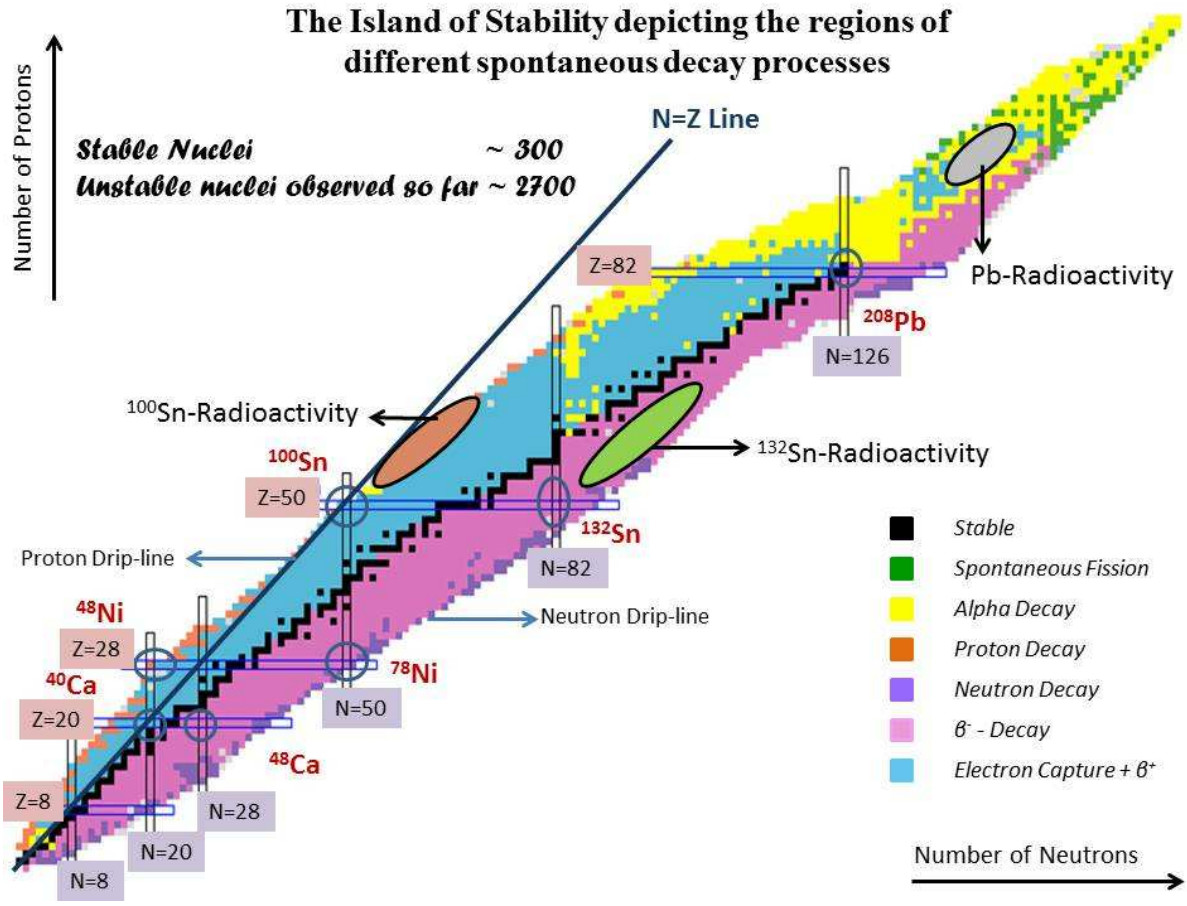

Figure 1.2 The island of stability, illustrating the respective fertile regions for various radioactive phenomenon like α-decay, cluster radioactivity (^{100}Sn, ^{132}Sn and ^{208}Pb) and spontaneous fission.

to spontaneous decays, the compound nucleus formed in its excited state, has different possibilities through which it can disintegrate to form stable products. These possibilities include Evaporation Residues-ERs (like α-radioactivity in ground state), Intermediate Mass Fragments-IMFs (like ground state cluster decay), Heavy Mass Fragments-HMFs (like heavy-particle radioactivity) and Fission (like spontaneous fission). The decay channel in induced reactions primarily depends on the beam energies, angular momentum acquired by the compound system, mass asymmetry of the reaction partners, etc. The mechanisms mentioned above such as ER, IMF, HMF and fission occur at low energies i.e. E$\leq$15 MeV per nucleon. A large number of experiments have been performed using low energy heavy-ion beams which impart important information regarding reaction dynamics, mass distributions and the corresponding cross-sectional yields, etc. The mass distribution of fission fragments imparts fundamental information about the nuclear structure and the subsequent decay aspects. Moreover, it is closely related to the potential energy landscape of the fissile nucleus as revealed in saddle- and scission-point models [70, 74]. Experiments are being done on the fissioning nuclei to generate the fragment mass/cross-sectional yields so as to understand the fission decay mechanism more precisely. Such yields impart very useful information about the decay properties such as their fragment identification, emission times, barrier properties, etc. On the experimental front, it is very essential to be aware about the fission decay products since they have a great impact on the properties of nuclear fuel. As an instance, fission products participate in the production of heat by decaying themselves or by capturing and emitting neutrons. Consequently, fission fragments result in producing heat energy due to the radioactive emissions. Moreover, we know that nuclear fission is an exothermal process and as a consequence, it has huge applications in the production of energy. For example, in the fission fragmentation of an actinide nucleus, around 180 MeV of energy is released which directly indicates that 1 kg of Uranium (effective in generating 2x10^7 Kilowatt hours of energy) is sufficient to glow a bulb of 100 Watt for continuous 25,000 years. So, the proper understanding of the fission fragments is extremely important, particularly in view of their emission times

and respective structural behavior. In past, significant efforts have been put forward to measure the fission emission times (τ_f) using various experimental as well as theoretical methods [80–84]. The typical range in which fission fragments are emitted varies from 10^{-21} to 10^{-17} seconds; depending on the mass and excitation energy of the compound system. In reference to theoretical formalisms, numerous efforts have been accomplished to examine the decay of excited compound nuclei via ER, IMF/HMF or fusion-fission exit channels within the collective clusterization approach [85–87]. Fission of heavy actinide nuclei consisting Fm, Bk, U, Pu, Th, etc., has been explored using the formalism of Dynamical Cluster-decay Model (DCM) so as to analyze the mass distribution yields and the subsequent decay properties. The entrance channel effects and other decay mechanisms such as non-compound nucleus processes, are also studied within DCM in the other mass regions (light mass, super-heavy region) of periodic table. In present thesis, the study is confined to heavy ion induced fission in heavy CN mass region. The fission of pre-actinide ^{181}Re and actinide ^{244}Pu nuclei are addressed; depicting the mass distributions of the decaying channels and the fragments emitting from the compound system are identified. In this analysis, the comparative study is carried out in order to observe the structural profile difference between spontaneous fission and the induced fission. In view of ground state and excited state studies covered in this thesis, it has been observed that the deformations of decaying fragments and their associated orientation degree of freedom play a significant role. The explanation to the importance and contribution of deformations and related orientations is discussed ahead in the next section.

1.3 Deformations and Orientations

Based on the everyday experience, a classical liquid drop when left secluded and undisturbed, remains spherical until or unless it is perturbed externally. This is because of the minimum surface tension acquired by the drop in the spherical configuration. Similarly, a magic nucleus can be made non-spherical (deformed) by breaking its symmetry

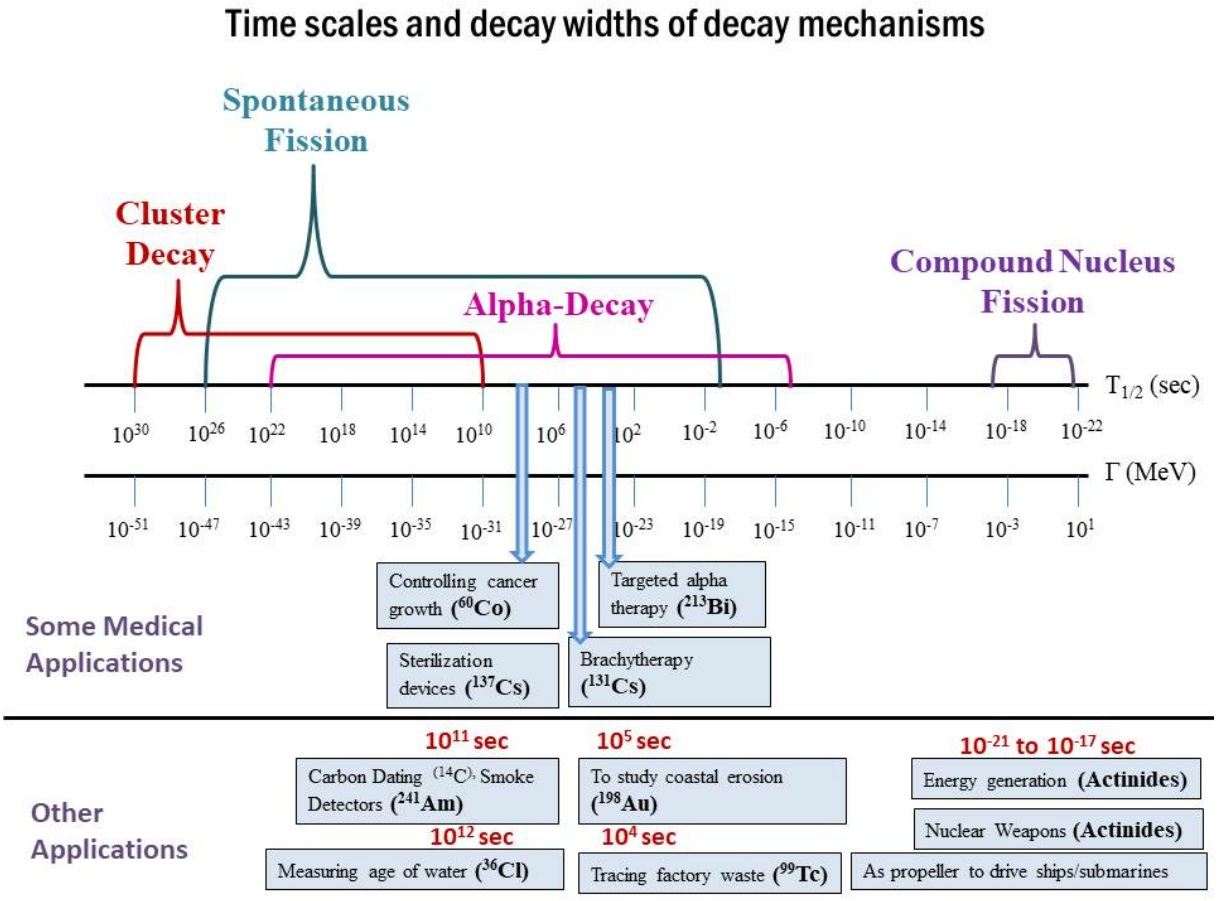

Figure 1.3 Characteristic time scales and decay widths of various ground and excited state decay mechanisms. Some examples of applications are also depicted in the figure in terms of their respective time scales.

by adding a few more nucleons to it. The resultant shape will be no more spherical due to the disruption of its shell closures. Pauli proposed the idea of deformations in 1924 [88] where he explained the origin of hyperfine structure of atoms and molecules. According to his theory, the electromagnetic interaction with the non-spherical nuclei gives rise to such hyperfine structures. The experimental evidence of deformations was demonstrated by Schuller and Schmidt [89]. Later, Bohr and Wheeler [8], while explaining the theoretical mechanism of nuclear fission, suggested the concept of nuclear shape vibrations. The parameter used to designate the extent of the deformation degree of freedom in a nucleus is known as Quadrupole Moment. Basically, it represents the deviation of a nucleus from its spherical symmetry. The quadrupole deformation (β_2) is the simplest and smallest order of deformation which is further divided into two types i.e. prolate (+ve and elongated) and oblate (-ve and flattened). The prolate nuclei are more in number as compared to the oblate systems, because the Coulomb repulsion deforms the nucleus more into an elongated configuration than flattened one. Usually, prolate nuclei are found just after the completely filled shells while the oblate nuclei are found near the end of the closed shells. The higher order deformations such as octupole (β_3) and hexadecapole (β_4) are also proved to be vital components in understanding the nuclear decay dynamics of super- and hyper-deformed systems. The octupole deformed nuclei appear as pear shaped having its reflection asymmetric. The role of deformations in various decay mechanisms has been studied extensively using many theoretical approaches. In the current thesis, the effect of deformations is analyzed so as to get a complete picture of the decay dynamics involved in different spontaneous as well as excited state processes.

Not just the deformation parameter plays a crucial role in explaining the nuclear properties, the corresponding orientation degree of freedom also plays an equally essential role. Orientation of a nucleus refers to the inclination of the symmetric axis of a system with respect to its collision axis. The two interacting/ decaying nuclei may exists in same plane (co-planar) or different planes (non-coplanar). In a number of studies [60, 61], it is noticed that the incorporation of deformations with proper addressal of orientation

leads to the reduction in the barrier height. Moreover, the barrier height of the various decaying channels depends upon the configuration of optimized (fixed) orientations which is divided into two categories. One is the cold-elongated configuration having largest interaction radius and the lowest barrier height, whereas the another one is the hot-compact configuration which possesses smallest interaction radius and exhibit highest barrier height. For a detailed description of the optimized orientations, one may see reference [90]. Since, the spontaneous decay processes are assumed to be cold phenomenon traditionally, so the deformations having cold-elongated configurations are opted while addressing the decay paths of ground state nuclei. On the other hand, orientations having hot-compact configuration are incorporated in the work where induced fission process is explored. As discussed above, the inclusion of deformations and orientations is desirable for the comprehensive knowledge of the decay dynamics of ground state as well as excited state nuclear systems, so these effects are included wherever applicable.

1.4 Motivation of the present work

For comprehensive understanding of nuclear dynamics, extensive studies are being done on experimental as well as theoretical front. To have a clear picture of the binary fragmentation, the identification of the mass fragments emitted in different spontaneous and induced decay processes play very important role. It is evident from literature that the half-lives of nuclei provide significant information about the stability status of a nucleus. The knowledge of emitting fragments and their respective half-lives could be exploited to address various important applications in the field of health and medicine, energy, etc. Based on the half-life data of different decay mechanisms, Fig. 1.3 is illustrated, where the broad range of half-lives and decay widths of different decay processes are depicted. In today's world, it is well known that nuclear energy is the most undoubted future source. Actinides ranging from Z=89 to 103 are the most commonly used elements in the production of nuclear weapons and in providing the electrical power to space vehi-

cles; especially Plutonium (Z=94), Curium (Z=96), etc. ^{241}Am (Z=95) and ^{252}Cf (Z=98) are widely used in Brachytherapy and smoke detectors. Besides, lighter elements such as ^{131}I, ^{32}P, ^{90}Sr and ^{90}Y, etc. are employed to treat several maligant and non-maligant disorders such as metastatic bone pain, neuroendocrine tumors, etc. Xe is broadly used in X-ray detection to diagnose the lung problems. Anyway, the present theoretical study is carried out with the help of theoretical formalism of Quantum Mechanical Fragmentation Theory (QMFT) due to the motivation provided by the immense applications of the radionuclides. In this thesis, we propose to present spontaneous α-decay treatment of trans-Sn N=Z nuclei (ranging from Te (Z=52) to Ba (Z=56)), since α-exit channel is the most significant mechanism to explore the structure of such N=Z systems. The cluster radioactivity is worked out in the vicinity of ^{100}Sn and ^{132}Sn doubly magic nuclei. It is worth mentioning here that the doubly magic neutron rich ^{132}Sn exists on the passage of astrophysical r-processes, and consequently, its experimental and theoretical investigation is one of the most fascinating concern. The spontaneous fission of the nuclei from Z=92 to 108 is examined so as to pin point the fragments emitted in the decay process. The comparison of ground state fission with the induced one is made for two heavy nuclei i.e. ^{181}Re and ^{244}Pu in terms of their structural behavior. The detailed explanation of results obtained is shown in chapters 3 to 6.

1.5 Layout of the thesis

The present thesis is composed as follows:

Chapter 2 contains the formalism- Quantum Mechanical Fragmentation Theory (QMFT), on which the whole thesis is based. Then, the Preformed Cluster Model (PCM) within the methodology of QMFT is explained so as to address the various spontaneous decay modes like α-decay, cluster radioactivity and spontaneous fission. The useful input quantities like fragmentation potential, preformation probability, penetrability, etc. in the calculations of decay half-lives are briefly explained in this chapter. The role of shell

closure effects in radioactive decays is shown in terms of binding energy of the nucleus. Further, the PCM with temperature and ℓ-effects (centrifugal potential term) included namely Dynamical Cluster-decay Model (DCM), is presented in order to explore the heavy-ion induced dynamics. The relevance of deformations and orientations is explained concisely in context of barrier characteristics and the variations in the structural features of decaying fragments. The difference in the penetration probability expressions used in PCM and DCM are elucidated in terms of one step and two step WKB approximation approach. The PCM and DCM calculated outcomes are expounded in the upcoming chapters.

Chapter 3 provides a comprehensive description of ground state & excited state α-decay processes. The triple α-decay chains starting from ^{114}Ba nucleus (formed in ^{58}Ni(^{58}Ni,2n) reaction) and terminating at ^{102}Sn are explored in order to obtain the characteristics of decay dynamics. The 2n-cross-sections and the subsequent half-lives of considered chains have been estimated which are in agreement with the available experimental data. Next, the nuclei lying in the vicinity of super-allowed α-decay region are investigated in terms of different proximity interaction potentials. These trans-Sn nuclei include isotopes of Te, I, Xe, Cs and Ba commencing from their respective N=Z systems. The α-decay half-lives corresponding to each proximity potential are calculated for all the nuclei and are compared with the respective experimental data. The role of deformations and orientations is investigated in both spontaneous as well as excited state decays. The comparison between the spontaneous and the excited decays is carried out on the basis of their scattering potentials and corresponding structural pattern of decaying fragments. The role of shell effects in ground state α-decays is explored in comparison to ones occurred via decay chains. After exploring the trans-Sn region in view of α-emission, a study is accomplished in the same region in terms of cluster radioactivity which is presented in the chapter 4.

Here, in **Chapter 4**, the results obtained in the the exotic phenomenon of cluster radioactivity are discussed in view of the importance of deformations and orientations

included. This study is an extension of the previous work [54, 55] on Sn-radioactivity, which was focussed on spherical choice of fragmentation only. The nuclei chosen for this study, are the trans-Sn neutron-deficient and neutron-rich systems (ranging from Xe to Gd) which decay either via ^{100}Sn or ^{132}Sn-radioactivity. The fragmentation profile and the corresponding preformation distribution is analyzed after the incorporation of deformation and orientation effects. Since, cluster decay is a cold phenomenon, the orientations having cold elongated configurations have been considered. The barrier characteristics like scattering potential, barrier height, barrier modification and penetrability are worked out so that the comprehensive information can be extracted about the decay dynamics involved in cluster emission process. The effect of various nuclear proximity potentials is investigated and the respective half-life times are evaluated; thereby comparing the outcomes obtained from spherical and deformed choice of fragments. Note that no experiments are performed on Sn-radioactivity yet, hence predictions on half-lives are given in this chapter. Additionally, an attempt has been made to calculate the fragmentation potential by including the higher multipole deformations (upto β_4), so as to see the effect of hexadecapole deformations on the cluster radioactivity of the considered systems. Depending on the mass of the emitting cluster/fragment, the next radioactive decay mechanism having heavier mass of the decay fragments than cluster decay, is the spontaneous fission. An exclusive description of spontaneous fission within PCM is displayed in the **Chapter 5**.

In this chapter, the collective clusterization approach within PCM is applied to examine the traditional phenomenon of spontaneous fission (SF). 45 Actinide and the trans-actinide nuclei ranging from ^{232}U to ^{264}Hs have been selected to carry out this study. The structural pattern of potential energy surfaces is explored via fragmentation potential to infer the significant information regarding the nature of the mass distributions. The identification of the fission fragments is done within PCM for all the considered nuclei; which is not accomplished yet in experiments. The role of two kinds of radii viz effective sharp radius (R_i) and Sussmann Central Radius (C_i) is probed in terms of fragmentation

behavior and the barrier tunnelling parameters. The corresponding SF half-lives have been calculated and are then compared with respect to experimental data. Further, the competition of spontaneous fission with the other above studied decay modes like α-decay, cluster emission and heavy particle radioactivity, is probed to obtain a transparent picture of most dominant decay mode. For this analysis, four even mass isotopes of U i.e. ^{232}U to ^{238}U are used. The half-lives for these isotopes with respect to each decay mode are evaluated and compared with available data. The predictions on the half-lives of heavy-particle radioactivity have been given for the considered systems so as to present the new possibilities for the future experiments. Beside spontaneous fission, the another kind of fission occurred is the induced one which takes place when a projectile with some beam energy is hit on a fixed target nucleus. In the present thesis, induced fission dynamics is also studied and the conclusions obtained from the same are discussed in **Chapter 6**.

Chapter 6 explains the heavy-ion induced fission of two heavy compound systems formed via two different reaction partners with some given excitation energies. The excited state calculations are performed using DCM, the extension of PCM with temperature and ℓ-effects incorporated. First section of chapter 6 contains the fission decay dynamics of ^{12}C+^{169}Tm reaction forming compound nucleus ^{181}Re* at beam energies $E_{Lab.}$=77-89 MeV. The total fission cross-sections using DCM are calculated and compared with the experimental ones. The mass distributions of ^{181}Re* nucleus have been generated for both spherical and deformed choice of fragments so as to identify the contributing fission fragments. The identified fission fragments are then, worked out for the calculation of fission emission times so as to present the likely prospects for future experiments. Furthermore, second section of this chapter consists of the fission dynamics of compound nucleus ^{244}Pu* formed via ^{6}He+^{238}U reaction over the center of mass energy range of $E_{c.m.}$=15-29 MeV. The cross-sections are calculated at their respective neck-length values within the framework of DCM and are then compared with the experimental data. Additionally, due to availability of spontaneous fission half-life data of some Pu isotopes i.e. even mass $^{234-246}$Pu, the extensive study of spontaneous fission is carried out for the mentioned nu-

clei so as to finally present a comparative description of ground state and excited state fission of Plutonium nucleus.

Finally, the summary and conclusions are described in **Chapter 7**. The possible future extensions of this study are also discussed in the same chapter.

Bibliography

[1] R. Diehl et al., Nature **439**, 45 (2006).

[2] E. Rutherford, Phil. Mag. **47**, 109 (1899).

[3] E. Rutherford, Phil. Mag. **21**, 669 (1911).

[4] E. Rutherford, Phil. Mag. **37**, 581 (1919).

[5] A. S. Eddington, The Scientific Monthly **11**, 4 (1920).

[6] G. Gamow, ZP **51**, 204 (1928).

[7] L. Meitner and O. R. Frisch, Nature **3615**, 239 (1939).

[8] N. Bohr, J. A. Wheeler, Phys. Rev. **56**, 426 (1939).

[9] G. N. Flerov, K. A. Petrjak, Phys. Rev. **58**, 89 (1940).

[10] S. Ruben and M. D. Kamen. Phys. Rev. **57**, 549 (1940).

[11] A. Sandulescu, D. N. Poenaru and W. Greiner, Sov. J. Nucl. **11**, 528 (1980).

[12] H. J. Rose and G. A. Jones, Nature (London) **307**, 245 (1984).

[13] D. N. Poenaru, R. A. Gherghescu, W. Greiner, Phys. Rev. Lett. **107**, 062503 (2011).

[14] D. N. Poenaru, R. A. Gherghescu, W. Greiner, Phys. Rev. C **85**, 034615 (2012).

[15] C. Yeong, M. Cheng, K. Hoong, Zhejiang Univ-Sci B **15**, 845-863 (2014).

[16] H. Becquerel, Compt. Rend. **122**, 420 (1896).

[17] J. K. Tuli, Nuclear Wallet Cards, http://www.nndc .bnl .gov /wallet/, 2011.

[18] S. Liddick et al., Phys. Rev. L **97**, 082501 (2006).

[19] I. G. Darby et al., Phys. Rev. L **105**, 162502 (2010).

[20] L. Capponi et al., Phys. Rev. c **94**, 024314 (2016).

[21] J. P. Maharana, A. Bhagwat and Y. K. Gambhir, Phys. Rev. C **91**, 047301 (2015).

[22] S. G. Thompson, A. Ghiorso, J. O. Rasmussen and G. T. Seaborg, Phys. Rev. **76**, 1406 (1949).

[23] J. O. Rasmussen, Jr., S. G. Thompson and A. Ghiorso, Phys. Rev. **89**, 33 (1953).

[24] K. S. Toth and J. O. Rasmussen, Phys. Rev. **109**, 121 (1958).

[25] C. Cozzini et al., Phys. Rev. C **70**, 064606 (2004).

[26] J. W. Beeman et al., Phys. Rev. Lett. **108**, 062501 (2012).

[27] D. Deng and Z. Ren, Phys. Rev. C **96**, 064306 (2017).

[28] C. Qi, F. R. Xu, R.J. Liotta and R. Wyss, Phys. Rev. Lett. **103**, 072501 (2009).

[29] J. M. Wang, H. F. Zhang and J. Q. Li, J. Phys. G: Nucl. Part. Phys. **41**, 075109 (2014).

[30] X. Bao, H. Zhang, H. Zhang, G. Royer, and J. Li, Nucl. Phys. A **921**, 85 (2014).

[31] G. Royer, Nucl. Phys. A **848**, 279 (2010).

[32] M. Bhuyan, S. K. Patra and R. K. Gupta, Phys. Rev. C **84**, 014317 (2011).

[33] V. Y. Denisov, O. I. Davidovskaya, I. Y. Sedykh, Phys. Rev. C **92**, 014602 (2015).

[34] K. P. Santhosh, I. Sukumaran, B. Priyanka, Nucl. Phys. A **935**, 28 (2015).

[35] Niyti, G. Sawhney, M. K. Sharma, R. K. Gupta, Phys. Rev. C **91**, 054606 (2015).

[36] K. Sharma and M. K. Sharma, Nucl. Phys. A **986**, 1 (2019).

[37] D. N. Poenaru, D. Schnabel, W. Greiner, D. Mazilu, R. Gherghescu, At. Data Nucl. Data Tables **48**, 231 (1991).

[38] G. A. Pik-Pichak, Yad. Fiz. **44**, 1421 (1986).

[39] G. A. Pik-Pichak, Sov. J. Nucl. Phys. **44**, 923 (1986).

[40] R. Blendowske, H. Walliser, Phys. Rev. Lett. **61**, 1930 (1988).

[41] Y. S. Zamyatnin, S. G. Kadmenski, S. D. Kurgalin, V. I. Furman, Y. M. Chuvilski, Sov. J. Nucl. Phys. **57**, 1905 (1994).

[42] R. Bonetti and A. Guglielmetti, Rom. Rep. Phys. **59**, 301 (2007).

[43] S. W. Barwick, P. B. Price, H. L. Ravn, E. Hourani, M. Hussonnois, Phys. Rev. C **34**, 362 (1986).

[44] P.B. Price, Ann. Rev. Nucl. Part. Sci. **39**, 19 (1989).

[45] E. Hourani, M. Hussonnois, in Particle Emission from Nuclei, vol. II, chap. **6** (CRC Press, Boca Raton), p. 171 (1989).

[46] E. Hourani, M. Hussonnois, D. Z. Poenaru, Annales de Physique (Paris) **14**, 311345 (1989).

[47] S. P. Tretyakova, Sov. J. Part. Nucl. **23**, 156 (1992).

[48] D. N. Poenaru, M. Ivascu and W. Greiner, Int. J. Rad. Appl. Instrum. D, Vol. **12**, No. 1-6, pp. 313-316 (1986).

[49] D. N. Poenaru, W. Greiner and E. Hourani, Phys. Rev. C **51**, 2 (1995).

[50] X. Bao, H. F. Zhang, J. M. Dong, J. Q. Li and H. F. Zhang, Phys. Rev. C **89**, 067301 (2014).

[51] G. Royer, R. Moustabchir, Nucl. Phys. A **683**, 182 (2001).

[52] K. P. Santhosh and R. K. Biju, Ann. of Phys. **334**, 280287 (2013).

[53] S. S. Malik and R. K. Gupta, Phys. Rev. C **39**, 5 (1989).

[54] S. Kumar, D. Bir, R. K. Gupta, Phys. Rev. C **51**, 4 (1995).

[55] S. Kumar, J. S. Batra, R. K. Gupta, J. Phys. G: Nucl. Part. Phys. **22**, 215 (1996).

[56] S. Kumar, R. K. Gupta, Phys. Rev. C **49**, 1922 (1994).

[57] S. Kumar, D. Bir, R. K. Gupta, Phys. Rev. C **51**, 1762 (1995).

[58] S. K. Arun, R. K. Gupta, B. B. Singh, S. Kanwar, M. K. Sharma, Phys. Rev. C **79**, 064616 (2009).

[59] S. K. Arun, R. K. Gupta, S. Kanwar, B. B. Singh, M. K. Sharma, Phys. Rev. C **80**, 034317 (2009).

[60] G. Sawhney, M. K. Sharma, R. K. Gupta, Phys. Rev. C **83**, 064610 (2011).

[61] R. Kumar, M. K. Sharma, Phys. Rev. C **85**, 054612 (2012).

[62] R. Kumar, Phys. Rev. C **86**, 044612 (2012).

[63] A. Guglielmetti, R. Bonetti, G. Poli, R. Collatz, Z. Hu, R. Kirchner, E. Roeckl, N. Gunn, P. B. Price, B. A. Weaver, A. Westphal, J. Szerypo, Phys. Rev. C **56**, R2912 (1997).

[64] K. Sharma, G. Sawhney, M. K. Sharma and R. K. Gupta, Eur. Phys. J. A **55**, 30 (2019).

[65] G. Sawhney, K. Sandhu, M. K. Sharma and R. K. Gupta, Eur. Phys. J. A **50**, 175 (2014).

[66] N. E. Holden and D. C. Hoffman, Pure Appl. Chem. **72**, 1525 (2000).

[67] N. Schunck and L. M. Robledo, Rep. Prog. Phys. **79**, 116301 (2016).

[68] X. J. Bao, S. Q. Guo, H. F. Zhang, Y. Z. Xing, J. M. Dong and J. Q. Li, J. Phys. G: Nucl. Part. Phys. **42**, 085101 (2015).

[69] C. Xu, Z. Ren, Y. Guo, Phys. Rev. C **78** 044329 (2008).

[70] S. Singh, R. K. Gupta, W. Scheid and W. Greiner, J. Phys. G. **18**, 1243 (1992).

[71] G. Royer, M. Jaffre, D. Moreau, Phys. Rev. C **86**, 044326 (2012).

[72] J. Maruhn and W. Greiner, Phys. Rev. L **32**, 10 (1974).

[73] R. K. Gupta, W. Scheid and W. Greiner, Phys. Rev. L **35**, 6 (1975).

[74] F. Barranco, R. A. Broglia and G. F. Bertsch, Phys. Rev. L **60**, 507 (1988).

[75] W. J. Swiatecki, Phys. Rev. **100**, 937 (1955).

[76] V. M. Strutinsky, Nucl. Phys. A **95**, 420 (1967).

[77] K. Sharma, G. Sawhney and M. K. Sharma, Phys. Rev. C **96**, 054307 (2017).

[78] K. P. Santhosh, B. Priyanka, G. J. Jayesh, and S. Sabina, Phys. Rev. C **84**, 024609 (2011).

[79] K. P. Santhosh and B. Priyanka, Phys. Rev. C **90**, 054614 (2014).

[80] J. U. Andersen *et al*, Phys. Rev. Lett. **99**, 162502 (2007).

[81] M. Morjean *et al*, Phys. Rev. Lett. **101**, 072701 (2008).

[82] K. Kapoor *et al*, Phys. Rev. C **96**, 054605 (2017).

[83] K. Ramachandran, A. Chatterjee, A. Navin, K. Mahata, A. Shrivastava, V. Tripathi, S. Kailas, V. Nanal, R. G. Pillay, A. Saxena, R. G. Thomas, S. Kumar, and P. K. Sahu, Phys. Rev. C **73**, 064609 (2006).

[84] M. T. Senthil Kannan, J. Sadhukhan, B. K. Agrawal, M. Balasubramaniam and S. Pal, Phys. Rev. C **98**, 021601(R) (2018).

[85] G. Sawhney, G. Kaur, M. K. Sharma and R. K. Gupta, Phys. Rev. C **88**, 034603 (2013).

[86] M. Kaur, M. K. Sharma and R. K. Gupta, Phys. Rev. C **86**, 064610 (2012).

[87] R. Mittal, D. Jain and M. K. Sharma, Nucl. Phys. A **968**, 436-452 (2017).

[88] W. Pauli, Naturwiss. **12**, 741 (1924).

[89] T. Schuller and T. Schmidt, Z. Phys. **92**, 148 (1934); **94**, 457 (1935).

[90] R. K. Gupta, M. Balasubramaniam, R. Kumar, N. Singh, M. Manhas and W. Greiner, J. Phys. G: Nucl. Part. Phys. C **31**, 631 (2005).

Chapter 2

Theoretical Formulation

2.1 Introduction

The research on nuclear dynamics has been extensively explored with the advancements in various spectacular experimental techniques and the computing provisions along with the progressive scientific programming tools. The consolidated outcomes obtained from the experimental and theoretical nuclear research provide an insight to view and portray the nuclear decay dynamics with an improved perception. While experimental methods help us to visualize the nuclear reaction dynamics, on the other hand, the theoreticians provide a proper and necessary description about the internal mechanisms taking place inside the nucleus. Hence, both scientific approaches are interconnected with each other as the theory is formalized to address the experimental results while experiments are performed to validate the various predicted nuclear phenomenon. Stressing on the theoretical approaches applied to study nuclear decay aspects, a number of methodologies have been developed or are being developed in order to investigate the decay mechanisms discussed in the previous chapter. These models include Unified Fission Model (UFM) [1,2], Two-Center Shell Model (TCSM) [3, 4], Analytical Super-Asymmetric Fission Model (ASAFM) [5, 6] and many more that significantly contribute in understanding several spontaneous as well as excited state decay processes. The fundamental methodology im-

plemented in this thesis is the Quantum Mechanical Fragmentation Theory (QMFT) [7–9] which is a unified description to address the heavy-ion induced collisions and subsequent decay dynamics within the framework of collective clusterization approach. This methodology is extensively exercised to streamline various aspects related to formation and decay paths of heavy-ion induced reactions (HIRs). The QMFT follows two aspects- One refers to the preformation probability P_0 of the fragments, preborn inside parent nucleus and the second one corresponds to the penetration probability P of the preformed fragments calculated while tunnelling through the potential barrier. Within the QMFT formalism, Preformed Cluster Model (PCM) [10–19] is implemented here to analyze various spontaneous decay processes. The PCM approach is also implemented in past to examine the nuclear structure characteristics in view of radioactive cluster decay process. However, in the present study, it is worked out in the application of α-decay, cluster/heavy cluster emissions and spontaneous fission processes. Further, to exercise the excited state decays, Dynamical Cluster Model (DCM) [20–24], the extended version of PCM, is used where the temperature and the angular momentum effects are duly incorporated. The heavy-ion induced fission of heavy fissile nuclei is investigated and the deformation and related orientation effects are included wherever relevant.

2.2 Preformed Cluster Model (PCM) for radioactive decays

In recent past, various theoretical approaches have been employed to explore the ground state fission; symmetric or asymmetric or super-asymmetric. Here, the super-asymmetric one refers to the α-decay and cluster radioactivity. Some of these theoretical approaches take preformation factor into consideration while others depend only on penetration of the decay fragments. Just as in Gamow theory of α-decay [25], the value of α-preformation factor is always taken as unity. While, in the QMFT based PCM approach, the cluster is supposed to be preformed inside the mother nucleus and the probability of its formation

is termed as preformation probability P_0. This preformed fragment, then tunnels the potential barrier by hitting the barrier constantly with impinging frequency ν_0. The probability of getting the fragment outside the potential barrier is termed as penetration probability (P). It is important to note that the preformation probability of all possible fragments in binary decay is taken into account and hence different decay paths such as α-decay, cluster radioactivity, heavy-particle radioactivity and spontaneous fission could be addressed on equal footing. The decay constant λ and the corresponding half-life $T_{1/2}$ of a nucleus within PCM is estimated by:

$$\lambda = \nu_0 P_0 P, \quad T_{1/2} = \frac{\ln 2}{\lambda} \tag{2.1}$$

The impinging frequency ν_0 is expressed as:

$$\nu_0 = \frac{velocity}{R_0} = \frac{\sqrt{2E_2/\mu}}{R_0} \tag{2.2}$$

This ν_0 is determined from the experimental Q-value, taken as total kinetic energy shared between the two clusters and remains approximately constant $\sim 10^{21} s^{-1}$.

2.3 Dynamical Cluster Model (DCM) for excited state decays

The Dynamical Cluster Model, for the decay of excited state nuclei, is an extended version of PCM with temperature, excitation energy and angular momentum effects incorporated. The co-ordinates mass asymmetry (η) and separation distance (R) of binary fragmentation theory in DCM, feature following path,

(i) the nucleon-division (or -exchange) between outgoing fragments, and

(ii) the transfer of kinetic energy of incident channel ($E_{c.m.}$) to internal excitation (total excitation or total kinetic energy, TXE or TKE) of the outgoing channel, since the fixed $R = R_a$, at which the mechanism is studied, depends on temperature T as well as on η,

i.e. $R(T,\eta)$. This energy transfer mechanism bears the relation

$$E^*_{CN} + Q_{out}(T) = TKE(T) + TXE(T). \tag{2.3}$$

The CN excitation energy E^*_{CN} is related to temperature T (in MeV) via Eq.(2.19).

Using decoupled approximation in context of partial waves, the decay cross-sections in DCM are defined as below:

$$\sigma = \sum_{\ell=0}^{\ell_{max}} \sigma_\ell = \frac{\pi}{k^2} \sum_{\ell=0}^{\ell_{max}} (2\ell+1) P_0 P; \qquad k = \sqrt{\frac{2\mu E_{c.m.}}{\hbar^2}} \tag{2.4}$$

where, P_0 is the preformation probability that corresponds to η-motion and penetration probability P refers to R-motion, described in upcoming Sec. 2.4.1 and Sec. 2.5.1 respectively. Evidently for ℓ=0 (s-wave), it must be noted that σ and λ vary through a constant only. Hence, similar to PCM, the complex fragments (both light cluster and heavy fragments) are treated as the dynamical collective mass motion of *preformed clusters or fragments* through the barrier. The structural knowledge of the compound nucleus or parent nucleus in both the models can be obtained from the behavior of preformation probability P_0 (also called as spectroscopic factor) of the decay fragments calculated by solving time-independent Schrödinger equation in η-coordinate (for details, see Section 2.4.1). The principal difference between the PCM and DCM formalism lies in the following: (i) the radius expression is temperature dependent within DCM and (ii) the fragmentation potential consists of angular momentum dependent potential for the addressal of excited state decays. A flowchart, depicting the overview of the input and output parameters/quantities used in PCM and DCM, is displayed in Fig. 2.1. The difference in the penetrability expression of both the models is also illustrated. Since both PCM and DCM are based on the QMFT, so a brief discussion of the same is given in the section ahead.

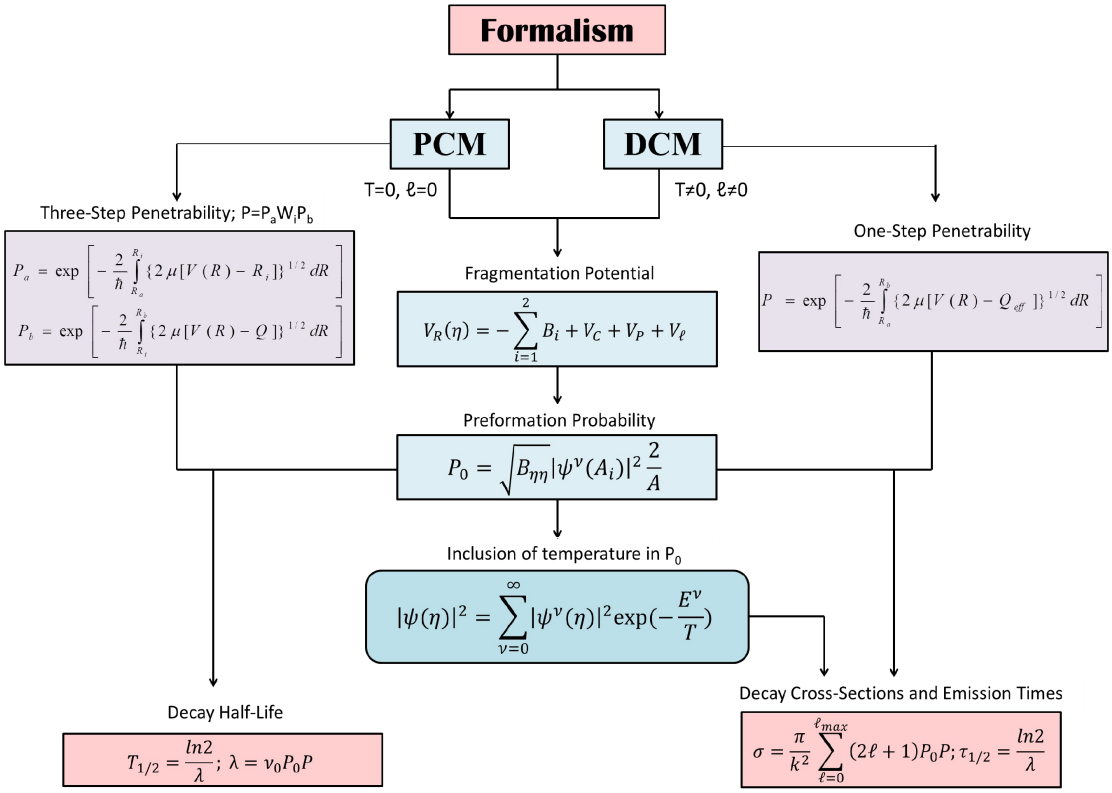

Figure 2.1 Flowchart illustration of the formalism implemented, depicting the expressions of various input and output quantities in order to address the ground and excited state decay processes.

2.4 Quantum Mechanical Fragmentation Theory (QMFT):

In QMFT [7–9], the prerequisite quantities for the elucidation of nuclear decay dynamics are the potential energy surfaces (PES) and mass yields exhibiting structural information of the decay fragments. To determine such quantities, the QMFT originates in terms of the following collective variables:

(i) relative separation R between the two emitting nuclei (or, equivalently, the length parameter $\lambda = L/2R_0$, with L as the length of the nucleus and R_0 as the radius of an equivalent spherical nucleus).

(ii) The deformation parameter $\beta_{\lambda i}$ (λ=2,3,4 and i=1,2) of the decay fragments.

(iii) The orientation degrees of freedom $\theta_i (i = 1, 2)$ of the deformed nuclei.

(iv) Azimuthal angle ϕ between the principal planes of the two interacting systems.

(v) Neck parameter ε, defined by the ratio $\varepsilon = E_0/E'$ for the interaction region ($R < R_1 + R_2$, R_i (i=1, 2) is the radius of the two nuclei). Here E_0 is the actual height of the barrier and E' is the fixed barrier of the two center oscillator. $\epsilon = 0$ represents a broad neck formation, on the other hand $\epsilon = 1$ means that the neck is fully squeezed in, corresponding to the asymptotic region ($R > R_1 + R_2$).

(vi) Mass and charge fragmentation co-ordinates [26–28].

The mass and charge-asymmetry coordinates in QMFT are expressed as

$$\eta = \frac{A_1 - A_2}{A}; \qquad \eta_Z = \frac{Z_1 - Z_2}{Z} \tag{2.5}$$

Likewise, the neutron asymmetry coordinate

$$\eta_N = \frac{N_1 - N_2}{N}, \tag{2.6}$$

Here A, Z and N refer to the mass, charge and the neutron number of the decaying parent nucleus. The range of η is within $0 \leq |\eta| \leq 1$ which provides a collective explanation of a few-nucleon, multi-nucleon (a cluster) transfer, the complete fusion ($|\eta| = 1$) of nuclei and the symmetric ($\eta = 0$), asymmetric and super-asymmetric fragmentation of the decaying nucleus. In the present work, symmetric/asymmetric and super-asymmetric fragmentation refers to the fission, cluster decay and α-decay respectively.

In the next subsection, stationary Schrödinger wave equation is used to calculate the preformation factor (P_0) which in turn is used to estimate the cross-sections σ and half-lives $T_{1/2}$ of the decay products.

2.4.1 Time Independent Schrödinger wave equation and the determination of Preformation Probability $\mathbf{P_0}$

Within QMFT, the collective Hamiltonian can be expressed by:

$$H = K(\mathbf{R}, \beta, \varepsilon, \eta, \eta_Z; \dot{\mathbf{R}}, \dot{\beta}, \dot{\varepsilon}, \dot{\eta}, \dot{\eta}_Z) + V(\mathbf{R}, \beta, \varepsilon, \eta, \eta_Z). \tag{2.7}$$

where K corresponds to the kinetic energy term and V refers to the potential energy. β stands for deformation parameter having orders upto '4' i.e. hexadecapole deformations ($\beta_{\lambda 1}$ and $\beta_{\lambda 2}$; λ=2,3,4) in the present work. However, λ may go beyond 4 and such assignment can be undertaken as a future problem. The neck parameter is pre-assumed to be zero i.e $\epsilon = 0$ due the reason that fission is an unstoppable phenomenon, so the compound/parent nucleus formation may ultimately leads to the scission stage. For the potential $V(\eta, \eta_Z, R)$, minimized in the η_Z co-ordinate, Schrödinger wave equation in terms of η and R co-ordinates is expressed as:

$$H(\eta, R)\psi(\eta, R) = E(\eta, R)\psi(\eta, R) \tag{2.8}$$

having the Hamiltonian,

$$H(\eta, R) = K(\eta) + K(R) + K(\eta, R) + V(\eta) + V(R) + V(\eta, R) \tag{2.9}$$

Therefore, in a decoupled approximation [29], expanding the η and R components separately, the Schrödinger Eq. (2.9) can be solved using Hamiltonian:

$$H = \overbrace{-\frac{\hbar^2}{2\sqrt{B_{\eta\eta}}}\frac{\partial}{\partial\eta}\frac{1}{\sqrt{B_{\eta\eta}}}\frac{\partial}{\partial\eta} - \frac{\hbar^2}{2\sqrt{B_{RR}}}\frac{\partial}{\partial R}\frac{1}{\sqrt{B_{RR}}}\frac{\partial}{\partial R}}^{\text{Kinetic Energy Term}} + \overbrace{V_R(\eta) + V_\eta(R)}^{\text{Potential Energy Term}} . \tag{2.10}$$

Here, $\mathrm{V}_R(\eta)$ and $\mathrm{V}_\eta(\mathrm{R})$ are the respective potentials corresponding to η and R motion which are later described as fragmentation potential and scattering potential in Sec

2.4.3 and 2.5. Further, for decoupled Hamiltonian, Schrödinger wave Eq. (2.10) can be segregated as

$$\left[-\frac{\hbar^2}{2\sqrt{B_{\eta\eta}}}\frac{\partial}{\partial\eta}\frac{1}{\sqrt{B_{\eta\eta}}}\frac{\partial}{\partial\eta}+V(\eta)\right]\psi^{\nu}(\eta)=E^{\nu}_{\eta}\psi^{\nu}(\eta) \tag{2.11}$$

&

$$\left[-\frac{\hbar^2}{2\sqrt{B_{RR}}}\frac{\partial}{\partial R}\frac{1}{\sqrt{B_{RR}}}\frac{\partial}{\partial R}+V(R)\right]\psi^{\nu}(R)=E^{\nu}_{R}\psi^{\nu}(R) \tag{2.12}$$

having

$$\psi(\eta,R)=\psi(\eta)\psi(R) \tag{2.13}$$

&

$$E=E_{\eta}+E_{R} \tag{2.14}$$

Here, $B_{\eta\eta}$ represents the mass parameters depicting the kinetic energy term, discussed later in Sec 2.4.2. The states $\psi^{\nu}(\eta)$ are the vibrational states in the potential $V(\eta)$ and are labelled by the quantum numbers $\nu=0,1,2,....$ referring to ground state (ν=0) and excited state solutions. The Schrödinger equation in mass asymmetry component η can be solved after the proper inclusion of Hamiltonian. The numerical solution of Eq. (2.11) results into the preformation probability (P_0). The same is calculated by solving square of wave function $|\psi^{\nu}(\eta)|^2$ simply as:

$$P_0(A_2)\propto|\psi^{\nu}(A_2)|^2 \tag{2.15}$$

Starting from the radioactive nuclei decaying via spontaneous fission or cluster radioactivity/α-emission, only the lowest state i.e. $\nu=0$ is occupied. The higher values of ν come into picture only for excited state solutions. For such situations, the preformation distribution, proportional to the probability $|\psi^{(0)}(\eta)|^2$ of finding a decay channel η at a distance R on the decay path is given by:

$$P_0=|\psi^{(0)}_{R}(A_2)|^2\frac{2}{A}\sqrt{B_{\eta\eta}(A_2)}). \tag{2.16}$$

Here, "2" represents the normalization factor which is 200% (in terms of yield); expressing the sum of preformation yield of all the possible outgoing fragments. Hence, the expression for the preformation yield in PCM/DCM reads as

$$Yield = |\psi_R^{(0)}(A_2)|^2 \frac{200}{A/2} \sqrt{B_{\eta\eta}(A_2)}). \tag{2.17}$$

Here, the temperature dependence is incorporated by assuming a Boltzmann like occupation of higher vibrational states for the addressal of excited state decays.

$$|\psi(\eta)|^2 = \sum_{\nu=0}^{\infty} |\psi^{\nu}(\eta)|^2 \exp\left(-\frac{E_\eta^\nu}{T}\right) \tag{2.18}$$

Temperature T is calculated in terms of excitation energy of the compound nucleus i.e. by the following relation:

$$E_{CN}^* = E_{cm} + Q = \frac{A}{9}T^2 - T \tag{2.19}$$

However, for ground state decays, the temperature effects remain silent within PCM. Note that we are dealing here with a directly measurable quantity, the mass asymmetry, which works dynamically as mass transfer coordinate. Thus, the calculated distribution yields $P_0(A_i)$ are directly comparable with experiments via their structural behavior. The classical hydrodynamical mass parameters $B_{\eta\eta}$ used in Eq. (2.16), are discussed in the next subsection.

2.4.2 Classical Hydrodynamical Mass Parameters

The mass parameters B_{ij}, describing the kinetic energy term K in Eqs. (2.11) and (2.12) can be calculated using cranking masses within the Asymmetric Two-Center Shell Model ($ATCSM$) [3,4] or the classical hydrodynamical masses of Kröger and Scheid [30], which find good comparison with the microscopic cranking mass outcomes. The coupling term of the kinetic energy $K(\eta, R)$, proportional to $\frac{\partial^2}{\partial\eta\partial R}$, is neglected here, since the coupled

cranking masses are very small [26,27], ($B_{R\eta} \ll (B_{RR}B_{\eta\eta})^{1/2}$ and $B_{R\eta_Z} \ll (B_{RR}B_{\eta_Z\eta_Z})^{1/2}$). The same negligence is valid for the coupling term in case of potential energy $V(\eta, R)$. The mass parameters of Kröger and Scheid are based on the hydrodynamical flow which provides a simple analytical expression as:

$$B_{\eta\eta} = \frac{AmR^2}{4}\left[\frac{v_t(1+\gamma)}{v_c(1+\delta^2)} - 1\right] \tag{2.20}$$

with

$$\gamma = \frac{R_c}{2R}\left[\frac{1}{1+\cos\vartheta_1}\left(1-\frac{R_c}{R_1}\right) + \frac{1}{1+\cos\vartheta_2}\left(1-\frac{R_c}{R_2}\right)\right] \tag{2.21}$$

$$\delta = \frac{1}{2R}\left[(1-\cos\vartheta_1)(R_1-R_c) + (1-\cos\vartheta_2)(R_2-R_c)\right] \tag{2.22}$$

$$v_c = \pi R_c^2 R \tag{2.23}$$

The angles ϑ_1 and ϑ_2 are zero and $\delta = 0$ signifies that the two spheres are in touching configuration. $R_c(\neq 0)$ is the radius of a cylinder of length R, having mass flowing in it homogenously; whose presence is estimated as the mass transfer between the two spherical fragments. The same formalism has been generalized for calculating mass parameters in case of deformed systems by using the radii R_1 and R_2, given by Eq. (2.25) ahead. The another important quantity along with $B_{\eta\eta}$, in the calculation of P_0 is the fragmentation potential ($V_R(\eta)$) which is discussed in the next subsection.

2.4.3 The Fragmentation Potential $V(\eta)$

The fragmentation potential $V_R(\eta)$, appearing in Eq. (2.11), is expressed as,

$$\begin{aligned} V(\eta, R, \ell, T) &= -\sum_{i=1}^{2} B_i(A_i, Z_i, \beta_{\lambda i}, T) + V_c(R, Z_i, \beta_{\lambda i}, \theta_i, \phi, T) \\ &+ V_p(R, A_i, \beta_{\lambda i}, \theta_i, \phi, T) + \underbrace{V_\ell(R, A_i, \beta_{\lambda i}, \theta_i, \phi, T)}_{\ell\text{=0 for spontaneous decays}} \end{aligned} \tag{2.24}$$

Here, the first term indicates the binding energy component; V_C, V_P and V_ℓ represent the Coulomb, proximity and centrifugal potentials to be discussed later. Note that the above

equation is generalized for both ground state as well as excited state decay mechanisms, hence, while applying it for spontaneous decays, the temperature and V_ℓ will be neglected. The fragmentation potential $V(\eta)$, is calculated at a fixed distance $R = R_1 + R_2 + \Delta R$ where R is defined after the inclusion of deformations as:

$$R_i(\alpha_i, T) = R_{0i}(T)[1 + \sum_\lambda \beta_{\lambda i} Y_\lambda^{(0)}(\alpha_i)], \tag{2.25}$$

and the temperature dependence in radius expression within DCM is incorporated as:

$$R_{0i}(T) = [1.28A_i^{1/3} - 0.76 + 0.8A_i^{-1/3}] \times (1 + 0.0007T^2). \tag{2.26}$$

The charges Z_i in Eq. (2.24) are decided by minimizing the total potential $V(\eta)$, in the η_Z coordinate at each η-value. Here in Eq. (2.25), λ=2,3,4 in the present work and α_i denotes the angle between the radius vector R_i of the colliding nuclei and the symmetry axis in clockwise direction. Another choice of radius comes into picture if we allow the surface effects into consideration, this is known as Sussmann's Central Radius (C_i) and reads as:

$$C_i = R_i - \frac{1}{R_i} \tag{2.27}$$

The comparison of effective sharp radius (R_i) and Sussmann central radius (C_i) [31] is made in Chapter 5 of the present work in order to find the favorable choice of radius in a particular decay modes such as spontaneous fission. The different potential components/terms used in Eq. (2.24) are discussed ahead for better clarification of the methodology used.

2.4.4 Binding energies

B_i (i=1,2) appearing in Eq. (2.24), are the binding energies of the two emitting nuclei, compiled from the experimental data of Audi-Wapstra [32] and the theoretical binding energy estimates of Möller *et al.* [33] (wherever the experimental B's are not available). It

is to be noted that the binding energies consist of liquid drop term (macroscopic) and the shell correction term (microscopic) within the Strutinsky renormalization procedure [34] as:

$$B(T) = V_{LDM}(T) + \delta U exp\bigg(- \frac{T^2}{{T_0}^2}\bigg). \tag{2.28}$$

The T dependent liquid drop part of the binding energy $V_{LDM}(T)$ is taken from Davidson *et al.* [35]. It is worth mentioning here that for the ground state calculations, the total binding energies are incorporated in PCM as it is from the tables of [32, 33], assuming that the value of B's in the mentioned tables already contain the liquid drop term and the shell correction potential energies. However, in DCM, first of all, these B's are made Temperature-dependent as per the above Eq. (2.28) as a result of which total potential $V_R(\eta)$ is calculated for excited state decays.

The shell correction term seem to be an essential term in evaluating the nuclear masses. Generally, the microscopic shell correction part, together with the liquid drop component, provide a precise explanation of the binding energy acquired by the nuclear system. The impact of shell correction term reduces with increase in temperature and generally follow the hot orientation criteria. Whereas, cold fragmentation refers to the situation where shell effects are extremely important. An increase in the temperature component in decay dynamics of any nucleus leads to the disappearance of shell effects. A descriptive example of the same is discussed in the results of Chapter 3, where the preformation profile of ^{114}Ba is illustrated to compare the T=0 and T$\neq$0 decays; thereby signifying the role of shell effects along with the temperature dependence in it.

2.4.5 The Coulomb potential

Coulomb potential tells about the repulsive forces acting between two interacting nuclei due to their charges, either in colliding configuration or in emission channel. It acts along the line joining the two nuclei. The Coulomb potential for two interacting sphere nuclei

is expressed by:

$$V_c = \frac{Z_1 Z_2 e^2}{R} \tag{2.29}$$

However, in case of deformed and oriented systems, the modified expression of V_C is given as:

$$V_c(Z_i, \beta_{\lambda i}, \theta_i, T) = \frac{Z_1 Z_2 e^2}{R(T)} + 3 Z_1 Z_2 e^2 \sum_{\lambda, i=1,2} \frac{R_i^{\lambda}(\alpha_i, T)}{(2\lambda+1) R(T)^{\lambda+1}} Y_{\lambda}^{(0)}(\theta_i) \left[\beta_{\lambda i} + \frac{4}{7} \beta_{\lambda i}^2 Y_{\lambda}^{(0)}(\theta_i)\right], \tag{2.30}$$

with R_i from Eq. (2.25). $Y_{\lambda}^{(0)}(\theta_i)$ are the spherical harmonics function.

2.4.6 The Proximity Potential

When the surfaces of two nuclei experience each other's effective field within a small distance (say, approx. 2 fm) comparable to their surface thickness, then the surface energy term alone is not enough to address the interaction between the two. Henceforth, an additional interaction comes into picture. Such an additional attractive force existing between the interacting nuclei is known as proximity force and the potential corresponding to this force is defined as the proximity potential.

Blocki *et al.* [36] have re-examined and extended a formula, according to which the potential between two surfaces in close proximity is proportional to the interaction potential per unit area between the two flat surfaces. The original expression of Blocki based on the pocket formula was for spherical nuclei, and is given by

$$V_P(s_0) = f(sh., geo.)\Phi(s_0) = 4\pi \bar{R} \gamma b \Phi(s_0). \tag{2.31}$$

Here, $\overline{R}$ is the mean curvature radius of the outgoing channel which for spherical nuclei

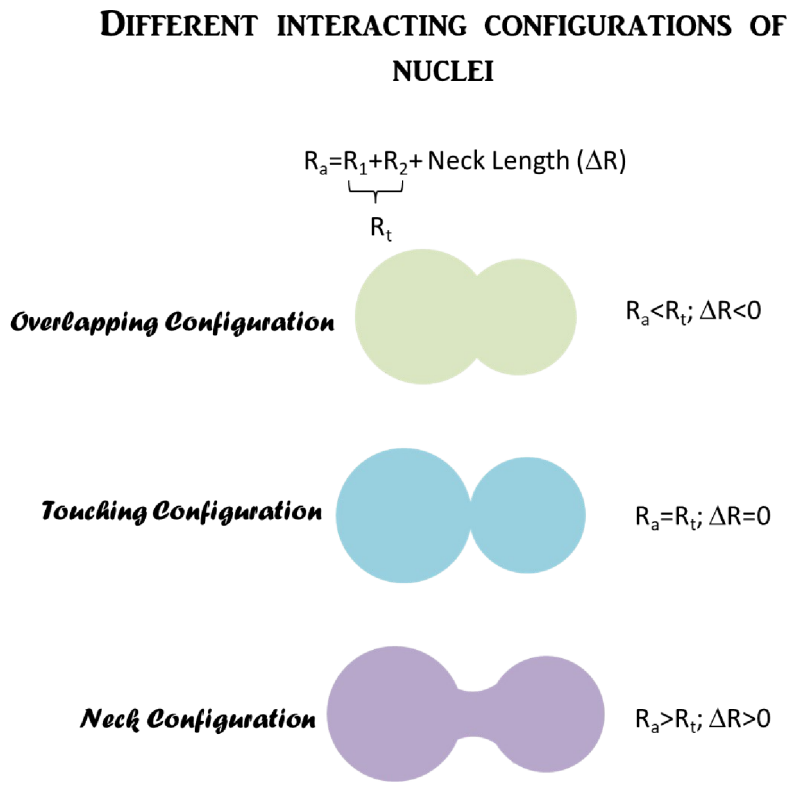

Figure 2.2 Pictorial description of two interacting nuclei having three different configurations explained in terms of neck length parameter ΔR.

reads as:

$$\overline{R} = \frac{R_1 R_2}{R_1 + R_2} \tag{2.32}$$

Eq. (2.31) is valid for zero (touching configuration) and positive values of s_0, but is also applied for negative s_0 as studied in results of Chapter 5 in discussion of spontaneous fission. $\Phi(s_0)$ is the universal function which is independent of the shapes of nuclei but depends on the minimum separation distance s_0, as

$$\Phi(s_0) = \begin{cases} -\frac{1}{2}(s_0 - 2.54)^2 - 0.0852(s_0 - 2.54)^3 \\ -3.437 exp(-\frac{s_0}{0.75}) \end{cases} \tag{2.33}$$

respectively, for $s_0 \leq 1.2511$ and $s_0 \geq 1.2511$. Here, s_0 is defined in units of b, i.e. s_0 is s_0/b, where b is the diffuseness parameter. This function is defined for negative (the overlap region), zero (touching configuration) and positive (neck region) values of s_0 as

depicted in Fig. 2.2. For a fixed R, the minimum distance s_0 is defined as

$$s_0 = R - R_1 - R_2 \tag{2.34}$$

where R_i is defined in Eq. (2.25). b is the diffuseness of the nuclear surface given by

$$b = \left[\pi/2\sqrt{3}\ln 9\right]_{t_{10-90}} \tag{2.35}$$

where t_{10-90} is the thickness of the surface in which the density profile changes from 90% to 10%. The value of b$\sim$1 fm. However, the temperature dependent diffuseness (b) within DCM for excited state decays is given as

$$b(T) = 0.99(1 + 0.009T^2) \tag{2.36}$$

The γ is the specific nuclear surface tension given by

$$\gamma = 0.9517\left[1 - 1.7826\left(\frac{N-Z}{A}\right)^2\right] MeVfm^{-2} \tag{2.37}$$

Therefore, the proximity potential [37] for decaying nuclei is given as

$$V_p(A_i, \beta_{\lambda i}, \theta_i, T) = 4\pi\bar{R}(T)\gamma b(T)\Phi(s_0(T)). \tag{2.38}$$

The above mentioned proximity of Blocki is known as Proximity-1977. Beside this, other versions of proximity potentials are also applied in chapters 3 and 4 of the thesis. These potentials include:

Proximity 1988 (Prox 88): Möller and Nix [38] improved the mass formula by changing the value of coefficients γ_0 and k_s as 1.2496 MeV fm^{-2} and 2.3, respectively. This modified version was labelled as "Proximity 1988" by Reisdorf [39]. It is to be noted that this set of coefficients give stronger attraction i.e. deeper pocket and includes stronger isospin effect as compared to Prox 77.

Modified Proximity 1988 (mod-Prox 88): Gupta *et al.* modified the value of coefficient γ_0 of Prox 1988 in order to fit the fusion cross section for the various reactions simultaneously within the extended Wong model [7]. This modified version is denoted as mod-Prox 1988. The value of coefficient γ_0 used for mod-Prox 1988 is 1.65 MeV fm^{-2}, and the remaining quantities are same as that for Prox 1988 including the universal function.

Proximity 2000 (Prox 00): Myers and Swiatecki [40] modified Eq. (2.38) by using available knowledge of nuclear radii and surface tension coefficients. For this potential, the nuclear charge radius is defined as:

$$R_{00i} = 1.24A_i^{1/3}\left(1 + \frac{1.646}{A_i} - 0.191\frac{A_i - 2Z_i}{A_i}\right) fm, \tag{2.39}$$

where $i = 1, 2$. The half-density radius, R_{0i}, was obtained from the relation:

$$R_{0i} = R_{00i}(1 - \frac{7}{2}\frac{b^2}{R_{00i}^2} - \frac{49}{8}\frac{b^4}{R_{00i}^4} + ...)(i = 1, 2). \tag{2.40}$$

Here, the universal function for Prox00 is taken from [41].

Bass 1980 (Bass 80): The universal function for this potential [42] is given by,

$$\Phi(s) = [0.033exp(\frac{s}{3.5}) + 0.007exp(\frac{s}{0.65})]^{-1}. \tag{2.41}$$

The radius vector, R_{0i} for this potential is same as Prox 77 with central radius, R_i, as

$$R_i = [(R_{0i}(T))(1 - \frac{0.98}{R_{0i}(T)^2})][1 + \sum_{\lambda}\beta_{\lambda i}Y_{\lambda}^{(0)}(\alpha_i)](i = 1, 2) \tag{2.42}$$

Ngô 1980 (Ngô 80): Ngô parameterized the nucleus-nucleus interaction potential in the spirit of proximity concept. The interaction potential is divided into the geometrical factor and a universal function. The nuclear part of the parameterized potential is written as [43]:

$$V_N^{Ngo80}(r) = \overline{R}\phi(r - C_1 - C_2)MeV \tag{2.43}$$

with

$$\overline{R} = \frac{C_1 C_2}{C_1 + C_2} \tag{2.44}$$

and

$$R_i = \frac{NR_{n_i} + ZR_{p_i}}{A_i} (i = 1, 2) \tag{2.45}$$

The details of universal function for this interaction potential is explained in [43].

2.4.7 Centrifugal Potential

Another term in the potential energy comes into picture due to the rotation of the nucleons in the excited state. This kind of additional energy due to the angular momentum ℓ, is defined as centrifugal potential or the potential caused due to angular momentum and is expressed as:

$$V_\ell(R, A_i, \beta_{\lambda i}, \theta_i, T) = \frac{\hbar^2 \ell(\ell+1)}{2I(T)} \tag{2.46}$$

where I is the moment of inertia which may be either in complete sticking limit or in non-sticking limit.

For **Sticking moment of inertia:**

$$I_s(T) = \mu R^2 + \frac{2}{5} A_1 m R_1^2(\alpha_1, T) + \frac{2}{5} A_2 m R_2^2(\alpha_2, T). \tag{2.47}$$

whereas

For **Non-Sticking moment of inertia:** $I(T)$=I_{NS}=μR^2, where $\mu = \frac{A_1 A_2}{A_1 + A_2} m$ is the reduced mass with m as the nucleon mass.

Note that the experimentally obtained value of angular momentum is based on the moment of inertia in non-sticking limit [44]. The sticking limit of moment of inertia is found to be more suitable for the calculation of fission cross-sections [45] while taking the proximity interactions into account. The implementation of sticking limit leads to larger values of angular momentum. Additionally, it is relevant to mention here that the role of V_ℓ remains silent in ground state decays since angular momentum in such cases is

negligible. Within DCM/PCM, the use of various terms- V_C, V_P and V_ℓ is also utilized to calculate the penetration probability P via determination of scattering potential which is discussed in the next section.

2.5 The Scattering Potential $V(R)$

After binary fragmentation, for a fixed decay channel A_1+A_2 (η), the scattering potential $V(R)$ is calculated which is expressed as the sum of Coulomb, proximity and angular momentum-dependent potentials, where temperature, deformation and orientation effects are duly incorporated through radius term defined in Eq. (2.25).

$$\begin{aligned} V(R,\ell,T) &= V_c(R,Z_i,\beta_{\lambda i},\theta_i,\phi,T)+V_p(R,A_i,\beta_{\lambda i},\theta_i,\phi,T) \\ &+ \underbrace{V_\ell(R,A_i,\beta_{\lambda i},\theta_i,\phi,T)}_{\ell\texttt{=0 for spontaneous decays}} \end{aligned} \tag{2.48}$$

The above scattering potential describes the tunnelling path of decay channel through the potential barrier and hence consequently, results in the estimation of penetrability P of the decay fragments. Here also, the term V_ℓ within PCM will remain silent for spontaneous decays due to $\ell = 0\hbar$.

2.5.1 Penetration Probability P

For R-motion, in place of solving the Schrödinger Eq. (2.12), we apply the WKB approximation to determine the penetration probability P. As far as the use of mass parameter B_{RR} is concerned, the effective mass B_{RR} is found to be nearly similar to reduced mass for incompressible irrotational approach [46]. Hence, instead of using B_{RR}, we are using the reduced mass μ in the calculation of the WKB penetrability P.

The scattering potential, for ^{114}Ba $\rightarrow ^{110}$Xe+^{4}He studied in [47] is shown in Fig. 2.3, evaluated by using Eq. (2.48) for spontaneous as well as excited state decays. The path of penetration and the corresponding barrier parameters are also illustrated.

Focussing on the barrier penetration of ground state parent nuclei (see Fig (b)), the first (inner) turning point R_a is fixed at $R_a = R_t + \Delta R$, where $R_t = R_1 + R_2$ in PCM. Here, the penetration probability P consists of three factors:

1. The penetrability P_a from R_a to R_i,

2. the (inner) de-excitation probability W_i at R_i and

3. the penetrability P_b from R_i to R_b

giving the resultant as

$$P = P_a W_i P_b. \tag{2.49}$$

From the excitation model of M. Greiner and W. Scheid [48], the de-excitation probability W_i is expressed as

$$W_i = \exp(-bE_i) \tag{2.50}$$

This means that the de-excitation process is confined to only a single transition. In PCM, b is taken as zero which further mens that W_i=1.

Therefore,

$$P = P_a P_b, \tag{2.51}$$

Here, P_a and P_b are estimated within WKB approximation as

$$P_a = \exp\left[-\frac{2}{\hbar}\int_{R_a}^{R_i}\{2\mu[V(R) - V(R_i)]\}^{1/2}dR\right] \tag{2.52}$$

and

$$P_b = \exp\left[-\frac{2}{\hbar}\int_{R_i}^{R_b}\{2\mu[V(R) - Q]\}^{1/2}dR\right]. \tag{2.53}$$

Here R_a and R_b are the first and second turning points respectively as shown in Fig. 2.3. This concludes that the tunneling commences at $R = R_a$ and ends at $R = R_b$, with $V(R_b) = Q$-value for spontanous decays. Such a procedure is followed for the ground

state decays, however for an excited compound nucleus, we consider

$$V(R_a) \;\; = \;\; V(R_b) = Q_{eff} = TKE + Q_{out} \tag{2.54}$$

. In DCM, P=P_b and Q_{eff} replaces Q and the limits of integration are from R_a to R_b as depicted in panel (a) of Fig. 2.3.

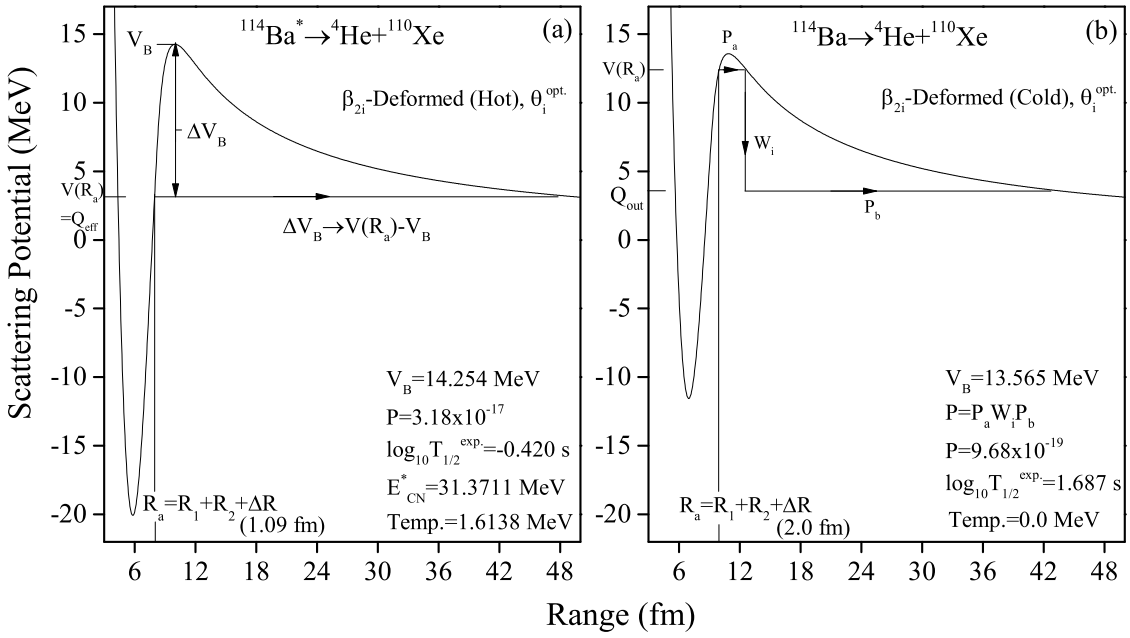

Figure 2.3 Interaction potentials calculated for the (a) excited state and (b) ground state emission of ^{114}Ba $\rightarrow$ ^{110}Xe + ^{4}He channel considering the deformed choice of fragments. Various quantities like barrier height, penetration probability, etc. are also mentioned in the panels.

Therefore P is given as

$$P = exp[-\frac{2}{\hbar}\int_{R_a}^{R_b}\{2\mu[V(R) - Q_{eff}]\}^{1/2}dR], \tag{2.55}$$

After the formation of a barrier, various barrier characteristics are found to be responsible for the variation in resultant half-lives or decay cross-sections. These barrier parameters include V_B, R_B, $V(R_a)$, R_a, ΔV_B etc. and are discussed in the section 2.5.2 ahead.

2.5.2 Barrier Characteristics

For the decay of a nucleus, we select the first turning point as

$$R_a(T) = R_t + \Delta R(\eta, T) \tag{2.56}$$

where

$$R_t = R_1(\alpha_1, T) + R_2(\alpha_1, T) \tag{2.57}$$

$\Delta R(T)$ is the relative internuclear separation between two fragments A_i and refers to the neck-length parameter that incorporates the neck formation effects. Both the scission-point [49] and saddle-point [50,51] statistical fission models consider such kind of inclusion of a neck length parameter. The R_i are radius vectors which are also made temperature dependent, given by Eqs.(2.25) and (2.26).

In order to explain various decay mechanisms using collective clusterization approach, the entry point (barrier position) is modified in view of the available experimental data on cross-sections and half-lives. Such modification leads to automatic origin of index of barrier lowering, ΔV_B, defined as in Eq. (2.58). This feature of 'lowering of barriers' (without altering the depth of potential pocket) for both ground state and excited state decays arise in PCM/DCM due to corresponding changes in neck-length parameter ΔR. In other words, it is defined as the difference between V_B and $V(R_a)$, the barrier height and the actually used barrier, as:

$$\Delta V_B = V(R_a) - V_B. \tag{2.58}$$

and is termed as 'Barrier Modification parameter'. Note that, ΔV_B for excited state decays will be different for each ℓ-value and is defined as a negative quantity since the actual barrier height is effectively lowered. Generally, it is found that the parameter ΔV_B is higher in magnitude for spontaneous decays in comparison to the excited state decays [52]. This result, along with the relevant description is discussed in Chapter 6 of

the thesis.

Next, the results extracted using this methodology are presented in the upcoming chapters. To start with, the next Chapter 3 presents a detailed analysis of α-radioactivity which is worked out in the domain of trans-tin nuclei.

Bibliography

[1] X. J. Bao, S. Q. Guo, H. F. Zhang, Y. Z. Xing, J. M. Dong and J. Q. Li, J. Phys. G: Nucl. Part. Phys. **42**, 085101 (2015).

[2] C. Xu, Z. Ren, Y. Guo, Phys. Rev. C, **78** 044329 (2008).

[3] J. Maruhn and W. Greiner, Phys. Rev. L **32**, 10 (1974).

[4] R. K. Gupta, W. Scheid and W. Greiner, Phys. Rev. L **35**, 6 (1975).

[5] D. N. Poenaru, M. Ivascu and W. Greiner, Int. J. Rad. Appl. Instrum. D, Vol. **12**, No. 1-6, pp. 313-316 (1986).

[6] D. N. Poenaru, W. Greiner and E. Hourani, Phys. Rev. C **51**, 2 (1995).

[7] R. K. Gupta, R. Kumar, N. K. Dhiman, M. Balasubramaniam, W. Scheid and C. Beck, Phys. Rev. C **68**, 014610 (2003).

[8] M. Balasubramaniam, R. Kumar, R. K. Gupta, C. Beck and W. Scheid, J. Phys. G **29**, 2703 (2003).

[9] R. K. Gupta, M. Balasubramaniam, R. Kumar, D. Singh and C. Beck, Nucl. Phys. A **738**, 479c (2004).

[10] S. S. Malik and R. K. Gupta, Phys. Rev. C **39**, 5 (1989).

[11] S. Kumar, D. Bir, R. K. Gupta, Phys. Rev. C **51**, 4 (1995).

[12] S. Kumar, J. S. Batra, R. K. Gupta, J. Phys. G: Nucl. Part. Phys. **22**, 215 (1996).

[13] S. Kumar, R. K. Gupta, Phys. Rev. C **49**, 1922 (1994).

[14] S. Kumar, D. Bir, R. K. Gupta, Phys. Rev. C **51**, 1762 (1995).

[15] S. K. Arun, R. K. Gupta, B. B. Singh, S. Kanwar, M. K. Sharma, Phys. Rev. C **79**, 064616 (2009).

[16] S. K. Arun, R. K. Gupta, S. Kanwar, B. B. Singh, M. K. Sharma, Phys. Rev. C **80**, 034317 (2009).

[17] G. Sawhney, M. K. Sharma, R. K. Gupta, Phys. Rev. C **83**, 064610 (2011).

[18] R. Kumar, M. K. Sharma, Phys. Rev. C **85**, 054612 (2012).

[19] R. Kumar, Phys. Rev. C **86**, 044612 (2012).

[20] G. Sawhney, G. Kaur, M. K. Sharma and R. K. Gupta, Phys. Rev. C **88**, 034603 (2013).

[21] M. Kaur, M. K. Sharma and R. K. Gupta, Phys. Rev. C **86**, 064610 (2012).

[22] R. Mittal, D. Jain and M. K. Sharma, Nucl. Phys. A **968**, 436-452 (2017).

[23] N. Grover, G. Kaur and M. K. Sharma, Phys. Rev. C **93**, 014603 (2016).

[24] M. Kaur and M. K. Sharma, Phys. Rev. C **85**, 054605 (2012).

[25] G. Gamow, ZP **51**, 204 (1928).

[26] J. Maruhn and W. Greiner, Phys. Rev. Lett. **32**, 548 (1974).

[27] R. K. Gupta, W. Scheid, and W. Greiner, Phys. Rev. Lett. **35**, 353 (1975).

[28] H. J. Fink, W. Greiner, R. K. Gupta, S. Liran, J. H. Maruhn, W. Scheid, and O. Zohni, in Proceedings of Int. Conf. on Reaction between Complex Nuclei, Nashville, 1974, 21, (Amsterdam: North Holland), pages 2.

[29] R. K. Gupta, IANCAS Bull. (India), **6**, 2 (1990).

[30] H. Kröger and W. Scheid, J. Phys. G **6**, L85 (1980).

[31] G. S*ü*ssmann, Z. Phys. A **274**, 145 (1975).

[32] G. Audi, A. H. Wapstra and C. Thibault, Nucl. Phys. A **729**, 337 (2003).

[33] P. Möller, J. R. Nix, W. D. Myers, and W. J. Swiatecki, At. Data Nucl. Data Tables **59**, 185 (1995).

[34] V. M. Strutinsky, Nucl. Phys. A **95**, 420 (1967).

[35] N. J. Davidson, S. S. Hsiao, J. Markram, H. G. Miller, and Y. Tzeng, Nucl. Phys. A **570**, 61c (1994).

[36] J. Blocki, J. Randrup, W. J. Swiatecki, and C. F. Tsang, Ann. Phys. (NY) **105**, 427 (1977).

[37] R. K. Gupta, M. Balasubramaniam, R. Kumar, N. Singh, M. Manhas, and W. Greiner, J. Phys. G: Nucl. Part. Phys. C **31**, 631 (2005).

[38] P. Moller and J. R. Nix, Nucl. Phys. A **361**, 117 (1981).

[39] W. Reisdorf, J. Phys. G: Nucl. Part. Phys. **20**, 1297 (1994).

[40] W. D. Myers and W. J. Swiatecki, Phys. Rev. C **62**, 044610 (2000).

[41] W. D. Myers and W. J. Swiatecki, Ann. Phys. **55**, 395 (1969); Nucl. Phys. A **336**, 267 (1980).

[42] W. Reisdorf, J. Phys. G: Nucl. Part. Phys. **20**, (1994) 1297.

[43] H. Ngô and C. Ngô, Nucl. Phys. A **348** 140 (1980).

[44] S. Kailas (private communication).

[45] M. K. Sharma, G. Sawhney, R. K. Gupta, and W. Greiner, J. Phys. G: Nucl. Part. Phys. **38**, 105101 (2011); M. K. Sharma, G. Sawhney, S. Kanwar, and R. K. Gupta, Mod. Phys. Lett. A **25**, 2022 (2010).

[46] D. N. Poenaru, R. A. Gherghescu and W. Greiner, Eur. Phys. J. A **24**, 355 (2005).

[47] K. Sharma and M. K. Sharma, Nucl. Phys. A **986**, 1 (2019).

[48] M. Greiner and W. Scheid, J. Phys. G: Nucl. Phys. **12** L229 (1986).

[49] T. Matsuse, C. Beck, R. Nouicer, and D. Mahboub, Phys. Rev. C **55**, 1380 (1997).

[50] S. J. Sanders, D. G. Kovar, B. B. Back, C. Beck, D. J. Henderson, R. V. F. Janssens, T. F. Wang, and B. D. Wilkins, Phys. Rev. C **40**, 2091 (1989).

[51] S. J. Sanders, Phys. Rev. C **44**, 2676 (1991).

[52] K. Sharma, G. Sawhney, M. K. Sharma and R. K. Gupta, Nucl. Phys. A **972**, 1 (2018).

Chapter 3

α-decay analysis of trans-tin nuclei

3.1 Introduction

Alpha decay is historically the first observed radioactivity which provides some important information about the mass and structure of nucleus. Also, it has proven to be a valuable tool to explore the low-energy structure of neutron-deficient nuclei near magic shell closures [1]. It is evidently confirmed that the N, Z=50 shell closures are related to ^{100}Sn due to the existence of an island of α-decay in the neutron-deficient Sn-region. In view of classical Gamow picture, it was concluded that the α-particle is supposed to be preformed within the parent nucleus with a certain preformation factor and leak through the Coulomb barrier, generated by the electrostatic interaction of the α-particle with the constituent protons of the daughter product. The α-decay theory formulated by Gamow, Gurney and Condon on the basis of quantum tunnelling, was one of the early achievements in quantum mechanics. Later on, as an outcome of this pioneering study, various theoretical investigations were carried out for better understanding of α-decay mechanism. These studies are based on various microscopic, macroscopic, cluster and fission approaches [2–9] and adequately address the process of α-emission. Many times, α-decay leads to doubly magic ^{208}Pb or ^{100}Sn, which are highly stable against these kind of emissions and consequently affect the corresponding half life times of the parent system.

The doubly magic ^{100}Sn is the heaviest N=Z nucleus (N=Z=50) produced and studied so far. Therefore, it is of great interest to explore the isotopes of elements neighboring to ^{100}Sn i.e. Te, I, Xe, etc. as their lightest isotope decays through α-emission mode, either spontaneously or may be induced by the excitation of the nucleus or via some subsequent α-decay chains.

These neutron-deficient systems are very fascinating because they are located very close to the N=Z line. Important feature of such a study is that one of the fragment always belongs to spherically closed shell nucleus ^{4}He. The deformation parameters of the parent and daughter nuclei which further change the barrier characteristics, play a vital role in addressing this novel process of α-decay. Interestingly, in the present study, all the considered parent and daughter systems are prolate deformed thereby signifying the indispensable role of deformations in the decay of such ground state nuclei. Several theoretical formalisms considering parent and daughter ground state (GS) deformations are established, like unified model for α-decay and α-capture [10], generalized density-dependent cluster model [11], coupled channel studies [12], preformed cluster model [13] and Coulomb and proximity potential model for deformed nuclei [14], which exhibit the lowering of barrier height after the inclusion of deformation effects. The key constituent of these formalisms is the nuclear potential, which comprises of long-range and short-range contributions. The short-range interaction potential is the backbone of all the theoretical formalisms. Various versions of nuclear potentials are available in literature. Some of them have been studied in the previous studies of Preformed Cluster-decay Model (PCM) [15] for the addressal of different nuclear phenomenon such as cluster radioactivity, fusion, etc. For the overall understanding of α-emission process, a proper understanding of the barrier characteristics is extremely desirable, as the preformation and penetration probabilities depend significantly on the configuration of nuclear potential. In the present work, various nuclear proximity potentials such as Prox77 [16], Prox88 [17, 18], Prox00 [19, 20], Mod-prox88 [31], Prox Ngo80 [21] and Bass 1980 [18] having different barrier characteristics are used in the analysis. It is relevant to mention that, PCM carries the structural

information of the decaying nuclear system via the preformation factor. This approach of PCM has successfully addressed various ground state properties of the nuclei and related phenomena like cluster radioactivity [22], spontaneous fission [23], α-decay chains etc. [24] in different regions of the nuclear chart. Knowing that the PCM calculated half life ($T_{1/2}$) reflects the combined effect of preformation probability (P_0) and penetration probability (P), consequently the predicted half lives remain very sensitive to the barrier characteristics. In this chapter, the addressal of the α-decay half lives is attempted via ground state emission and excited state emission process in the trans-Sn region. Basically, the objective of this work is three folds: (i) to study the three α-decay chains, starting with ^{114}Ba and ending at ^{102}Sn with some excitation energies of the parent nuclei. (ii) to analyze the comparison between ground state and excited state α-decay in terms of their structural behavior and shell effects. (iii) to address the α-radioactivity and decay half-lives of $^{105-111}$Te, $^{107-112}$I, $^{109-113}$Xe, ^{114}Cs and ^{114}Ba ground state parent nuclei using different proximity potentials. The decay of excited nuclei is accomplished within the methodology of Dynamical Cluster-decay Model (DCM) [25, 26] whereas for that of the ground state decays, Preformed Cluster-decay Model (PCM) [13,27–29] is used. The basic difference between the DCM and PCM is that the latter is the ℓ=0 and T=0 version of the former. The main component of the two models is the nuclear potential, and hence a proper understanding of the potential barrier is very important for the comprehensive knowledge of the induced as well as the spontaneous decay processes.

Section 3.2 of this chapter, gives a detailed discussion on the calculations and results obtained. Finally, the conclusions have been summarized in Section 3.3. Note that the work of this chapter is published in [30].

3.2 Calculations and Results

It is well known that, as the number of nucleons increase above A=140, α-emission becomes the major decay mode for the heavy nuclei. Instead, the nuclei with

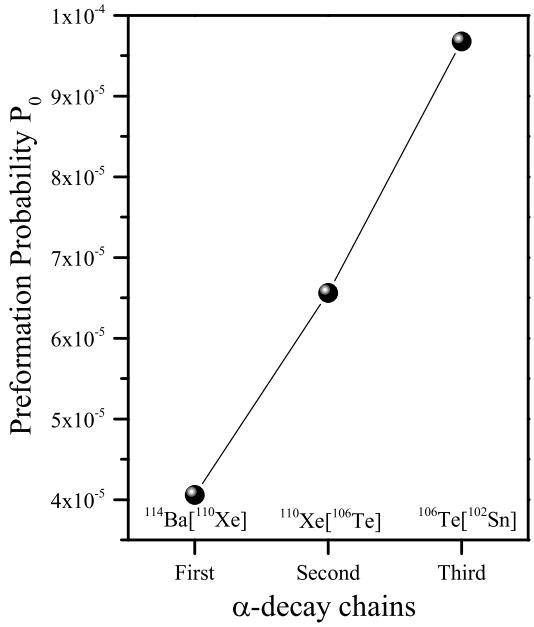

Figure 3.1 Preformation probability P_0 plotted against number of α-decay chains starting from ^{114}Ba and terminating upto ^{102}Sn. Note that the parent nuclei are marked in the figure with the emitted daughter product in square parentheses.

light mass are stable against α-decay, except the super-allowed α-decay island above the exotic doubly magic nucleus ^{100}Sn. In present work, the triple α-decay chain ^{114}Ba$\rightarrow^{110}$Xe$\rightarrow^{106}$Te$\rightarrow^{102}$Sn [32] is studied using the Dynamical cluster decay model (DCM) at the reported energy E_{Lab}=210 MeV by including different neck-length parameters, depending on the structure of the parent and daughter nuclear systems. The calculations are executed for spherical as well as quadrupole (β_2) deformed approach of fragmentation including orientation effects of the decaying nuclei. Next, the dynamics of α-decay half-lives ($T_{1/2}$) of Te, I, Xe, Cs and Ba isotopes starting from their respective N=Z isotopes is presented using Preformed Cluster decay Model (PCM). In this analysis, the role of various proximity interactions is probed in terms of barrier characteristics and the corresponding tunnelling probabilities. The behavior of the fragmentation potential, preformation profile, barrier lowering effect, etc. are analyzed so as to have a complete understanding of the nuclear structure effects involved. Similar effects for heavier nuclei such as ^{150}Dy, ^{152}Ho, ^{154}Ho and ^{154}Tm, are also explored. In addition to this, a comprehensive comparative analysis is carried out to explore the structure effects in view of

Table 3.1 DCM calculated half-lives $\log_{10}T_{1/2}$ (s) for the successive α-decay of $^{114}Ba^*$ compound system terminating upto ^{102}Sn while considering the spherical as well as deformed choice of fragments.

Compound	Decay	E^*_{CN}	Temp.	ΔR (fm)	$\log_{10}T_{1/2}$(s)			Q_α-value
Nucleus	Channel	(MeV)	(MeV)	Sph./β_2	Sph.	β_2	Expt. [32]	(MeV)
$^{114}Ba^*$	$^4He+^{110}Xe$	31.371	1.613	1.09	-4.373	-0.727	-0.420	3.546
$^{110}Xe^*$	$^4He+^{106}Te$	27.761	1.548	1.11	-4.640	-1.082	-1.022	4.606
$^{106}Te^*$	$^4He+^{102}Sn$	23.901	1.467	1.17	-6.699	-4.308	-4.154	6.016

ground state α-emission and the one occurred via triple α-decay chain.

In view of the dynamics involved in the triple α-decay chain process, the DCM, is executed in which temperature and angular momentum effects are incorporated. The DCM is applied because of the fact that triple α-decay chain emerges in the decay of $^{114}Ba^*$ nucleus, which is produced via 2n-emission of ^{116}Ba nuclear system. The calculations for 2n-emission and successive α-decays are carried out for both spherical and deformed approaches of fragments (having hot-compact configuration) and the results are compared with corresponding experimental data [32]. It is important to state that, the neck parameter (ΔR) for spherical fragmentation of 2n-emission is ΔR=1.15 fm, which increases to 1.25 fm after the inclusion of deformations effects. Table 3.1 depicts the calculated α-half life values for the decay of $^{114}Ba^*$, $^{110}Xe^*$ and $^{106}Te^*$ nuclei. The respective temperature and Q-values are also shown in the table. It is noticed that the DCM evaluated α decay lifetimes find nice agreement with the respective experimental data at corresponding neck-length values. It is important to mention here that the neck values are kept fixed independent of the choice of spherical or deformed fragmentation. It is seen that at the mentioned ΔR values, deformed approach seems to be a better option to study such kind of decays. It is to be observed that DCM calculations are sensitive to ΔR and the results for spherical approach improve for comparatively smaller neck values. However, it is evident from Table 3.1 that the value of ΔR increases as we move towards the more stable

daughter nucleus.

The penetration probability plays extremely important role to understand the dynamics of α-decays. In the present work, the penetrability is calculated using the WKB approximation as mentioned in Eq. (2.55) and Eqs. (2.52, 2.53), which is solved in terms of one step and two step tunnelling in DCM and PCM respectively. Hence, the potential calculated at first and second turning points of penetration directly depends on the Q value of the reaction as shown in Fig. 2.3 of Chapter 2. In order to analyze the behavior of preformation probability in terms of shell closure effects, Fig. 3.1 is plotted for number of α-decay chains starting from ^{114}Ba and terminating at ^{102}Sn. The effect of N=Z=50 is evident in terms of preformation probability (P_0), as the highest preformation yield is observed for channel ^{106}Te$\rightarrow^{4}$He+^{102}Sn since it is having daughter in the vicinity of doubly magic nucleus ^{100}Sn (N=Z=50) and this channel possesses the highest Q-value. Hence, one may conclude that the half-life of ^{106}Te must be lowest as both the factors P_0 and Q-value bear inverse relation with $T_{1/2}$. Conclusively, the highest preformation yield, Q-value and consequently penetration probability for ^{106}Te is mainly because of the magicity effect.

In the above analysis, complete decay mechanism of excited ^{114}Ba* nucleus is observed through the DCM. Further, the ground state decay of ^{114}Ba is also analyzed in terms of scattering potential and preformation distribution, so that a comparison between excited and ground state decays be carried out. The difference between ground and excited state is that in the excited state of the nucleus, energy provides extra push to the nucleus for penetration through the barrier. However, the ground state penetration primarily depends on Q-value, without any extra push. In view of this, a comparison between the one step and two step penetration paths of excited and ground state α-emission respectively for ^{114}Ba nucleus decaying into ^{4}He+^{110}Xe channel is shown in Fig. 2.3 of Chapter 2. It is to be noted that the first turning point in case of excited state decays is much lower in comparison to that of the ground state decay. Furthermore, the barrier height V_B is higher for the excited state decays. This is possibly due to the

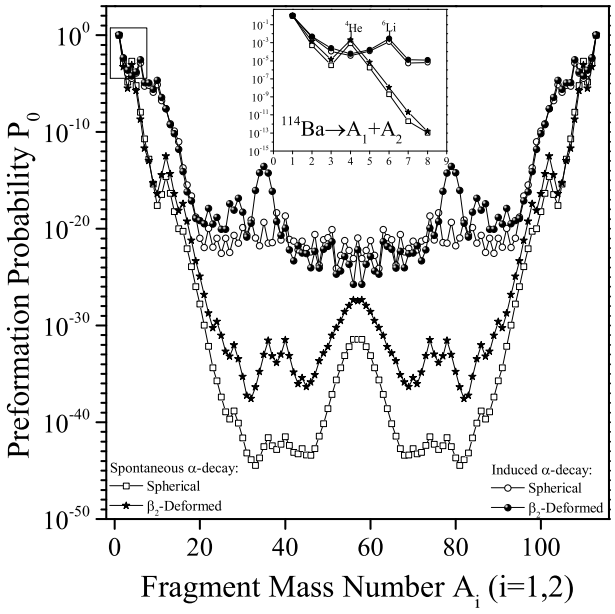

Figure 3.2 Comparison of calculated preformation distribution yields for the spontaneous and the induced α-emission for the decay of ^{114}Ba using spherical as well as deformed approach. The inset of this figure depicts the P_0 for the lighter mass region i.e. A=1-8 only.

fact that ground state processes are the cold phenomena due to which they don't need any external energy to complete the penetration process and hence possess the lower barrier height in comparison to the excited decays. As a consequence, spontaneous α-decays require much higher neck in order to tunnel across the potential barrier. Also, the tunnelling probability is seen to be higher in case of panel (a) which clearly suggests that higher the energy of the parent nucleus, penetration will be more easier. It is important to mention here that the choice of different ΔRs specifies different time scale for the decay products. In the same figure, it is mentioned that ΔR for panel (b) is much higher as compared to panel (a) which is in clear agreement with α-decay life times of the parent system ^{114}Ba. Furthermore, a comparative study of induced α-decay versus spontaneous α-emission of ^{114}Ba is carried out in terms of fragment formation yields P_0. Figure 3.2 depicts the preformation probability as a function of fragment mass number for the spontaneous and excited state α-decay of ^{114}Ba parent nucleus. In this figure, we compare the calculated fragment formation yields P_0 for ℓ=0$\hbar$ case so as to explore the importance of magic shells in mass/preformation distributions. The spontaneous and

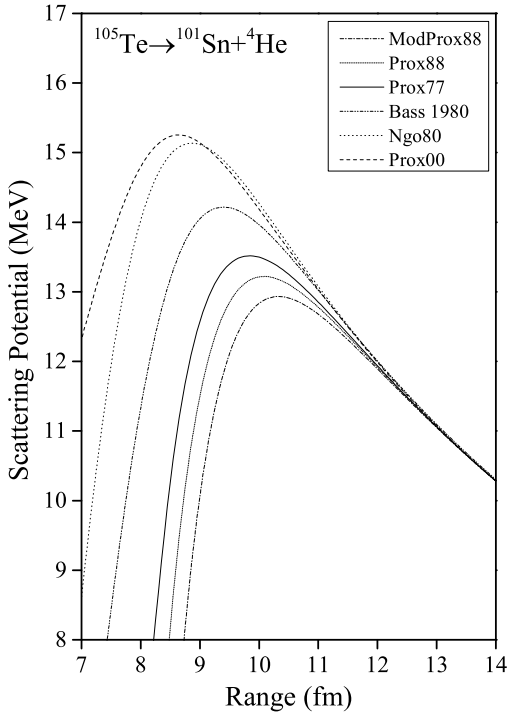

Figure 3.3 Interaction potentials calculated for the decay of ^{105}Te → ^{101}Sn + ^{4}He using various versions of nuclear proximity potentials i.e. Prox77, Prox88, Mod-Prox 88, Prox00, Prox Ngo80 and Prox Bass 1980.

induced α-decay processes show completely different structural pattern in terms of the emission of most prominent fragments, thereby indicating shell closure property of the decay fragments. For the chosen parent nucleus, the most probable fragment in lower mass region is ^{4}He for spontaneous α-emission whereas this fragment changes to ^{6}Li for induced α-decay. For a better description of the structural behavior of decaying parent nucleus in the lighter mass region, the inset of this figure displays the P_0 for A=1-8 only. It is evident that α-channel is clearly visible for spontaneous α-decays due to its high value of preformation probability in comparison to excited state decays. This might be due to the fact that the shell effects get vanished after a particular value of temperature (T_0=1.5 MeV). Or we can say that the shell effects are best visible in spontaneous decays. Moreover, the mass distribution of the decay of ^{114}Ba in the fission region changes from symmetric to asymmetric when one moves from ground state emission to the excited state decays. However, stressing on the role of deformations in the present study, it is seen that

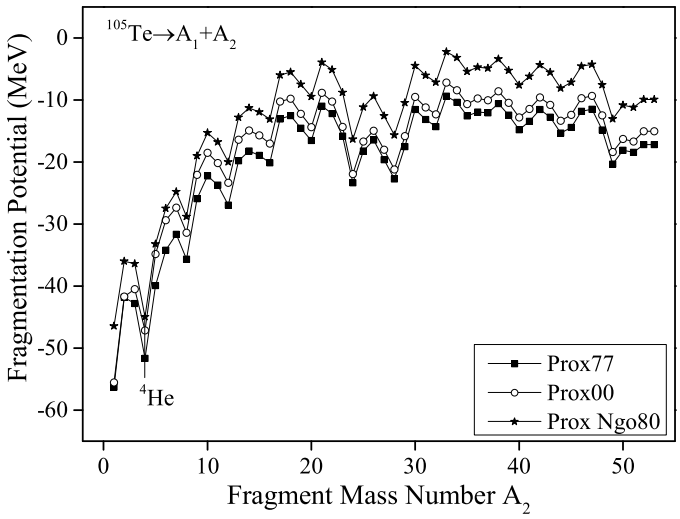

Figure 3.4 Fragmentation profile for the decay of ^{105}Te $\rightarrow$ A_1+A_2 considering Prox77, Prox00 and Prox Ngo80. Note that the angular momentum effects are kept silent for the ground state α-emission study within PCM.

the preformation factor for almost all the possible decaying fragments is higher for the deformed choice of fragmentation. The above results hold true for all the three decaying nuclei i.e. ^{114}Ba, ^{110}Xe and^{106}Te (not shown here), thereby signifying that deformations along with the shell effects play a significant role in studying clusterization process near the super-allowed region of α-decay.

Now, proceeding further, in addition to ^{114}Ba nucleus, various isotopes of Te, I, Xe, and Cs are also investigated so that the complete decay analysis of this mass region be worked out. Considering the fact that the barrier characteristics play a significant role in the penetration process, we have tried to choose the optimal potential barrier for tunnelling of the α-particle. Consequently, different choices of nuclear proximity potentials are exercised to explore the dynamics of α-radioactivity. In previous studies [15, 33], the role of various interaction potentials were used within Preformed Cluster Model to explore the cluster decay of various ground state nuclei. Out of various proximity potentials, here we started our analysis by opting 6 different potentials to study the α-emission in the trans-Sn region. To pursue this work, firstly, Fig. 3.3 is plotted for lightest nucleus ^{105}Te decaying into ^{4}He+^{101}Sn channel using Prox-77, Prox-88, Prox-00, Mod-Prox-88, Prox Ngô 80 and Prox Bass 1980 potentials to analyze the behavior of scattering potential.

Table 3.2 The PCM calculated values of barrier height V_B, first turning point R_a and second turning point R_b in the spontaneous decay of ^{105}Te considering 6 different proximity interaction potentials used in the present study.

Proximity Potential	V_B (MeV)	R_a (fm)	R_b (fm)	$R_a - R_b$ (fm)
Mod-Prox 88	12.940	8.900	15.327	6.427
Prox 88	13.229	8.400	20.184	11.784
Prox 77	13.514	8.400	15.127	6.727
Bass 1980	14.217	8.419	22.422	14.003
Prox Ngo 80	15.145	8.342	10.637	2.295
Prox 00	15.256	7.527	10.308	2.781

It may be noticed that most of the considered potentials were used in the previous studies of PCM [15] and other theoretical works based on proximity interactions such as [34]. It is evident from Fig. 3.3 that the barrier corresponding to mod-Prox 88 is lowest. The interaction potential corresponding to Prox88 and Prox77 is almost similar to that of mod Prox88 because of the slight variation in their surface energy coefficients. On the other hand, Prox Ngo80 has barrier characteristics very close to Prox00 possibly due to their effective dependence on isospin and asymmetry of the emitting nuclei. The barrier corresponding to Bass 1980 potential lies in between Prox77 and Ngo80 potential. In the present analysis, Prox00 and Prox Ngo80 turn out to be favorable than other interaction potentials considered in the current study of α-decay process. This is because of the easier penetration while using Prox 00 and Ngo 80. This fact can be further clarified from Table 3.2, which depicts the difference in the values of first and second turning points of the penetration path (shown in column V of Table 3.2). It is observed that the emitting α-particle requires less path to tunnel through the barrier while considering Prox 00 and Ngo 80 as a result of which penetration becomes much more easier in case of these two proximity potentials. Although, the overall process of α-emission doesn't depend only upon the penetration probability P, the contribution of preformation factor P_0 is

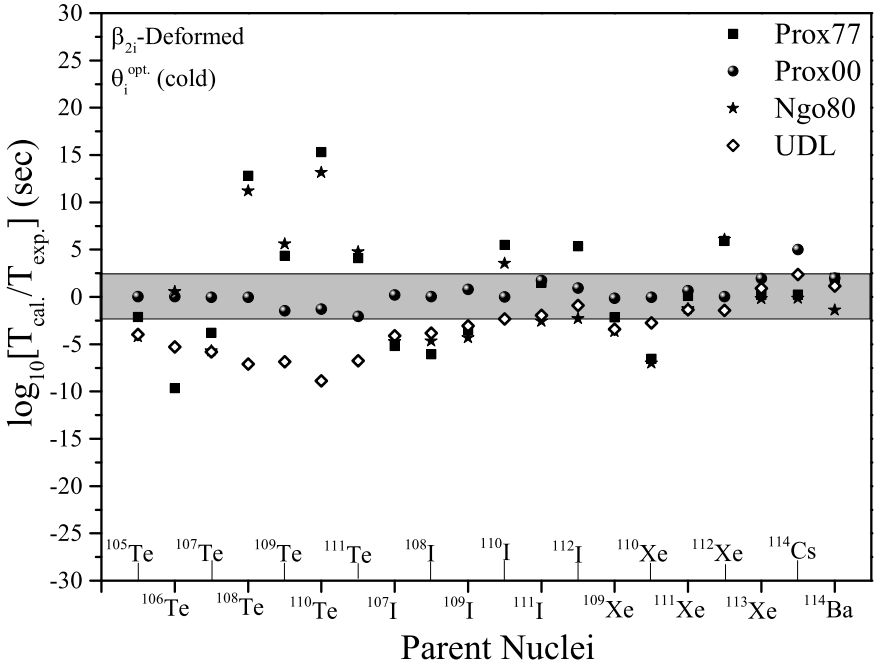

Figure 3.5 Deviations between the logarithms of PCM calculated half-lives and the experimental ones corresponding to different cases of parent nuclei while using Prox77, Prox00, Prox Ngo80 and Universal Decay Law (UDL). Here, solid square symbol, sphere, star and open diamond represent Prox77, Prox00, Prox Ngo80 and UDL respectively.

equally important, but the higher magnitude of P (in comparison to P_0) is dominating the decay process in the present scenario. Therefore, in the further calculations, only the three higher barrier proximity potentials viz. Prox77, Prox00 and Prox Ngo80 have been considered whose penetration process is comparatively easier. The reason of choosing the Prox 77 for further calculations is that it is extensively exercised in previous investigations [15, 22, 23, 35] on ground state decays within the framework of PCM.

It is relevant to mention that another interesting quantity in determining the decay constant λ or half-life $T_{1/2}$ is the preformation probability P_0, which is dependent on the fragmentation potential V(A_2). It is to be noted that the fragmentation potentials plotted in Fig. 3.4 are calculated using deformed approach within cold-optimum orientations, since the preformation probability for α-cluster is seen to be more prominent for β_2-deformed case (see Fig. 3.2). The cold orientation criteria is applied here because the temperature and angular momentum effects are silent. We concentrate only on the minima of fragmentation potential, since the clusters on the minima of fragmentation potential

correspond to the maxima in the preformation distribution. Fig. 3.4 depicts the behavior of fragmentation potential of ^{105}Te using Prox 77, Prox00 and Ngo 80 proximity potentials. It is observed that the potential energy minima appears at A_2=4n α-structure upto mass number A$\simeq$30 for the consideration of all the three potentials. ^{4}He (α-particle) is found to be the most preferred outgoing fragment from the parent system ^{105}Te and found to compete with ^{1}H in the spontaneous decay of ^{105}Te parent system. The structural profile seems to be similar for the use of different proximity potentials but there is a change in the magnitudes of their respective V_η values. It is also seen that Prox77 possesses the lowest magnitude of fragmentation potential whereas the Prox Ngo80 gives highest magnitude.

Table 3.3 The α-decay $\log_{10}T_{1/2}$(s) values on their best fitted neck-length parameters ΔR (fm) for the decay of 20 ground state parent nuclei in the trans-Sn region using three chosen proximity potentials i.e. Prox77, Prox00 and Prox Ngo80 considering only deformed approach of fragments. The outgoing channel along with the corresponding Q-values are also mentioned for all the considered parent systems.

Serial	Compound	Decay	ΔR (fm)			$\log_{10}T_{1/2}$(s)				Q-value
No.	Nucleus	Channel	Prox77	Prox Ngo80	Prox00	Prox77	Prox Ngo80	Prox00	Expt. [36]	(MeV)
1	^{105}Te	^{4}He+^{101}Sn	2.00	2.00	1.82	-8.313	-10.418	-6.169	-6.193	6.30
2	^{106}Te	^{4}He+^{102}Sn	1.30	2.00	0.685	-13.77	-3.564	-4.107	-4.129	6.01
3	^{107}Te	^{4}He+^{103}Sn	2.00	2.00	1.15	-6.111	-8.027	-2.345	-2.318	5.55
4	^{108}Te	^{4}He+^{104}Sn	1.30	2.00	0.42	-12.106	-10.507	0.669	0.690	5.02
5	^{109}Te	^{4}He+^{105}Sn	2.00	2.00	0.95	-1.976	-3.239	0.899	2.378	4.51
6	^{110}Te	^{4}He+^{106}Sn	1.30	2.00	0.27	-8.73	-6.574	5.297	6.568	4.03
7	^{111}Te	^{4}He+^{107}Sn	2.00	2.00	0.95	3.95	3.295	6.014	8.072	3.38
8	^{107}I	^{4}He+^{103}Sb	2.00	2.00	2.30	-8.732	-8.273	-3.334	-3.530	5.54
9	^{108}I	^{4}He+^{104}Sb	1.30	2.00	1.30	-7.965	-6.562	-1.856	-1.896	4.97
10	^{109}I	^{4}He+^{105}Sb	2.00	2.00	2.30	-4.253	-5.052	0.068	-0.744	4.48
11	^{110}I	^{4}He+^{106}Sb	1.30	2.00	1.87	-4.894	-2.927	0.625	0.621	4.03
12	^{111}I	^{4}He+^{107}Sb	2.00	2.00	2.30	1.157	0.110	4.435	2.685	3.58
13	^{112}I	^{4}He+^{108}Sb	1.30	2.00	2.00	0.073	3.119	6.378	5.425	3.02
14	^{109}Xe	^{4}He+^{105}Te	2.00	2.00	2.20	-3.351	-4.854	-1.341	-1.213	4.81
15	^{110}Xe	^{4}He+^{106}Te	1.30	2.00	1.10	-7.596	-8.048	-1.091	-1.044	4.60
16	^{111}Xe	^{4}He+^{107}Te	2.00	2.00	2.30	0.091	-1.270	0.636	-0.008	4.07
17	^{112}Xe	^{4}He+^{108}Te	1.30	2.00	1.46	-3.409	-3.564	2.551	2.524	3.62
18	^{113}Xe	^{4}He+^{109}Te	1.70	1.50	2.50	3.682	3.733	5.855	3.905	3.07
19	^{114}Cs	^{4}He+^{110}I	1.60	1.60	2.00	3.274	3.367	8.531	3.521	3.02
20	^{114}Ba	^{4}He+^{110}Xe	2.00	2.00	1.95	-0.34	0.282	3.669	1.687	3.54

Apart from the ground state decay of ^{105}Te where role of various proximity potentials is exercised, the relevance of selected potentials- Prox-77, Prox-00 and Prox Ngo 80 is tested for all considered ground state nuclei ranging from A=105-114. Using the preformation probability and the tunnelling probability calculated in reference to fragmentation potential and scattering potential respectively, in the decay of various isotopes of Te, I, Xe, Cs and Ba parent nuclei, the α-decay half-lives are estimated using different proximity potentials discussed in Fig. 3.4. Table 3.3 depicts the experimental half-lives and the ones calculated within PCM using Prox77, Prox00 and Prox Ngo80. It is worth stating that these $\log_{10}T_{1/2}$ values are computed at the best fitted neck-length values (also shown in Table 3.3). It is noticed that the α-decay half-life values calculated while considering Prox00 address the experimental data [36] nicely, except for some heavier nuclei. Fig. 3.5 illustrates the difference in magnitude of experimental α-decay half-lives and those calculated within PCM for all the considered ground state parents. For the sake of comparison, the α half-life values calculated using Universal Decay Law (UDL) of [37] are also shown in this figure. From this figure, it is noted that except for ^{113}Xe, ^{114}Cs and ^{114}Ba parent nuclei, Prox00 seems as a favorable option while addressing the α-radioactivity of the chosen nuclei. On the other hand, Prox Ngo80 performs better for these heavier nuclei. In addition to this, the standard rms deviation from the experimental data is determined for the studied proximity interaction potentials viz. Prox77, Prox00 and Prox Ngo80 using the following equation:

$$\sigma = \sqrt{\sum_{i=1}^{n}[log_{10}(T_i/T_{exp.})]^2/(n-1)} \tag{3.1}$$

The magnitude of standard rms deviation σ comes out as 6.366, 1.555 and 5.589 for Prox77, Prox00 and Prox Ngo80 respectively, which seems to suggest that Prox00 provides reasonable estimate of α-radioactivity in this intermediate mass region. For better description on α-decay of nuclei in trans-Sn region, nuclei heavier than Ba are also analyzed in view of the above mentioned proximity potentials. The calculations are

Table 3.4 PCM calculated α-emission half-life values for the decay of some heavier parent systems ^{150}Dy, ^{152}Ho, ^{154}Ho and ^{154}Tm for the use of Prox77, Prox00 and Prox Ngo80. The corresponding neck-length values along with the decay channel and Q-values are also mentioned in the table.

Serial	Compound	Decay	ΔR (fm)		$\log_{10}T_{1/2}$(s)			Q-value
No.	Nucleus	Channel	Prox00	Prox Ngo80	Prox00	Prox Ngo80	Expt. [36]	(MeV)
1	^{150}Dy	^{4}He+^{146}Gd	1.80	1.38	7.041	3.127	3.079	4.39
2	^{152}Ho	^{4}He+^{148}Tb	1.50	1.25	7.126	3.118	3.130	4.49
3	^{154}Ho	^{4}He+^{150}Tb	1.50	0.50	17.060	6.856	6.569	3.16
4	^{154}Tm	^{4}He+^{150}Ho	1.50	0.20	5.260	2.129	1.176	5.05

performed for the α-emission of ^{150}Dy, ^{152}Ho, ^{154}Ho and ^{154}Tm parent nuclei using Prox00 and Prox Ngo80. These potentials are chosen for the further study in reference to the results obtained from Fig. 3.5. Table 3.4 depicts the $T_{1/2}$ values for the α-decay of above mentioned nuclei using Prox00 and Prox Ngo80. It is observed that for systems heavier than the ones reported in Table 3.3, Prox Ngo80 addresses the half life values better in comparison to Prox00. This switching in the choice of proximity potentials is possibly due to the α-penetration probability which is higher in case of Prox00 upto A=112 while for the nuclei having A>112, it is larger for the use of Prox Ngo80. On the contrary, the preformation probability P_0 is consistently higher for Prox Ngo80 for all nuclei with mass A=105-114. So, Fig. 3.5 and Table 3.4 conclude that Prox00 provides better option to address the decay of lighter isotopes upto A=112 in the trans-Sn region. Whereas, for A$\geq$113, Prox Ngo80 seems better to address the α-radioactivity in the chosen region of periodic table. This fact can be further clarified by the calculations of standard deviations for two different sets of parent nuclei decaying via α-emission. In view of these calculations, the complete list of parent nuclei ranging from ^{105}Te to ^{154}Tm is divided into two regions. One region ranges from ^{105}Te to ^{112}Xe and the second one varies from ^{113}Xe to ^{154}Tm. The standard deviations corresponding to both the mass regions are calculated individually while using Prox 00 as well as Prox Ngo80 and are shown in Table 3.5.

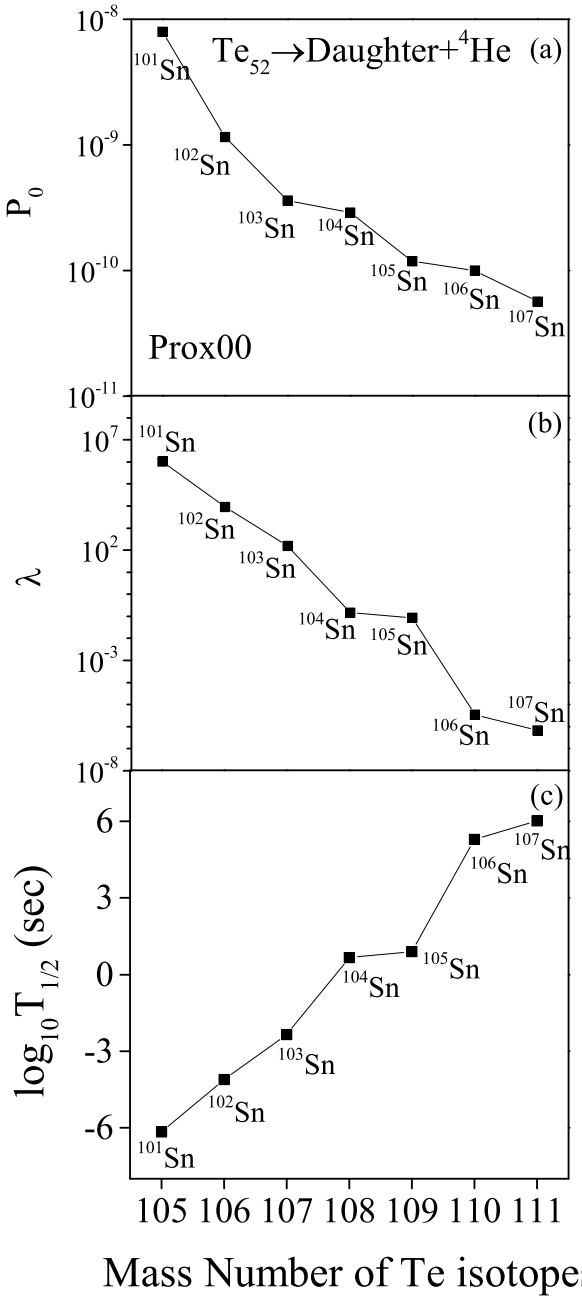

Figure 3.6 PCM calculated (a) preformation probability P_0, (b) decay constant λ and (c) half-lives $\log_{10}T_{1/2}$ (s) values for the α-decay of some isotopes of Te i.e. $^{105-111}$Te. The respective daughter nuclei emitted from different parent systems are also depicted in the figure.

Table 3.5 The calculated standard deviation values for the two mass regions for the use of Prox00 and Prox Ngo80 potentials.

Serial Number	Mass Region	Standard Deviation σ	
		Prox00	Prox Ngo80
1	^{105}Te to ^{112}Xe	0.9061	6.0804
2	^{113}Xe to ^{154}Tm	5.6455	0.7092

Furthermore, it is worth noting that the decay constant λ (or half lives $T_{1/2}$) in PCM reflects the combination of preformation probability P_0 and penetration probability P (since the assault frequency ν_0, is nearly constant $\sim 10^{21}$ s^{-1}). The behavior of P_0 along with the evaluated respective decay constant (λ) and half-life time ($T_{1/2}$) values is depicted in Fig. 3.6 for the α-decay of different isotopes of Te i.e. $^{105-111}$Te. The Te nucleus is opted to carry out the isotopic analysis, because the α half-life data is available for larger set of isotopes of Te as compared to I and Xe isotopes. It is to be noted that the daughter fragments formed in the decay of the chosen parent systems are marked in this figure. The curves in panels (a) and (b) of Fig. 3.6 are consistent i.e. P_0 and λ decrease with the increasing mass of Te nucleus. This is due to the fact that the lowest isotope of Te, ^{105}Te is decaying into ^{4}He+^{101}Sn, having daughter fragment in the vicinity of doubly magic nucleus ^{100}Sn (N=Z=50). On the contrary, ^{111}Te is decaying via α-emission having daughter ^{107}Sn which is comparatively less probable in comparison to the decay of lighter isotopes of Te. As a consequence, ^{105}Te is exhibiting the lower half-life value as shown in panel (c) of this figure. Hence, it can be remarked that shell effects are the noteworthy contributors in deciding the outgoing decay channel in the framework of clusterization process adopted in present set of calculations.

3.3 Summary

In this chapter, we have carried out the emission of α-cluster in the ground state as well as excited state decays of some trans-Sn nuclei lying near N=Z line. Firstly, the triple α-decay chain $^{114}\text{Ba}\xrightarrow{\alpha}{}^{110}\text{Xe}\xrightarrow{\alpha}{}^{106}\text{Te}\xrightarrow{\alpha}{}^{102}\text{Sn}$ is investigated, within the binary fragmentation approach of dynamical cluster decay model. The calculations have been performed for spherical as well as quadrupole deformed (β_2) approaches of decay products. It is observed that among the three parent nuclei in the successive α-decay chain, $^{106}\text{Te}\rightarrow{}^{102}\text{Sn}+\alpha$ seems the most probable decay due to the magicity of its daughter fragment. Consequently, it is the most unstable parent system among the considered nuclei. Furthermore, the α-decay half-lives of some parent nuclei lying in trans-Sn region are calculated using different nuclear proximity potentials. While analyzing the potential energy surfaces considering the three different proximity potentials- Prox77, Prox00 and Prox Ngo80, it is observed that the structure remains almost same, although some change in magnitude of fragmentation potential is evident. ^{4}He seems to compete with ^{1}H for all the ground state nuclei with A=105-114. The reported α half-lives for nuclei from ^{105}Te to ^{112}Xe are nicely addressed using Prox00, whereas for the decay of nuclei above ^{113}Xe, Prox Ngo80 seems to perform better. This switching of proximity potentials is reinforced due to the barrier penetrability of α-particle. Additionally, it has been observed that the spontaneous α-emission of all the chosen nuclei exhibit symmetric fission distribution whereas the induced α-decay shows relatively asymmetric mass distribution in the fissioning region. Moreover, the most probable fragment in lower mass region changes from ^{4}He to ^{6}Li as one moves from ground state to excited state decays because of the dissipation of shell effects at higher temperature values.

After exploring α-radioactivity in trans-Sn region, next step is to focus on another spontaneous decay mechanism termed as cluster radioactivity. The detailed description of results obtained on this rare ground state phenomenon is presented in Chapter 4.

Bibliography

[1] A. Andreyev et al., Nature (London) **405**, 430 (2000).

[2] J. P. Maharana, A. Bhagwat and Y. K. Gambhir, Phys. Rev. C **91**, 047301 (2015).

[3] K. Varga, R. Lovas, R. Liotta, Phys. Rev. Lett. **99**, 37 (1992).

[4] B. A. Brown, Phys. Rev. C **46**, 811 (1992).

[5] G. Royer, R. Gherghescu, Nucl. Phys. A **699**, 479 (2002).

[6] D. N. Poenaru, R. A. Gherghescu, W. Greiner, Phys. Rev. Lett. **107**, 062503 (2011).

[7] C. Qi, R. Liotta, R. Wyss, Prog. Part. Nucl. Phys. **105**, 214251 (2019).

[8] R. G. Lovas, R. J. Liotta, A. Insolia, K. Varga and D. S. Delion, Physics Reports **294**, 265-362 (1998).

[9] N. Ashok and A. Joseph, Nucl. Phys. A **977**, 101 (2018).

[10] V. Yu. Denisov and A. A. Khudenko, Phys. Rev. C **80**, 034603 (2009).

[11] D. Ni and Z. Ren, Phys. Rev. C **81**, 024315 (2010).

[12] D. S. Delion, Z. Ren, A. Dumitrescu and D. Ni, J. Phys. G **45**, 053001 (2018).

[13] S. Kumar and R. K. Gupta Phys. Rev. C **55**, 218 (1997).

[14] K. P. Santhosh and S. Sahadevan, Nucl. Phys. A **847**, 42 (2010).

[15] R. Kumar and M. K. Sharma, Phys. Rev. C **85**, 054612 (2012).

[16] J. Blocki, J. Randrup, W. J. Swiatecki, and C. F. Tsang, Ann. Phys. (NY) **105**, 427 (1977).

[17] P. Moller and J. R. Nix, Nucl. Phys. A **361**, 117 (1981).

[18] W. Reisdorf, J. Phys. G: Nucl. Part. Phys. **20**, 1297 (1994).

[19] W. D. Myers and W. J. Swiatecki, Phys. Rev. C **62**, 044610 (2000).

[20] W. D. Myers and W. J. Swiatecki, Ann. Phys. **55**, 395 (1969); Nucl. Phys. A **336**, 267 (1980).

[21] H. Ngô and C. Ngô, Nucl. Phys. A **348**, 140 (1980).

[22] G. Sawhney, M. K. Sharma and R. K. Gupta, Phys. Rev. C **83**, 064610 (2011).

[23] K. Sharma, G. Sawhney and M. K. Sharma, Phys. Rev. C **96**, 054307 (2017).

[24] Niyti, G. Sawhney, M. K. Sharma and R. K. Gupta, Phys. Rev. C **91**, 054606 (2015).

[25] R. K. Gupta *et al*, Int. Rev. Phys. (IREPHY) **2**, 369 (2008).

[26] R. K. Gupta in *Clusters in Nuclei* Lecture Notes in Physics edited by C. Beck, Vol. I (Springer-Verlag, Berlin), **818**, p.223 (2010).

[27] R. K. Gupta, in Proceedings of the 5th International Conference on Nuclear ReactionMechanisms, Varenna, edited by E. Gadioli (Ricerca Scientifica ed Educazione Permanente, Milano, 1988) p. 416.

[28] S. S. Malik and R. K. Gupta Phys. Rev. C **39**, 1992 (1989).

[29] S. K. Arun, R. K. Gupta, S. Kanwar, B. B. Singh and M. K. Sharma, Phys. Rev. C **80**, 034317 (2009).

[30] K. Sharma and M. K. Sharma, Nucl. Phys. A **986**, 1 (2019).

[31] R. K. Gupta, M. Balasubramaniam, R. Kumar, D. Singh and C. Beck, Nucl. Phys. A **738**, 479c (2004).

[32] L. Capponi et al., Phys. Rev. C **94**, 024314 (2016).

[33] G. Sawhney, K. Sandhu, M. K. Sharma and R. K. Gupta, Eur. Phys. J. A **50**, 175 (2014).

[34] I. Dutt and R. K. Puri, Phys. Rev. C **81**, 064609 (2010).

[35] S. Kumar, D. Bir and R. K. Gupta, Phys. Rev. C **51**, 4 (1995).

[36] J. K. Tuli, Nuclear Wallet Cards (2011), http://www.nndc.bnl.gov/wallet/.

[37] C. Qi, F. R. Xu, R. J. Liotta and R. Wyss, Phys. Rev. Lett. **103**, 072501 (2009).

Chapter 4

Cluster emission in view of Sn-Radioactivity

In the previous chapter, study on α-decay of trans-Sn nuclei was carried out within the PCM framework in view of radioactive emissions and the induced decay chains. The role of deformations and related orientations was investigated in order to identify the most preferred pairs in the decay channel. In addition to this, an extensive analysis of various nuclear proximity interaction potentials was carried out so as to shortlist the appropriate proximity interaction to study α-radioactivity in this intermediate mass region of the periodic table. As an extension of this, the cluster radioactivity having the emitting fragment heavier than α-particle is explored in the same mass region i.e. for trans-Sn nuclei. This study is worked out as an extension of previous work on Sn-radioactivity within PCM which considered only spherical fragmentation of neutron deficient and neutron-rich Xe-Gd parents. However, the effect of deformations and orientations, along with the importance of different proximity interactions is investigated in the present work. The works on ^{100}Sn (in case of neutron-deficient parents) and ^{132}Sn (for neutron-rich parents) radioactivity, with the deformation and orientation effects included in PCM, is published in [1]. This chapter presents a brief introduction to the exotic phenomenon of cluster radioactivity in Sec. 4.1. Further, the explanation to the results obtained is discussed in

Sec. 4.2 and the conclusions drawn from this study are summarized in Sec. 4.3 of the present chapter.

4.1 Introduction

The novel process of cluster radioactivity, i.e., the ground state emission of fragments heavier than ^{4}He, was firstly established on theoretical front [2] followed by its confirmation experimentally in 1984 [3]. Various clusters of C, N, O, F, Ne, Mg, and Si have been detected from a number of actinides ranging from ^{221}Fr to ^{242}Cm and the quest for other possible cluster emissions is still on. It is observed that in this rare, fourth-kind of radioactivity, closed shell nuclei are involved most of the times, i.e., the daughter is generally a closed shell, ^{208}Pb nucleus or its neighboring nucleus. To date, ^{34}Si is the heaviest cluster detected having longest decay half-life measured ($log_{10}T_{1/2} = 29.04$) from ^{238}U parent. In the framework of collective clusterization process, cluster radioactivity is similar to α-decay, where cluster is assumed to be preformed inside the parent nucleus and keeps on assaulting the surface of the nucleus before penetrating through it. For many cases, it has been established that the cluster emission from odd parent nuclei is hindered [4] as compared to those from the neighboring even-even isotopes; thereby indicating that even mass nuclei are better cluster emitters than the odd mass ones. Moreover, the observed decays, where the parent and daughter nuclei have odd mass, are less in number. Therefore, one can also explore this phenomenon in terms of odd-even effect besides the possible existence of new islands of cluster radioactivity.

Stressing on the importance of shell effects in the trans-lead region, another fertile region for the possible existence of cluster radioactivity was predicted to be the trans-tin domain [5,6], where the role of closed shell daughter such as ^{100}Sn or ^{132}Sn and its adjacent neighbors may reinforce the possibility of cluster emission. It is worth mentioning that 'Tin' represents the shell closure at $Z = 50$, just before the lead $Z = 82$, and hence in order to explore this region, ground state (T=0) decays of neutron-deficient $^{108-116}$Xe, $^{112-120}$Ba,

$^{116-124}$Ce, $^{120-124}$Nd, $^{124-128}$Sm and $^{128-132}$Gd nuclei had been analyzed in [5] on the basis of Preformed Cluster Model (PCM) [7–11]. This study indicates the interesting possibility of ^{8}Be decay of ^{108}Xe, ^{12}C decay of ^{112}Ba, ^{16}O decay of ^{116}Ce, etc., thereby showing a clear choice for A=4n α-like clusters invoking the doubly magic ^{100}Sn (Z=N=50) daughter. Apart from this, another study [6] was also carried out for some of the neutron rich ^{146}Ba, ^{152}Ce, ^{156}Nd, ^{160}Sm and ^{164}Gd parents to address the phenomenon of ^{132}Sn (N=82, Z=50) daughter radioactivity. It was observed [5, 6] that, with an increase in N/Z ratio of the parent nuclei, the contribution of A$\neq$4n non-α nuclei clusters becomes prominent. Experimentally, some attempts [12] were done to observe the ^{100}Sn-daughter radioactivity from ^{114}Ba parent nucleus formed in ^{58}Ni+^{58}Ni reaction. In addition, various models predicted Ba isotopes as the potential candidates for radiocarbon (cluster) decay [13–16], but all such attempts ended with only the upper limits of their half-life times. Instead, a new phenomenon of intermediate mass fragments (IMFs), also referred to as 'clusters' or 'complex fragments', emitted from the excited compound nucleus, was observed.

Considering strong shell effects in possible cluster emissions, the deformations and orientations of nuclei are also expected to play an important role. In order to examine such effects, we have chosen to work on both the neutron-rich and neutron-deficient nuclei, using the same, QMFT [17–20] based PCM methodology to study the impact of nuclear deformations and orientations on structural profile and hence the potential energy surfaces (PES) of $^{108-116}$Xe, $^{112-120,146}$Ba, $^{116-124,152}$Ce,$^{120-130,156}$Nd, $^{124-130,160,162}$Sm and $^{128-136,166}$Gd parents. Based on the collective clusterization picture, PCM is built with the use of preformation and penetration probabilities, which in turn help in evaluating the decay half-lives of the emitted clusters. Interestingly, all the parent nuclei considered here are prolate deformed. The emitted clusters ^{6}Li, ^{8}Be, ^{10}B, ^{14}N are oblate deformed whereas ^{16}O, ^{18}F, ^{20}Ne, ^{24}Mg and ^{28}Mg are prolate deformed, thereby signifying the indispensable role of deformations, not probed in the earlier works [5, 6]. The distinct advantage of including deformation effects in the fragmentation analysis is that, these effects influence the interaction potential, which in turn provide the corresponding modifications in the

barrier height and barrier position. The influence of deformation effects has been considered in other works [21,22] within PCM for the exotic decays of ground state parent nuclei from the trans-Pb region. The deformation effects up to quadrupole (β_2) alongwith the choice of "optimum" orientations [23] were found sufficient to address the experimental data on half-life times via the only parameter, viz. the neck-length parameter ΔR. Later on, the effect of higher-multipole deformations (β_{3i}, β_{4i}; i = 1, 2) was also accounted [24] in the emission of ^{14}C clusters with use of "compact" orientations.

Motivated by the above mentioned studies [21, 22, 24], using the preformed cluster model (PCM), here, the effects of nuclear deformations are investigated by incorporating the quadrupole and the higher order deformations, such as the octupole and hexadecapole, on the fragmentation behavior of the various ground state parent nuclei in trans-Sn region. Importantly, note that the experimentally observed β_3 values are not available in literature, thus the use of higher order deformations [25] must be made accurately, especially for the studied $8 \leq A \leq 34$ cluster emissions. In addition, the comparative analysis of nuclear proximity interaction potentials (Prox 1977, Prox 1988, and Prox 2000) having different isospin and asymmetry dependent parameters is made in terms of most probable cluster configuration emitted across ^{100}Sn-daughter nuclei. Furthermore, to explore the structural aspects in the dynamics of Sn radioactivity, the possible role of shell corrections has been worked out in terms of fragmentation potential and the preformation factor. An early report [26] on tin-radioactivity work was presented at the 12^{th} International Conference on Nucleus-Nucleus Collisions (NN2015) held in Catania, Italy.

Section 4.2 gives the details of our calculations and conclusions drawn for the radioactive cluster decay of the selected parent nuclei. Finally, the results are summarized in Sec. 4.3.

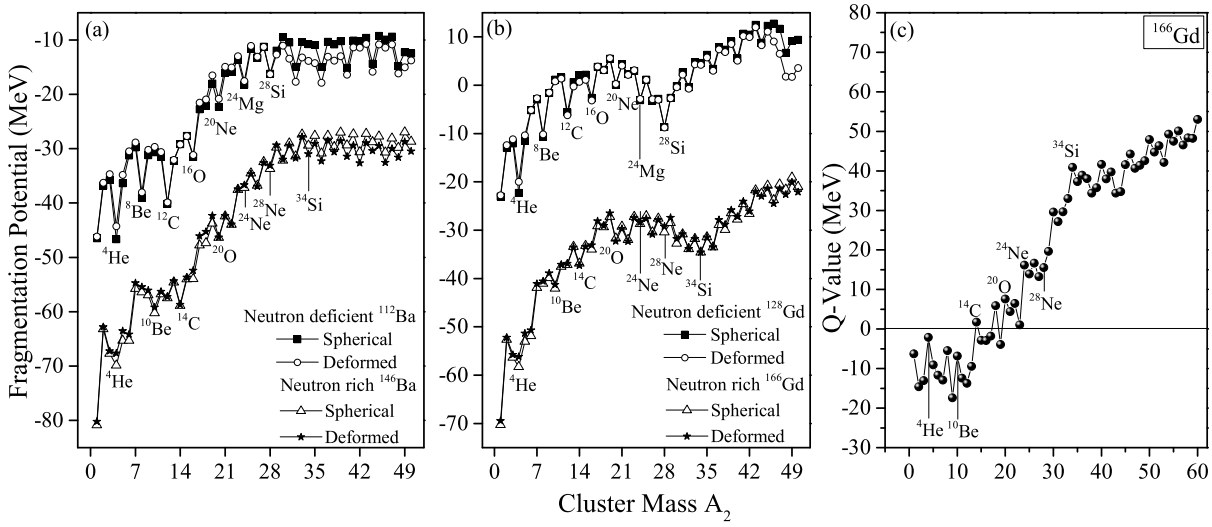

Figure 4.1 PCM calculated mass fragmentation potentials for the decay of (a) ^{112}Ba and ^{146}Ba parents and (b) ^{128}Gd and ^{166}Gd choices of parents considering spherical as well as deformed choice of nuclei. The relative distance is chosen as $R_t = R_1 + R_2$ in these calculations. The variation of Q-value with this cluster mass is depicted in panel (c) for parent nucleus ^{166}Gd.

4.2 Calculations and Results

Following the earlier study [21, 22] in the region of parent nuclides with $Z > 82$, the importance of deformations and orientations over the domain of nuclides lighter than Pb with atomic number $Z > 50$ is examined in order to investigate the importance of doubly magic ^{100}Sn or ^{132}Sn daughter from the point of view of exotic cluster decays. Ranging from the neutron-deficient to neutron-rich parents, the calculations for $^{108-116}$Xe, $^{112-120,146}$Ba, $^{116-124,152}$Ce,$^{120-130,156}$Nd, $^{124-130,160,162}$Sm and $^{128-136,166}$Gd nuclei have been performed. The possible cluster emission from the above mentioned region has been explored, which in general decay via doubly closed shell ^{100}Sn or ^{132}Sn daughter nuclei and/or nearby spherical/ deformed daughters. In other words, a comprehensive study has been carried out for spherical and deformed approaches of fragments to explore the properties of ground state parent nuclei in trans-Sn region. The characteristics such as potential energy surfaces, preformation probability, penetrability, decay barrier height etc. are studied with an aim to emphasize that the considered deformed parents in

the neighborhood of Z=50 are unstable against several cluster emission channels. Note that the spherical consideration of the fragments is allowed only via the Coulomb and nuclear interaction potentials since the binding energies therein are taken from either the experiments [27] or that from the deformation based calculations of Möller *et al.* [25].

The present calculations are performed at touching configuration i.e. $R_a = R_t = R_1 + R_2$ and angular momentum effects are kept silent. For deformations upto β_2, the orientation degree of freedom is fixed by using "optimum" orientation $\theta_i^{opt.}$ of Ref. [23] which manifest in the form of "hot compact" or "cold elongated" configurations. However, for investigating the role of higher order deformations, "compact" orientation should be used, instead. As the cluster emission process is a 'cold' phenomenon, we find here a clear preference for "cold elongated" configuration. Note that the interaction potential works as main ingredient for a 1-D barrier penetration model like the PCM, so a minute variation in its value may alter the decay constants and half-lives significantly. Therefore, it will be interesting to observe how the use of different interaction potentials, Prox77, Prox88 and Prox00 affect the potential energy surfaces (PES) of the considered neutron deficient parent systems. The nuclear proximity potential of Blocki *et al.* [28] has been employed in the earlier works of Gupta *et al.* [5] to investigate cluster radioactivity phenomenon. In addition to the previously studied parent systems in [5,6], we have extended the work to analyze/investigate ^{8}Be, ^{12}C, ^{16}O, ^{20}Ne, ^{24}Mg and ^{28}Si emissions from various $^{108-116}$Xe, $^{112-120,146}$Ba, $^{116-124,152}$Ce $^{120-130,156}$Nd, $^{124-130,160,162}$Sm and $^{128-136,166}$Gd parents for the comprehensive knowledge of cluster dynamics with and without inclusion of deformation effects.

First, the importance of deformations and orientations in view of mass fragmentation potentials V_η is investigated and depicted in Fig. 4.1(a) for ^{112}Ba and ^{146}Ba nuclei which correspond to neutron deficient and neutron rich isotopes of Ba nucleus. Similarly, fragmentation potential for ^{128}Gd (neutron deficient) and ^{166}Gd (neutron rich) nuclei are plotted in Fig. 4.1(b). Only the clusters for mass $A_2 \leq 50$ are considered. Here, the interesting clusters are the ones present in the potential energy minima because the

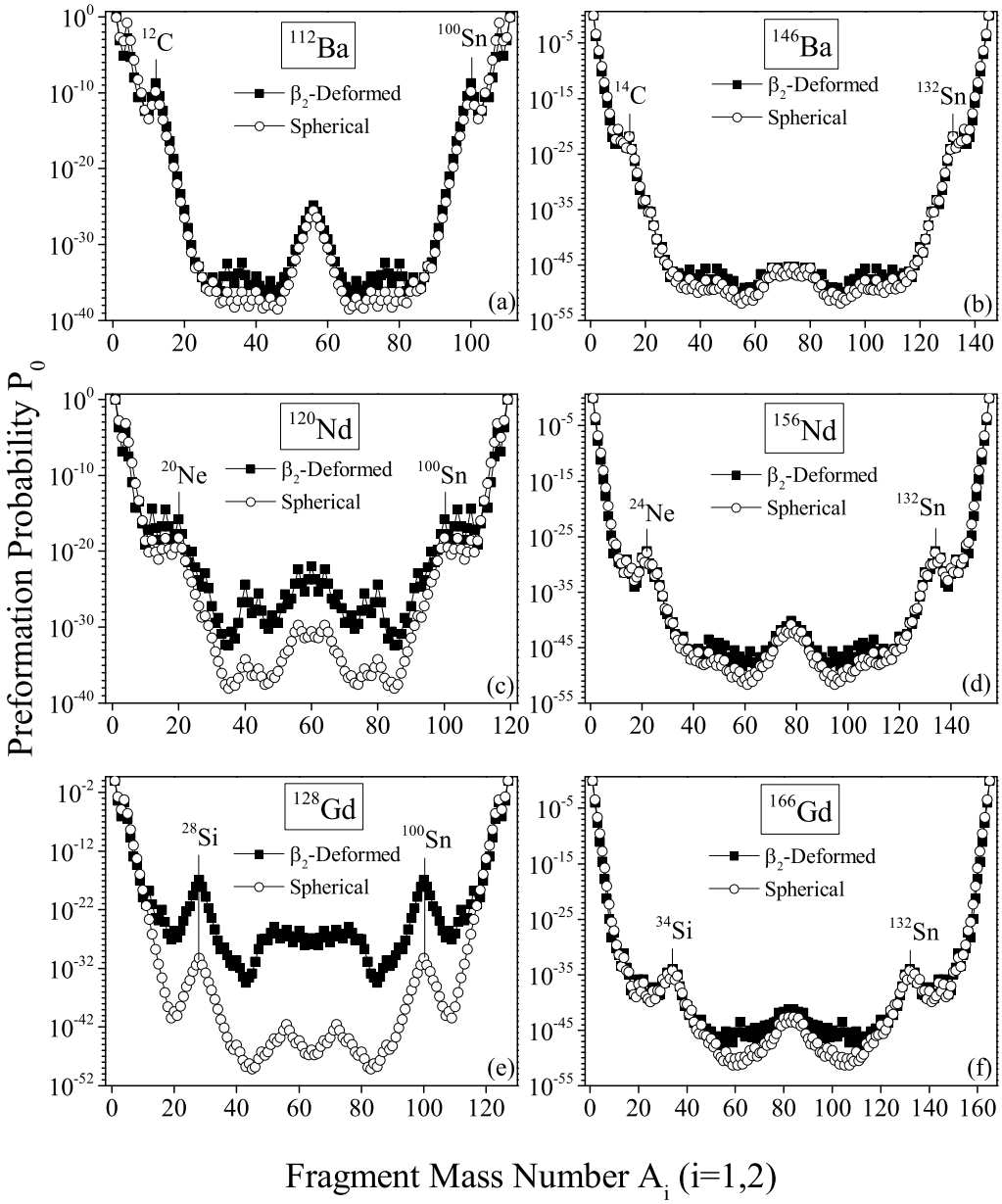

Figure 4.2 Fragment preformation probability P_0 plotted as a function of fragment mass A_i showing the comparison of spherical and deformed choice of fragmentation for the parent nuclei (a) ^{112}Ba (b) ^{146}Ba (c) ^{120}Nd (d) ^{156}Nd (e) ^{128}Gd and (f) ^{166}Gd.

preformation factors (P_0) become prominent for the clusters at the minima of fragmentation potential. Basically, the minima in PES emerges predominantly because of the (spherical or deformed) shell closure effects of one or both the fragments which in turn provides insight regarding understanding of nuclear structure effects. It is noted that for the N=Z ^{112}Ba and ^{128}Gd parents, the minima in V(A_2) is seen at A_2=4n α-nuclei. With the increase in N/Z ratio, the minima start emerging at A_2=4n+2 clusters. The preference of non-α-like clusters decaying from neutron-rich parent systems and α-like clusters from neutron-deficient nuclei indicates the significance of asymmetry/symmetry of proton-neutron in both cases. It may be noted that non α-like clusters, $A_2 \neq 4n$ i.e. ^{14}C, ^{20}O, ^{24}Ne, ^{28}Mg and ^{34}Si were observed [4,5] in decay of various parents with Pb or neighboring nuclei as the daughter system. Interestingly, the nuclei ^{146}Ba, ^{166}Gd seem to be stable ($Q < 0$) against α-decay and unstable against several cluster decays. Even the predicted half-life times for considered exotic decays come out to be smaller than that for α-decay. In other words, the Q-value systematics for neutron rich parents enforces the appearance of non-α-like fragments in the cluster radioactivity process. Fig. 4.1(c) presents the calculated Q-values which is the available energy for the clusters to penetrate the potential barrier. Though the lighter clusters like ^{10}Be, ^{14}C, ^{20}O, etc. show minima in potential energy, their Q-values are very low. The higher Q-value increases the tunnelling probability which increases the probable existence of a particular decay mode. For example, penetrability for ^{34}Si cluster in the decay of ^{166}Gd comes out to be very large (refer to Fig. 4.4(b), discussed later). The Q-value systematics prefers the emission of ^{14}C, ^{20}O, ^{24}Ne, ^{28}Ne clusters in the decay of ^{166}Gd parent nucleus.

The above results can be more vividly interpreted in context of the quantity called as preformation probability (P_0) plotted in Figs. 4.2(a) to 4.2(f) for ^{112,146}Ba, ^{120,156}Nd and ^{128,166}Gd parents with respect to fragment mass for both spherical and deformed choices of fragmentation. A black vertical line is drawn in all panels of Fig. 4.2 to point out the most probable and hence energetically favored fragment. Here P_0, being a relative quantity, its magnitude is dependent on the relative contribution of all the decaying fragments in the

collective clusterization process and not on the cluster and daughter fragment alone. Here, four interesting results are obtained from Fig. 4.2: (i) the preferred cluster shifts towards the heavy mass region on increasing the mass number of parent nucleus. (ii) the status of favorably preformed fragments remains intact irrespective of the inclusion of deformation effects. Note that other clusters with potential equivalent to that of most probable cluster (shown in Fig. 4.1) are ruled out possibly due to small barrier penetrability P. (iii) closed shell effects of doubly magic ^{100}Sn on ^{12}C, ^{20}Ne and ^{28}Si and similarly ^{132}Sn on ^{14}C, ^{24}Ne and ^{34}Si fragments are clearly evident in terms of strong maxima appearing across heavier fragments in Fig. 4.2. (iv) while comparing spherical and deformed approaches, a huge difference is seen in the preformation values for decay of ^{128}Gd possibly because of the difference in its fragmentation potential in the fission region as clearly depicted in Fig. 4.1(b).

The above results hold true for all the studied neutron deficient to neutron rich Xe-Gd parents, thereby providing the relevant information regarding the structural behavior of these exotic nuclei. Note that, here doubly magic ^{100}Sn and ^{132}Sn correspond to the magic shell closure at neutron magic N=50, proton magic Z=50 and at N=82, Z=50, respectively. Moreover, it can be stated that the calculated mass distributions are found to be symmetric for almost all the 6 cases shown in Fig. 4.2, exhibiting the structure having hump in the cluster mass region.

Noting that the decay constant λ (or half-life times $T_{1/2}$) in PCM reflects the combined effect of both the preformation probability P_0 and the penetrability P (since the assault frequency ν_0, being merely a constant, varies in between 10^{20} to 10^{22} s^{-1}). The result of these two quantities along with the calculated $\log_{10}T_{1/2}$ values is depicted in Fig. 4.3 for the exotic decay of neutron deficient $^{108-116}$Xe, $^{112-120}$Ba, $^{116-124}$Ce,$^{120-130}$Nd, $^{124-130}$Sm and $^{128-136}$Gd parent systems covering almost all the known nuclei emitting various clusters from ^{8}Be to ^{28}Si. The choice of these clusters is made purely on the basis of potential energy minima in fragmentation path and hence maxima in preformation profile, discussed respectively in Figs. 4.1 and 4.2.

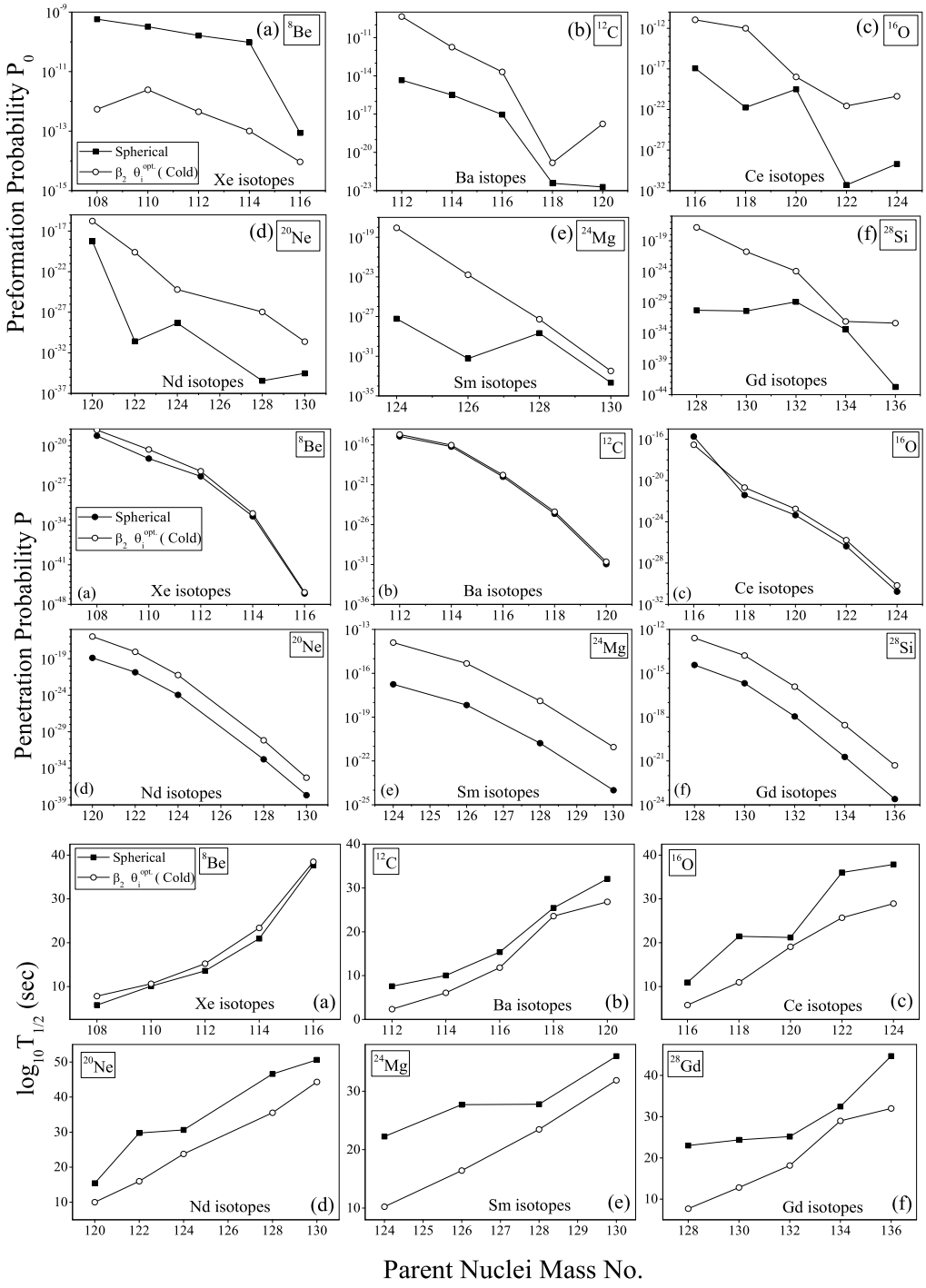

Figure 4.3 Preformation probability P_0, penetrability P and $\log_{10}\mathrm{T}_{1/2}$ as a function of parent nuclei mass number for the possible clusters emitted from different isotopes of Xe to Gd parents: (a) ^{8}Be emitting from Xe isotopes (b) ^{12}C from Ba isotopes (c) ^{16}O from Ce isotopes (d) ^{20}Ne from Nd isotopes (e) ^{24}Mg from Sm isotopes (f) ^{28}Si from Gd isotopes, showing comparison between spherical and deformed approach using cold configuration of emitted fragments.

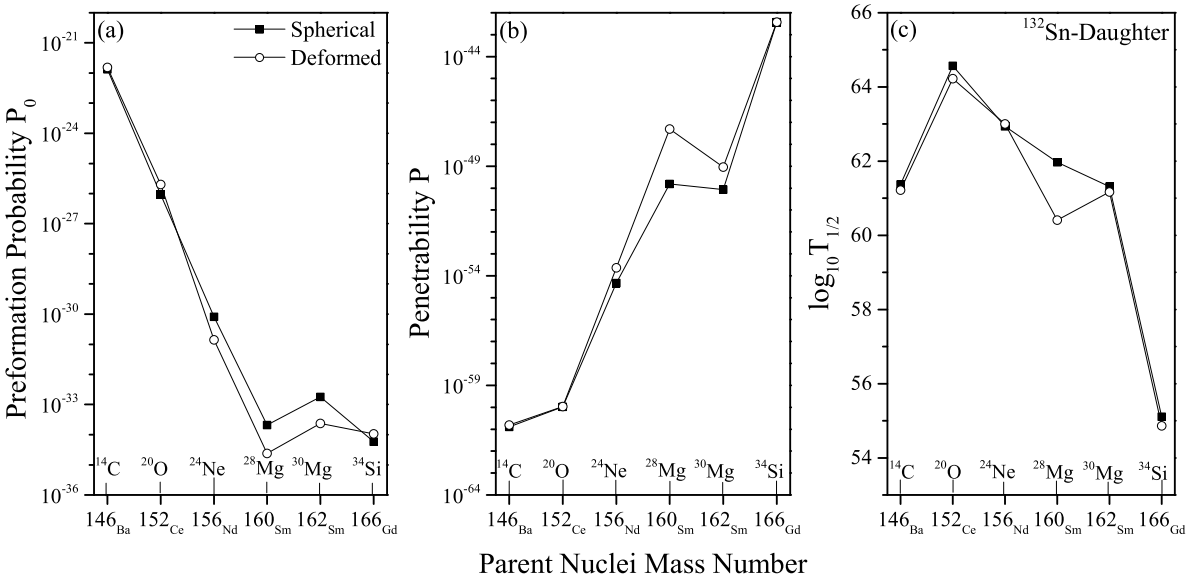

Figure 4.4 (a) Preformation probability (b) penetrability and (c) logarithm of half life $\log_{10}T_{1/2}$ plotted against neutron-rich parent nuclei mass number for both spherical and deformed approach of fragmentation. Note that all parent nuclei emit ^{132}Sn as daughter product.

For majority of the nuclei studied, it is observed that P_0 and P increase while one moves from spherical to deformed shape, thereby indicating indispensable role of deformation effects. Such a systematics is not followed by Xe isotopes, shown in panel (a) possibly because of the fact that some neck value is required to exercise the penetration process. In Fig. 4.3, it is seen that P_0 decreases in magnitude for spherical case (solid squares); whereas the same appears to be significantly large for deformed configuration (open squares). The same is true for penetrability which is comparatively higher for the deformed case. Furthermore, the evaluated half-lives for various cluster emissions clearly show that ^{8}Be emission from ^{108}Xe, ^{12}C from ^{112}Ba, ^{16}O from ^{116}Ce, etc. have the lowest $T_{1/2}$ values compared to the decay from neighboring ones. This is because of the fact that the clusters emitted correspond to doubly magic ^{100}Sn daughter nucleus. As expected, the magnitude of $\log_{10}T_{1/2}$ value is observed to be least for deformed configuration, varying over a wide range $\sim$ 3 to 40. In other words, the decays leading to doubly magic ^{100}Sn daughter are speculated as the probable cases for future measurements. The present study is an extension of the earlier report [26] to include cluster decays of parent nuclei having

daughter fragments other than doubly closed shell ^{100}Sn as well.

Similar outcomes are observed for the considered neutron rich isotopes of Ba to Gd parents. Apparently, the behavior of P_0, P and $\log_{10}T_{1/2}$ presented in Fig. 4.4 is found to be similar for spherical and deformed cases, for the chosen ^{146}Ba, ^{152}Ce, ^{156}Nd, ^{160,162}Sm and ^{166}Gd parents, independent of their masses. The preferential decay channel leading to doubly magic ^{132}Sn daughter (Z=50, N=82) is selected due to the largest preformation factor for all nuclei investigated here. Focussing on the importance of deformations, it is clearly seen from the comparison of Fig. 4.3 and Fig. 4.4 that P_0 and P for the β_2 deformed case are larger and hence half-life times are smaller for the same; thereby indicating interesting case of investigation. Hence, the inclusion of β_{2i} deformation influences significantly the emission of exotic clusters in the intermediate mass region. Furthermore, amongst the chosen isotopes of Ba, cluster half life is found to be smallest for the lightest isotope and observed to increase with the increasing number of neutrons in the mother nucleus. In other words, the emission of carbon (C) isotopes from ^{146}Ba has $T_{1/2}$ values larger than that of ^{112}Ba. Similar result holds good for oxygen (O) emission from Ce isotopes, Ne emission from Nd isotopes, Mg from Sm isotopes and Si from Gd isotopes. Summarizing, it is observed that the neutron-proton asymmetry in parent as well as daughter nuclei is responsible for the reduction in decay rate (and hence larger half life). From the above discussion, one may conclude that the decays leading to ^{100}Sn daughter seem to be more probable as compared to ^{132}Sn daughter ones while exploring cluster radioactivity in trans-Sn region.

Now, to understand the role of doubly magic closed shells more precisely, the minimized fragmentation potential V_η(R) is plotted for isobars of A=120, 124 and 128 in Fig. 4.5. The calculations are performed for the clusters ^{12}C, ^{16}O, ^{20}Ne, ^{24}Mg and ^{28}Si decaying respectively from (a) ^{120}Ba, ^{120}Ce, ^{120}Nd (b) ^{124}Ce, ^{124}Nd, ^{124}Sm and (c) ^{128}Nd, ^{128}Sm, ^{128}Gd parents. As mentioned above, the cluster corresponding to the Sn daughter (Z_2=50) seems to be energetically most preferred. As an instance, one can notice in panel (a) that in case of ^{120}Ba, the cluster ^{12}C is having the lowest fragmentation potential and hence

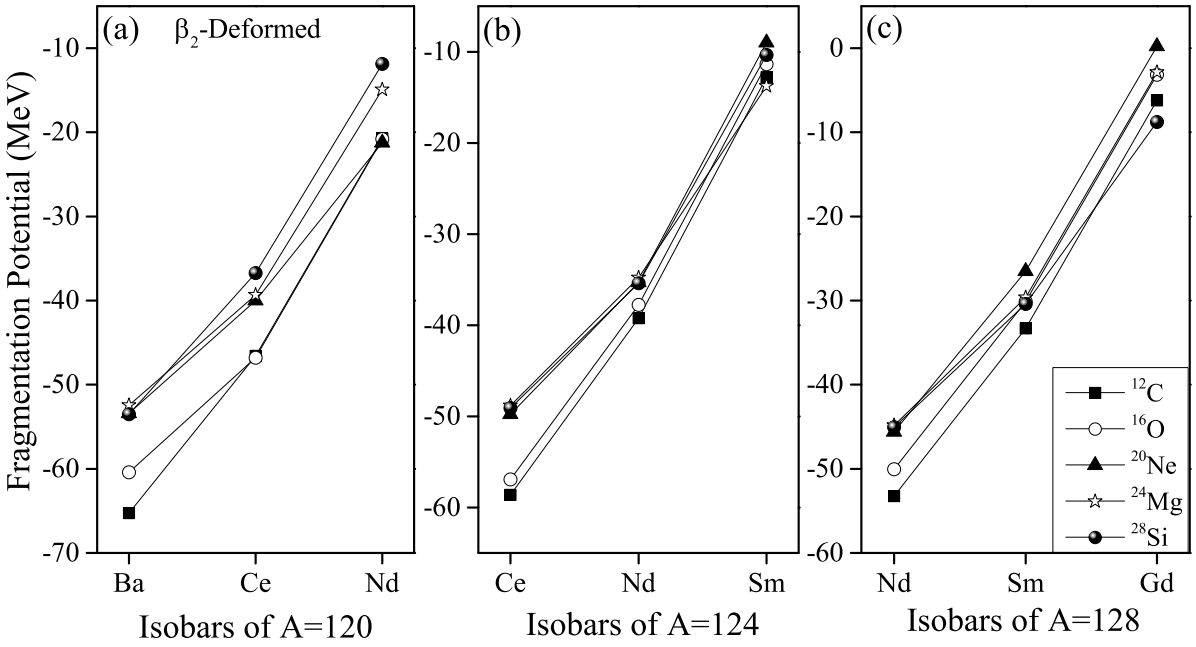

Figure 4.5 Variation of fragmentation potential (V_η) with isobars of A=120, 124 and 128 showing the comparison between clusters ^{12}C, ^{16}O, ^{20}Ne, ^{24}Mg and ^{28}Si emitted from (a) ^{120}Ba,^{120}Ce,^{120}Nd (b) ^{124}Ce,^{124}Nd,^{124}Sm and (c) ^{128}Nd,^{128}Sm,^{128}Gd parent nuclei.

one finds highest preformation yield for corresponding fragment as compared to the other emitted clusters. Similarly, in the decay of ^{120}Ce and ^{120}Nd nuclei, the minima in PES correspond to ^{16}O and ^{20}Ne clusters respectively in contrast to other emitting clusters. This observation is mainly attributed to magicity effect of heavy fragment ^{100}Sn having charge Z_2=50 and neutron number N_2=50. The similar outcomes are seen for isobars A=124 and A=128 respectively, depicted in panels (b) and (c) of Fig. 4.5. The above discussion implies that the nuclear shell structure effects play an essential role in reference to cluster emission in trans-Sn region.

Knowing that smaller Q-value corresponds to a larger half-life time, the same result is illustrated in present calculations presented in Fig. 4.6, where $\log_{10}T_{1/2}$ and Q-values for the ^{16}O cluster (emitted from various isotopes of Ce parent) are plotted with respect to Sn daughter neutron number. Apparently, the calculated half-lives show a sensitive dependence on Q-values estimated from available binding energies. Furthermore, the decay leading to ^{100}Sn appears as the most probable case of measurement ($T_{1/2} \sim 10^5$

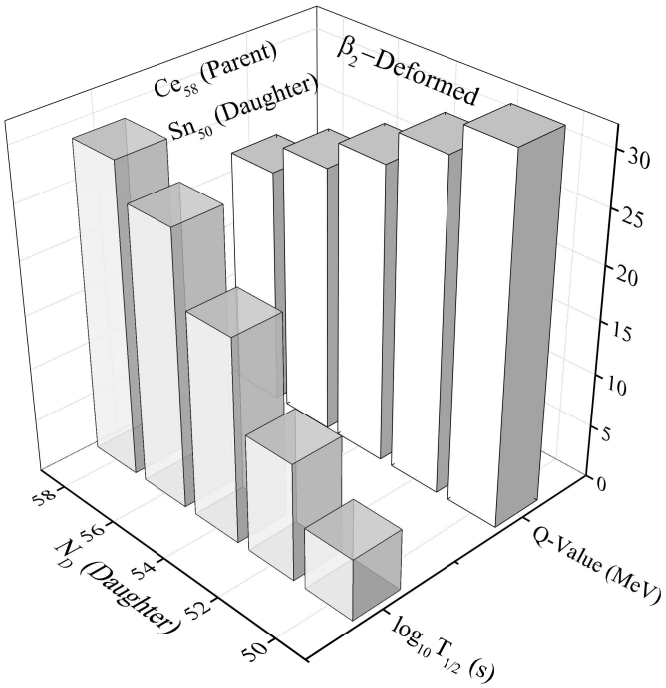

Figure 4.6 A 3-dimensional plot showing the variation of $\log_{10}T_{1/2}$ (s) and Q-value (MeV) as a function of neutron no. of daughter nucleus considering deformed fragments with optimum orientations. The cluster emitted (^{16}O) is kept fixed here.

sec). It is noted that with the decrease in the Q-value by about 0.5 MeV, an increase in the $T_{1/2}$ value by about one order is obtained. Therefore, the simultaneous measurement of the Q-value and $T_{1/2}$ is quite essential.

Further, the relevance of different nuclear potentials is investigated in Fig. 4.7, in terms of fragmentation potential to look for the relative emergence of probable cluster decays and associated nuclear structure effects, if any. In addition to the proximity potential used in all the calculations above i.e. Prox 1977 [28], the other potentials Prox 1988 [29,30] and Prox 2000 [31] having different dependencies on isospin and asymmetry parameter have been implemented here for the case of β_2-deformed choice of fragments. Although the magnitude of fragmentation potential are somewhat different for three potentials, their structural profiles are similar and exhibit α-like structure for fragments up to A_2=50. It is relevant to remind that Prox77 and Prox88 use the same universal function and its parameters, except the values of two co-efficients of surface energy term, whereas Prox00 uses an entirely different formulation.

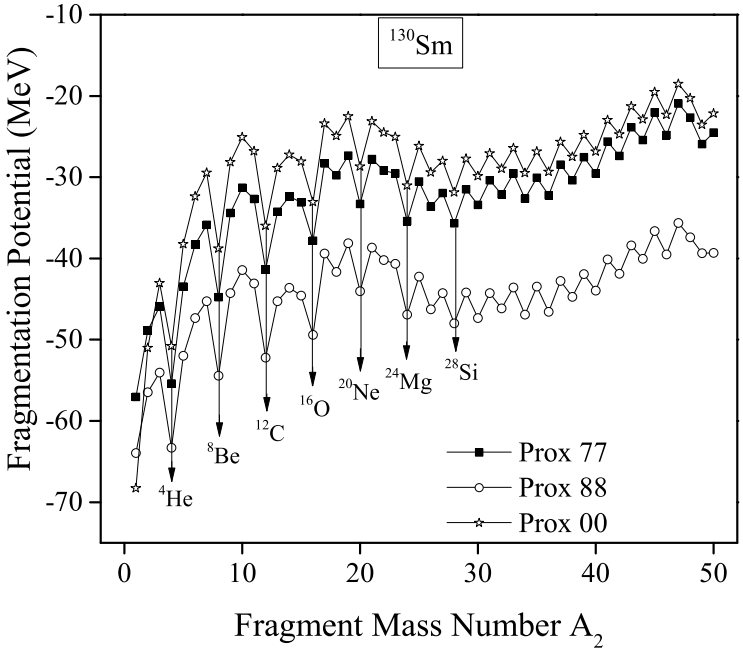

Figure 4.7 Fragmentation potential $V(\eta)$ for the decay of ^{130}Sm using nuclear proximity potentials Prox77, Prox88 and Prox00 at $R_a = R_t$ with deformed choice of fragmentation. The most probable clusters are pointed out with the solid lines.

Next, the possible role of shell corrections is analyzed here in Fig. 4.8 for the decay of ^{124}Sm nucleus. Firstly, the dependence of P_0 on shell corrections by considering δU=0 and then δU$\neq$0 is explored. It is clear from the figure that cluster ^{24}Mg (and its complementary heavy residue ^{100}Sn) appear in the preformation peak, only when the shell corrections δU are added to the liquid drop part of the binding energy. The above observation comprehensively suggests that shell corrections along with the choice of proximity potential play a crucial role in governing the clusterization process.

To probe the role of deformations and orientations further, fragmentation behavior is explored explicitly for ^{162}Sm case in Fig. 4.9(a) showing the comparison of quadrupole (β_2) deformed fragmentation with the higher order deformations up to hexadecapole (β_4). Importantly, deep minima are obtained for many clusters (due to their large values of deformation parameters) in case of deformations included upto β_{4i}, otherwise comparatively smooth potential surfaces are observed for both the spherical and β_{2i}-deformed choices. Similarly, while concentrating on the scattering path obtained via normalization of the

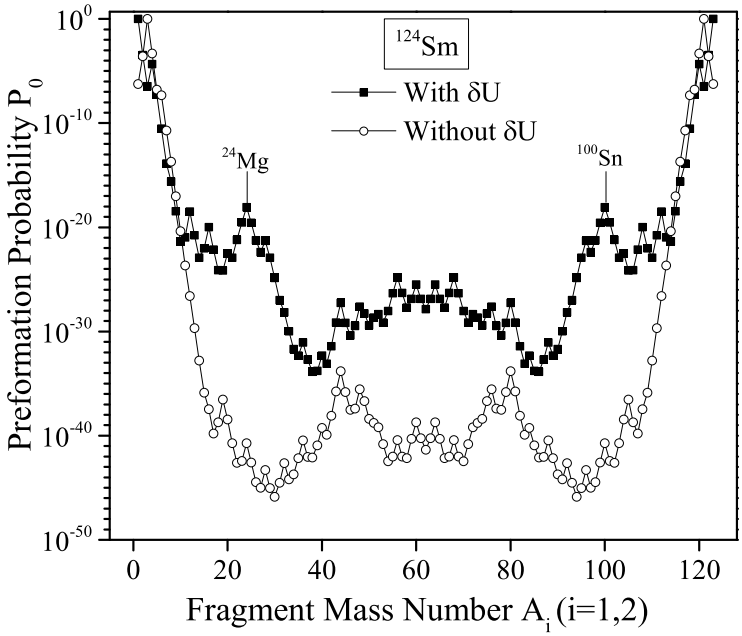

Figure 4.8 Role of shell corrections δU, depicted for ^{124}Sm by plotting the preformation factor P_0 with respect to both the cluster and daughter masses, showing the emergence of ^{100}Sn as the daughter product.

fragmentation potential w.r.t. binding energy, Fig. 4.9(b) shows that at the touching configuration ($R_a = R_t$), the barrier characteristics in terms of position as well as height get modified with the inclusion of higher order deformation and orientation effects of the decaying fragments. As expected, due to deformations, the barrier heights get reduced and position increased, thereby affecting the tunnelling probability P and hence the cluster decay half-life times. Since the calculated half life in PCM depends explicitly on both P_0 and P, this implies that the choice of deformations and orientations plays a vital role to estimate the half-life times and hence the cluster emission of considered nuclei.

Furthermore, an effort is made to estimate the cluster half lives using various neck length parameters to estimate the corresponding $\log_{10}T_{1/2}$ values for possible cluster emission in the trans-Sn region. Table 4.1 shows the cluster $\log_{10}T_{1/2}$ values for the use of different necks i.e. ΔR=0.0, 0.25 and 0.5 fm, for the decay of N=Z ^{112}Ba, ^{116}Ce, ^{120}Nd, ^{124}Sm and ^{128}Gd parent nuclei within deformed choice of fragmentation.

It is clear from Table 4.1 that the clusters ^{12}C, ^{16}O, ^{20}Ne, ^{24}Mg and ^{28}Si emitting

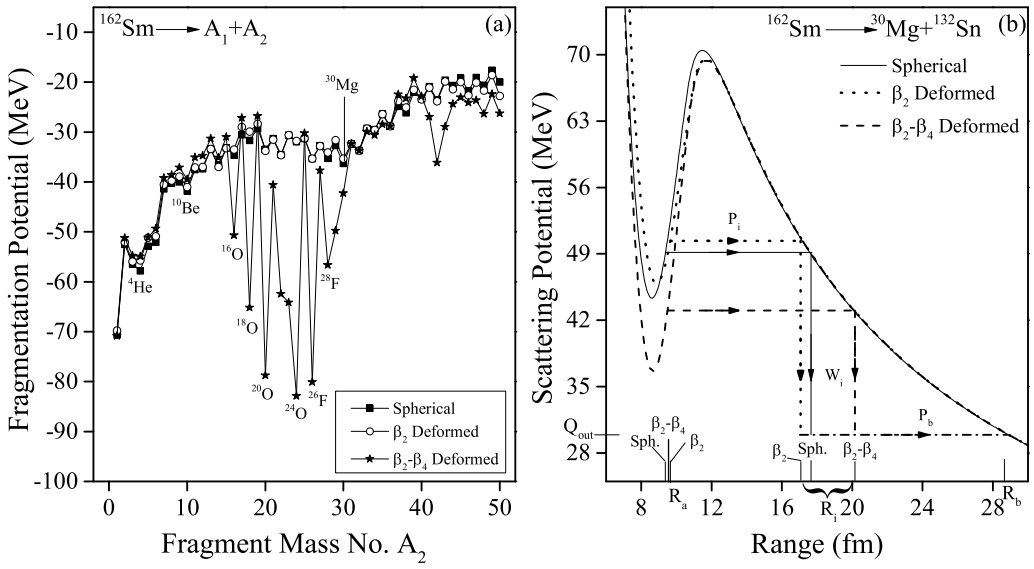

Figure 4.9 (a) The fragmentation potential for ^{162}Sm parent nucleus, taking the two fragments as spheres, β_{2i} alone, and $(\beta_{2i} - \beta_{4i})$ deformations at $R_a = R_t$. (b) Scattering potential for ^{30}Mg (+^{132}Sn) decay of parent nucleus ^{162}Sm, with spherical, β_2-deformed and multipole deformations approach included upto hexadecapole and orientation angles θ_i^c of compact cold configurations.

Table 4.1 The cluster $\log_{10}T_{1/2}$ values using different neck lengths parameters i.e. ΔR=0.0, 0.25 and 0.5 fm for the decay of N=Z ^{112}Ba, ^{116}Ce, ^{120}Nd, ^{124}Sm and ^{128}Gd parent nuclei while considering the deformed choice of fragmentation.

Parent	Decay	$\log_{10}T_{1/2}$		
Nucleus	Channel	R_t	R_t+0.25	R_t+0.5
^{112}Ba	^{12}C+^{100}Sn	3.35	2.98	2.35
^{116}Ce	^{16}O+^{100}Sn	5.77	5.22	3.23
^{120}Nd	^{20}Ne+^{100}Sn	10.02	8.68	7.53
^{124}Sm	^{24}Mg+^{100}Sn	10.24	8.60	7.21
^{128}Gd	^{28}Si+^{100}Sn	7.70	4.91	2.73

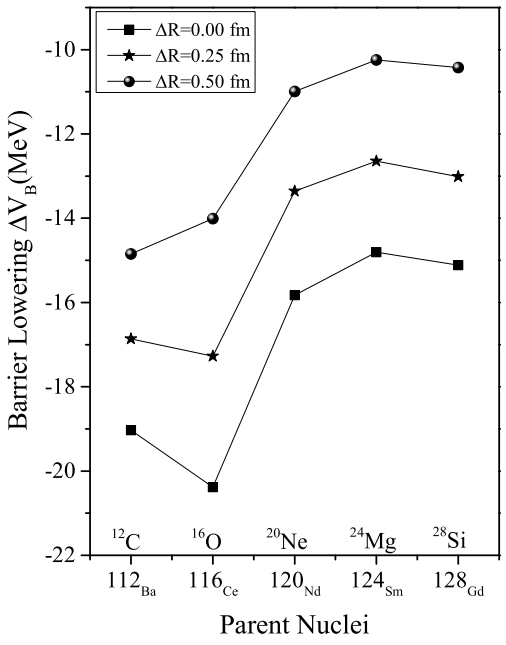

Figure 4.10 Variation of barrier lowering parameter ΔV_B (MeV) with the different neutron deficient N=Z parent nuclei on the x-axis for various values of neck length parameter ΔR considering deformed choice of fragments.

from their respective N=Z parents ^{112}Ba, ^{116}Ce, ^{120}Nd, ^{124}Sm and ^{128}Si have logarithms of half-lives in the range $\sim$ 2 to 10 which may provide useful information for the future experiments on cluster radioactivity of various nuclides in trans-Sn domain. Furthermore, the barrier modification ΔV_B, which is an intrinsic characteristic of PCM, is also estimated in reference to different choices of neck values. The variation of ΔV_B is plotted in Fig. 4.10 for neutron deficient parent nuclei while considering the deformed approach of fragmentation. It is worth mentioning here that ΔV_B is largely influenced by the variation in ΔR. The touching configuration i.e. R_a=R_1+R_2 corresponds to the largest barrier modification, however, the same is found to decline in magnitude while increasing the neck length parameter. It is clear from Fig. 4.10 that heavier fragments demand relatively less barrier modification. It is evident from the above discussion that the neck values and consequently the barrier lowering parameter play important role in deciding the tunnelling path and hence the half-life time of the respective clusters.

4.3 Summary

Summarizing, the effect of deformations and orientations is investigated in context of ground-state clusterization of $^{108-116}$Xe, $^{112-120,146}$Ba, $^{116-124,152}$Ce, $^{120-130,156}$Nd, $^{124-130,160,162}$Sm and $^{128-136,166}$Gd nuclei using the PCM. The deformations are used upto quadrupole (β_2) with optimum cold orientations as cluster radioactivity is a spontaneous decay process. The neutron-deficient parents have been shown to emit $\alpha-$like, A_2=4n clusters (for complementary daughter fragment ^{100}Sn), whereas the neutron-rich radioactive nuclei decay via emission of A_2=4n+2 clusters (non $\alpha-$like) independent of the choice of spherical/deformed fragmentation. The deformations and orientations seem important for the study of Sn-radioactivity because the fragmentation and scattering potentials get modified significantly after inclusion of such effects. While considering the deformed approach, it is found that cluster half life becomes much smaller than that for spherical approach. Hence, it is observed that the consideration of deformed choice seems to provide a favorable option for dealing with the decays leading to ^{100}Sn and ^{132}Sn daughter. In addition to this, it is also concluded that the decays forming ^{100}Sn as daughter product are more probable in view of cluster radioactivity phenomenon as compared to the decays leading to ^{132}Sn daughter fragment due to their higher P_0 and P values and corresponding lower half-lives.

The effect of different nuclear proximity interactions is also examined in reference to potential energy surfaces representing the nuclear structure effects. It is observed that Prox77, Prox88 and Prox00 exhibit similar clustering pattern in minima of fragmentation potential. Additionally, in order to obtain further description of the dynamics involved, the role of shell effects is examined via preformation profile and it is noticed that the shell effect (δU) is one of the essential factor that decides the structural behavior of cluster emission process. Besides the quadrupole (β_{2i}) deformations, an attempt is made to study the effect of higher-multipole deformations (upto hexadecapole i.e. β_{2i}, β_{3i}, β_{4i}) with cold compact orientations of nuclei in view of fragmentation path and barrier

characteristic behavior. The spherical and β_2-deformed approaches possess minima at 4n or 4n+2 clusters but large variation/fluctuations are seen in the potential energy surfaces while considering the deformations upto β_{4i}. This clearly indicates the significance of deformation effects in cluster emission of nuclei involved in Sn-radioactivity process.

After α-decay and cluster radioactivity, the next chapter presents the binary fragmentation via spontaneous fission of radioactive nuclei in heavy and super-heavy mass region. A comprehensive analysis of spontaneous fission of U to Hs nuclei is presented and its competition with the previous studied ground state decay modes is duly analyzed.

Bibliography

[1] K. Sharma, G. Sawhney, M. K. Sharma and R. K. Gupta, Eur. Phys. J. A **55**, 30 (2019).

[2] A. Săndulescu, D. N. Poenaru, and W. Greiner, Sov. J. Nucl. **11**, 528 (1980).

[3] H. J. Rose and G. A. Jones, Nature (London) **307**, 245 (1984).

[4] S. W. Barwick, P. B. Price, H. L. Ravn, E. Hourani, and M. Hussonnois, Phys. Rev. C **34**, 362 (1986).

[5] S. Kumar, D. Bir, and R. K. Gupta, Phys. Rev. C **51**, 4 (1995).

[6] S. Kumar, J. S. Batra, and R. K. Gupta, J. Phys. G: Nucl. Part. Phys. **22**, 215 (1996).

[7] R. K. Gupta, in Heavy Elements and Related New Phenomena, edited by W. Greiner and R. K. Gupta (World Scientific, Singapore, 1999), Vol. II, Chap. 18, p. 730.

[8] R. K. Gupta, in Proc. 5^{th} Int. Conf. on Nuclear Reaction Mechanisms, edited by E. Gadioli (Ricerca Scientifica ed Educazione Permanente, Milan, 1988), p. 416.

[9] S. K. Arun and R. K. Gupta, Phys. Rev. C **80**, 034317 (2009).

[10] R. Kumar and M. K. Sharma, Phys. Rev. C **85**, 054612 (2012).

[11] G. Sawhney, K. Sandhu, M. K. Sharma, and R. K. Gupta, Eur. Phys. J. A **50**, 175 (2014).

[12] A. Guglielmetti, R. Bonetti, G. Poli, R. Collatz, Z. Hu, R. Kirchner, E. Roeckl, N. Gunn, P. B. Price, B. A. Weaver, A. Westphal, and J. Szerypo, Phys. Rev. C **56**, R2912 (1997).

[13] S. Kumar and R. K. Gupta, Phys. Rev. C **49**, 1922 (1994).

[14] S. Kumar, D. Bir, and R. K. Gupta, Phys. Rev. C **51**, 1762 (1995).

[15] D. N. Poenaru, D. Schnabel, W. Greiner, D. Mazilu, and R. Gherghescu, At. Data Nucl. Data Tables **48**, 231 (1991).

[16] D. N. Poenaru, W. Greiner, and E. Hourani, Phys. Rev. C **51**, 594 (1995).

[17] R. K. Gupta, M. Balasubramaniam, R. Kumar, N. Singh, M. Manhas, and W. Greiner, J. Phys. G **31**, 631 (2005).

[18] J. Maruhn and W. Greiner, Phys. Rev. Lett. **32**, 548 (1974).

[19] R. K. Gupta, W. Scheid, and W. Greiner, Phys. Rev. Lett. **35**, 353 (1975).

[20] H. J. Fink, J. Maruhn, W. Scheid, and W. Greiner, Z. Phys. **268**, 321 (1974).

[21] S. K. Arun, R. K. Gupta, B. B. Singh, S. Kanwar, and M. K. Sharma, Phys. Rev. C**79**, 064616 (2009).

[22] S. K. Arun, R. K. Gupta, S. Kanwar, B. B. Singh, and M. K. Sharma, Phys. Rev. C **80**, 034317 (2009).

[23] R. K. Gupta, M. Balasubramaniam, R. Kumar, N. Singh, M. Manhas, and W. Greiner, J. Phys. G: Nucl. Part. Phys. **31**, 631 (2005).

[24] G. Sawhney, M. K. Sharma, and R. K. Gupta, Phys. Rev. C **83**, 064610 (2011).

[25] P. Moller, J. R. Nix, W. D. Myers, and W. J. Swiatecki, At. Data Nucl. Data Tables **59**, 185 (1995).

[26] G. Sawhney, K. Sharma, M. K. Sharma, and R. K. Gupta, EPJ Web of Conferences **117**, 04013 (2016).

[27] G. Audi and A. H. Wapstra, Nucl. Phys. A **595**, 409-480 (1995).

[28] J. Blocki, J. Randrup, W. J. Swiatecki, and C. F. Tsang, Ann. Phys. (NY) **105**, 427 (1977).

[29] P. Moller and J. R. Nix, Nucl. Phys. A **361**, 117 (1981).

[30] W. Reisdorf, J. Phys. G: Nucl. Part. Phys. **20**, 1297 (1994).

[31] W. D. Myers and W. J. Swiatecki, Phys. Rev. C **62**, 044610 (2000).

Chapter 5

Spontaneous fission and its comparison with competing ground state decay channels

The main focus in Chapter 4 was on the rare radioactive phenomena called as cluster decay or cluster radioactivity. The role of deformations and orientations was analyzed comprehensively along with the effects of different nuclear proximity potentials, and the structural pattern of fragmentation path was analyzed for numerous trans-tin nuclei. As such, no experimental data was available on Sn-radioactivity of these systems, so predictions were made on the half-lives of probable clusters; keeping in mind the upper limits on the cluster decay data. As a next step, the spontaneous fission exhibiting comparable fragments is explored, and the ground state decay of 45 actinide and trans-actinide nuclei is investigated. These nuclear systems range from ^{232}U (Z=92) to ^{264}Hs (Z=108). The mechanism of spontaneous fission is studied within Preformed Cluster decay Model (PCM) and is published in [1]. The mass distributions, barrier characteristics and the corresponding half-lives are addressed for the considered parent nuclei, by using two different forms of radius expressions viz. effective sharp radius and S*ü*ssmann's central radius. Additionally, a competition of spontaneous fission is explored with the other

radioactive decay modes such as α-decay, cluster emission and heavy particle radioactivity, etc. in terms of their fragmentation potential, preformation probability and the related characteristic quantities.

5.1 Introduction

Pioneering studies on various spontaneous (ground state) decays have played leading role to understand the nuclear phenomena and related properties. Discovery of α-radioactivity was instrumental in the earlier nuclear explorations and is considered as the chief decay phenomenon of nuclei in heavy/superheavy mass region. After about four decades from the discovery of alpha radioactivity, nuclear fission was discovered in 1939 [2]. Phenomenon of fission involves the division of a nucleus, with large imbalance and hence large instability, into two comparable fragments. The α-radioactivity, β-radioactivity and nuclear fission provide a useful tool to understand majority of nuclear properties. In 1980, after another four decades from the discovery of fission, it was predicted theoretically that unstable nuclei can attain stability not only by decaying via the above mentioned modes of radioactivity, but also by decaying through a very novel and exotic way, called cluster radioactivity [3, 4]. Here the unstable parent nucleus is assumed to decay into a cluster, which is larger than alpha particle but smaller than the lightest of fission fragments, and daughter nucleus. Apart from this, the authors of [5, 6] suggested the possibility of occurrence of heavy particle radioactivity from super-heavy elements via the spontaneous emission of heavy clusters.

Basically, all the above mentioned decay modes i.e. α-decay, cluster (both light as well heavy) emission and fission correspond to the breakup of a nuclear liquid drop into two fragments having different values of mass asymmetry, and hence are treated as different aspects of ground state decay of nuclear systems. Various theoretical formalisms [7–9] have been coined to explain the above mentioned spontaneous decays. Interesting feature of such a study is that one fragment is always spherical or nearly closed shell nucleus.

The first model that explained the α-decay was given independently by Gamow and Gurney by applying the well established quantum tunnelling effect. It was assumed that the α-particle is already formed inside the decaying nucleus and it keeps on assaulting the surface of the nucleus with definite frequency till it penetrates via the potential barrier with a certain probability. This approach for understanding the decay of nuclei forms the basis of almost all the models developed later for studying various ground state nuclear decays. Mainly there are two different types of models based on Gamow's idea. One such approach refers to Preformed Cluster Models (PCM) [10–13]. In this model, not just alpha particle but all the clusters of different sizes are assumed to be preformed inside mother nucleus with different probabilities depending on the mass of the parent nucleus. After this, the penetration across the potential barrier is similar to Gamow's penetration. In the second type of the models known as Unified Fission Models ($UFMs$); the penetration is considered without bothering about the cluster being preformed or not, inside the parent nucleus. Poenaru and Greiner [14] were the first to do a theoretical calculation for cluster decay by using such criteria, naming Analytical Super Asymmetric Fission Model ($ASAFM$). ASAFM in general, do not carry the relevant structure information. Alternatively, PCM comprises of the structural information of decaying nucleus in terms of the preformation factor. This approach of PCM has been proved to be successful in explaining various ground state properties of the nuclei and related phenomena like cluster radioactivity, alpha decay etc. in different regions of the Periodic table. Knowing that the PCM calculated $T_{1/2}$ is a combined effect of both preformation P_0 and penetration P probabilities, consequently the predicted half life values remain quite sensitive to the curvature and energetics of the barrier potential.

Note that the understanding of mass distributions of fissioning nuclei provides some exciting inputs regarding nuclear behavior and hence one needs to explore it on experimental as well as theoretical front. Some experimental data [15] on SF has been made available in past years, however systematics of this data has not been analyzed in terms of corresponding (most probable) fission fragments. In this chapter, firstly, the spon-

taneous fission half lives are investigated using PCM and attempt has been made to identify the most preferred heavy fragment channel for a number of nuclear systems, varying from heavy to superheavy (SHE) mass domain. Specifically, ^{232,234,235,236,238}U, $^{239-241}$Pu, ^{243}Am, ^{243,245,248}Cm, ^{249}Bk, $^{249-250}$Cf, ^{253}Es, ^{250,252,254,256}Fm, ^{255,257,259}Md, ^{252,254,256,257,259}No, ^{252,253,255,256,257,259}Lr, $^{255-260}$Rf, ^{255}Db, ^{258,260,262}Sg and ^{264}Hs nuclear systems are considered and their structural aspects are analyzed in view of the behavioral patterns of fragmentation potentials. This approach is an extension of earlier studies [16–21] based on PCM calculations, which provides reasonable agreement with the observed data on α- and cluster decay half-life values, and hence extends an opportunity to test its validity in reference to SF dynamics of some 45 nuclei. Further, a possible branching of α-decay with most prominent cluster decay(s) and its possible competition with (spontaneous) fission has been explored from even mass $^{232-238}$U nuclei. In other words, the comparative analysis of possible decay paths of different isotopes of U has been investigated using the collective clusterization method. In addition, several nuclear structural features such as the shell effects, barrier modification, and the fine-structure of decaying fragments have been explored. A comparison of our calculated α-, cluster and SF half-lives is made with the experimental data [15, 22, 23] and other theoretical calculations [24] to emphasize the relevance and applicability of the formalism used.

Section 5.2 of this chapter, gives the details of the calculations for ground state decays of various actinide and transactinide nuclei. Finally, the conclusions are summarized in Sec. 5.3.

5.2 Calculations and Results

The analysis of previous study in reference to cluster decay, alpha decay and heavy particle radioactivity [16–20] is extended here to address the spontaneous fission (SF) in the ground state emission of various parent nuclei, so as to work out the comparative emergence of clusters/fragments of different masses, particularly the fission fragments. Note that no

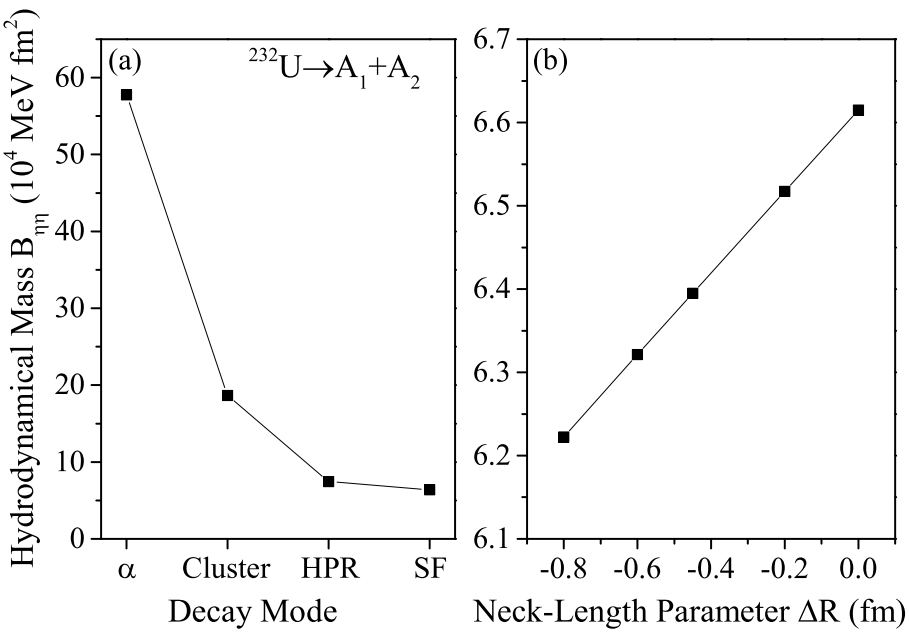

Figure 5.1 The variation of hydrodynamical masses $B_{\eta\eta}$ with the (a) different decay modes and (b) neck length parameter ΔR.

such fragment identification is made in the reported experiments. This section is split into two sub-sections. In Sec. 5.2.1, the fission half-lives of the observed spontaneous fission from ^{232}U to ^{264}Hs parents are calculated within the framework of PCM. Basically, PCM imparts better opportunity in the addressal of the spontaneous decays since preformation factor gives much needed nuclear structure information. The calculations are done at temperature T=0 and negligible or small value of angular momentum (say upto ℓ=5$\hbar$) is specified particularly for neutron rich isotopes of some parent nuclei. The behavior of potential energy surfaces, preformation profile, and barrier lowering effect, etc., is explored so as to have a complete understanding of the nuclear structure effects included. Then, in Sec. 5.2.2, a comprehensive analysis is carried out to explore the different possibilities of decay modes in reference to the dynamics of even A $^{232-238}$U isotopes. Furthermore, the identification of magic or near magic daughter is explored in context of competing decay of SF, $\alpha-$ and other cluster emission processes.

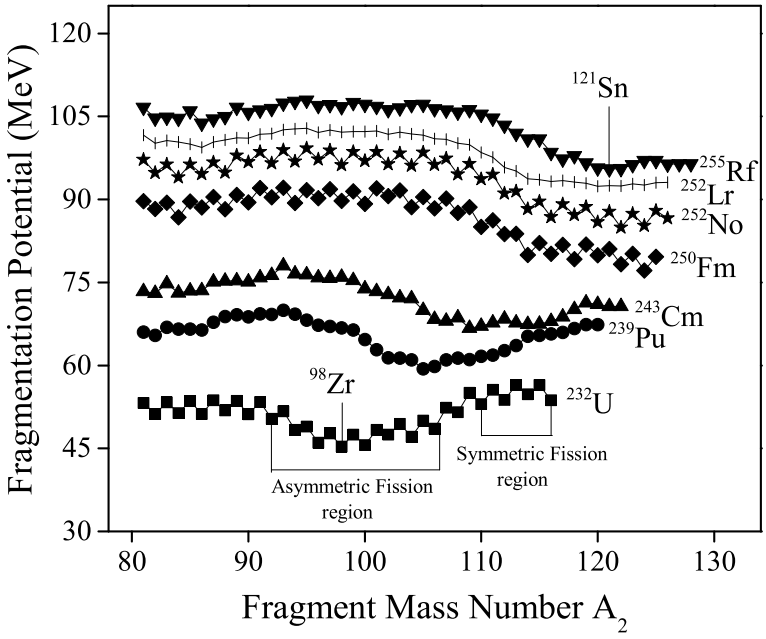

Figure 5.2 Fragmentation potential $V(A_2)$ plotted for various ground state parent nuclei, taking the two emitting fragments as spheres only.

5.2.1 Spontaneous fission analysis of various nuclei ranging from heavy to super heavy region.

Firstly, the fragmentation potential V(A_2) is analyzed in Fig. 5.2 for the chosen ^{232}U, ^{239}Pu, ^{243}Cm, ^{250}Fm, ^{252}No, ^{252}Lr and ^{255}Rf parents, plotted for spherical choice of fragments. The calculations are performed for optimum choice of ΔR, optimized to address the experimental data (refer Figure 5.5, explained later). It may be noted that the minima in the fragmentation potential corresponds to the maxima in the preformation probability of a particular decay mode. Here, the main emphasis is only on the potential energy minima. For the present study, the deformations effects are not included because spherical as well as deformation effects up to β_2 does not influence the status of preferred fragment and/or hence the minima in $V(A_2)$(for details refer Fig. 3 of [19]). The two captivating results are noticed in figure 5.2: (i) significant changes in the magnitude as well as in the structure of PES is observed with increasing mass and charge of parent nucleus which in turn would effect the relative preformation probability P_0 for all the fragments.

Table 5.1 Extracted half-lives compared with available data and other characteristic quantities like barrier lowering parameter ΔV_B, etc. for spontaneous fission of various parent nuclei.

Case	Parent	Decay	Choice of	ΔV_B	$logT_{1/2}(s)$			Q-value
No.	Nucleus	Channel	Radius	(MeV)	PCM	GLDM [24]	Expt. [15]	(MeV)
1	^{232}U	^{98}Zr+^{134}Te	R_t	-11.061	21.54	20.51	21.39	199.24
2	^{234}U	^{100}Zr+^{134}Te	R_t	-10.342	23.62	22.46	23.67	199.35
3	^{235}U	^{101}Zr+^{134}Te	R_t	-8.947	26.63	24.0	26.49	198.77
4	^{236}U	^{102}Zr+^{134}Te	R_t	-9.643	23.85	21.74	23.89	198.97
5	^{238}U	^{106}Mo+^{132}Sn	R_t	-9.988	23.31	21.04	23.41	200.70
6	^{239}Pu	^{105}Mo+^{134}Te	R_t	-9.38	23.21	22.43	23.39	210.04
7	^{240}Pu	^{106}Mo+^{134}Te	R_t	-10.549	18.13	22.7	18.17	210.26
8	^{241}Pu	^{107}Mo+^{134}Te	R_t	-8.38	24.65	22.81	24.36	209.53
9	^{243}Am	^{110}Ru+^{133}Sb	R_t	-8.289	21.80	20.83	21.79	215.90
10	^{243}Cm	^{109}Ru+^{134}Te	R_t	-9.336	19.32	20.64	19.23	221.12
11	^{245}Cm	^{115}Pd+^{130}Sn	R_t	-9.161	19.40	20.93	19.64	222.17
12	^{248}Cm	^{116}Pd+^{132}Sn	R_t	-9.667	14.02	18.66	14.11	223.48
13	^{249}Bk	^{116}Pd+^{133}Sb	R_t	-7.709	16.82	16.32	16.78	228.54
14	^{249}Cf	^{121}Cd+^{128}Sn	R_t	-6.562	18.43	16.39	18.34	234.30
15	^{250}Cf	^{120}Cd+^{130}Sn	R_t	-8.676	11.57	16.61	11.71	235.08
16	^{253}Es	^{125}In+^{128}Sn	R_t	-4.127	13.26	12.41	13.30	243.34
17	^{250}Fm	^{124}Sn+^{126}Sn	R_t	-7.789	7.38	7.65	7.41	248.51
18	^{252}Fm	^{126}Sn+^{126}Sn	R_t	-6.88	9.62	8.20	9.60	249.15
19	^{254}Fm	^{126}Sn+^{128}Sn	C_t	-0.583	5.58	7.71	7.27	250.78
20	^{256}Fm	^{128}Sn+^{128}Sn	C_t	-0.781	1.18	6.23	4.00	253.08
21	^{255}Md	^{126}Sn+^{129}Sb	C_t	-0.515	5.10	5.92	6.04	256.20
22	^{257}Md	^{126}Sn+^{131}Sb	C_t	-0.928	1.97	5.25	6.30	258.20
23	^{259}Md	^{128}Sn+^{131}Sb	C_t	-1.126	-1.41	3.46	3.76	259.89
24	^{252}No	^{122}Sn+^{130}Te	R_t	-7.397	1.12	4.34	1.07	260.24
25	^{254}No	^{124}Sn+^{130}Te	R_t	-6.994	4.57	4.70	4.47	260.57
26	^{256}No	^{124}Sn+^{132}Te	C_t	-2.095	2.03	4.32	2.04	262.17
27	^{257}No	^{125}Sn+^{132}Te	C_t	-1.762	3.21	4.30	3.23	262.48
28	^{259}No	^{126}Sn+^{133}Te	C_t	-0.413	0.68	3.30	4.54	264.27
29	^{252}Lr	^{120}Sn+^{132}I	R_t	-6.02	1.54	2.30	1.55	265.09
30	^{253}Lr	^{122}Sn+^{131}I	R_t	-6.996	1.64	2.96	1.46	265.45

Table 5.2 continue.

Case	Parent	Decay	Choice of	ΔV_B	$logT_{1/2}(s)$			Q-value
No.	Nucleus	Channel	Radius	(MeV)	PCM	GLDM [24]	Expt. [15]	(MeV)
31	^{255}Lr	^{122}Sn+^{133}I	R_t	-6.387	4.08	3.0	4.34	265.88
32	^{256}Lr	^{120}In+^{136}Xe	R_t	-7.006	5.55	3.51	5.95	264.26
33	^{257}Lr	^{124}Sn+^{133}I	C_t	-0.696	3.05	3.04	3.34	267.26
34	^{259}Lr	^{129}Sb+^{130}Te	C_t	-0.363	0.594	2.53	3.76	268.86
35	^{255}Rf	^{121}Sn+^{134}Xe	R_t	-6.505	0.51	1.32	0.50	271.52
36	^{256}Rf	^{122}Sn+^{134}Xe	R_t	-5.824	-2.80	1.60	-2.19	272.14
37	^{257}Rf	^{122}Sn+^{135}Xe	R_t	-6.691	2.64	1.93	2.59	272.37
38	^{258}Rf	^{124}Sn+^{134}Xe	C_t	-3.582	-1.87	1.62	-1.85	273.04
39	^{259}Rf	^{124}Sn+^{135}Te	C_t	-0.947	1.60	1.38	1.60	273.43
40	^{260}Rf	^{130}Te+^{130}Te	C_t	-0.642	-1.70	0.55	-1.29	274.87
41	^{255}Db	^{120}Sn+^{135}Cs	R_t	-6.232	-0.40	-0.45	-0.09	277.70
42	^{258}Sg	^{120}Sn+^{138}Ba	C_t	-2.532	-2.09	-1.53	-2.28	284.11
43	^{260}Sg	^{122}Sn+^{138}Ba	C_t	-2.371	-2.02	-2.38	-2.14	284.66
44	^{262}Sg	^{124}Sn+^{138}Ba	C_t	-1.008	-2.78	-4.40	-2.15	283.12
45	^{264}Hs	^{126}Te+^{138}Ba	C_t	-0.518	-4.47	-7.29	-2.79	297.61

(ii) for the lighter systems, the prominent potential energy minima are observed at the asymmetric fragments whereas symmetric fragmentation dominates for the heavier systems. For example, the PES in case of ^{232}U nuclei clearly show that ^{98}Zr(+^{134}Te) configuration is prominent which shifts to ^{121}Sn(+^{134}Te) for the choice of ^{255}Rf parent. A black vertical line is drawn to indicate the asymmetric (AF) and symmetric (SF) fragmentation regions. In a nutshell, the disintegration of lighter ^{232}U, ^{239}Pu and ^{243}Cm nuclei is primarily via AF, while for the decays of heavier ^{250}Fm, ^{252}No, ^{252}Lr and ^{255}Rf parents, the symmetric fragments contribution becomes dominant, compared to the AF contribution. Such differences in the fission valley structure indicates the possibility of fine structure among fission fragments.

Next, the characteristics of the fragmentation path for some 45 cases of spontaneously fissioning nuclei are investigated, listed in Table 5.1 covering majority of nuclei in actinide and transactinide region. Note that the fragments in the range A_2 = 98-130 appear as

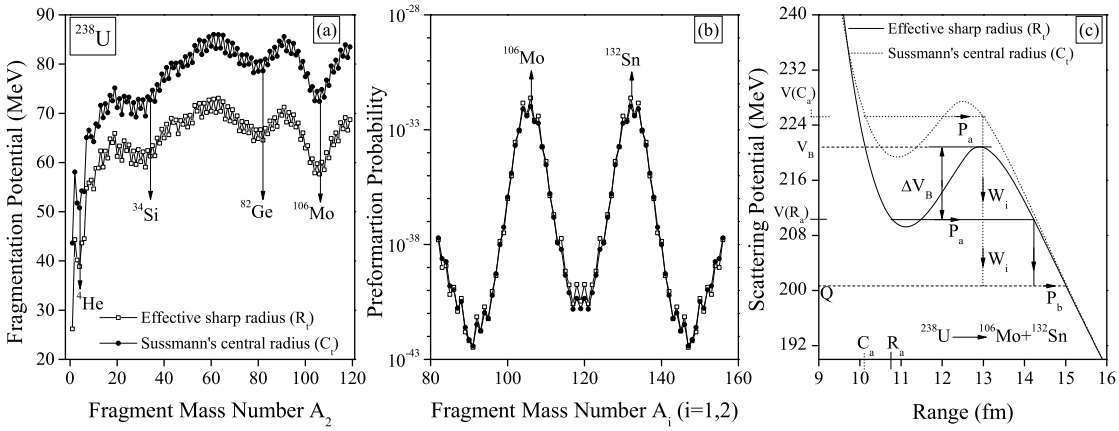

Figure 5.3 (a) The variation of fragmentation potential as a function of fragment mass A_2 for the decay of ^{238}U using two different radii (effective sharp radius R_t and S*ü*ssmann's central radius C_t) approaches. (b) Same as panel (a) but for the fragment preformation probability. (c) Scattering potentials for the spontaneous decay of ^{238}U$\rightarrow^{106}$Mo+^{132}Sn using R_t and C_t, showing the three steps of barrier penetration used in PCM.

the prominent contributors in SF half-lives for the respective fragmentation channels corresponding to ^{232}U-^{264}Hs systems, although symmetric fragments contribute more in heavier mass region contrary to asymmetric fragmentation in lighter nuclei. Table 5.1 shows the results of the PCM based half-lives for the chosen nuclei calculated using two different choice of radii, namely effective sharp radius R_t and S*ü*ssmann's central radius C_t [25], compared with available experimental data [15] (also illustrated in Figure 5.6) and other model calculations [24]. The Q-values are also listed in the table, evaluated by using the binding energy table of [26] and, wherever not available, the theoretical values of [27] are used. The preference for the decay channel is clearly based on the minima in the fragmentation potential and hence for the cases of largest preformation factors P_0, depicted as an instance for the ^{106}Mo fragment emitted from the ^{238}U parent in Fig. 5.3. The choice of different neck's ΔR for different nuclei (and hence different decay channels) suggest their occurrence at different time scales. For majority of the chosen nuclei, the PCM calculated $T_{1/2}$ values address the experimental numbers nicely using one parameter fit of ΔR chosen in reference to effective sharp radius (R_t+ΔR) approach. However, the same doesn't work reasonably well for neutron rich isotopes having heavier masses. It is worth mentioning here that the potential corresponding to first turning point $V(R_a)$

should lie within the dimensions of barrier in order to exercise the penetration process.

However, at smaller neck values, the behavior of $V(R_a)$ was not found to be consistent w.r.t. the above observation and hence the deviation indicates that relatively larger value of ΔR is required to address $T_{1/2}$ data. On the other hand, the calculated half-life times are seen to underestimate the measured SF data by a factor of $\sim$10 seconds at higher neck values, which in turn, suggests that different choice of radius may be required particularly for addressal of SF of neutron rich isotopes. Consequently, the impact of S*ü*ssmann's central radius C_t+ΔR is worked out and interestingly, we are able to address the measured half-lives. Note that, to include centrifugal term of the potential, the case of $\ell = 5\hbar$ is taken, chosen in reference to the C_t approach whereas $\ell = 0\hbar$ is considered for R_t choice. Specifically, for neutron rich isotopes, it is found that the comparison between the calculated and measured half lives improves to a fair extent by considering ℓ effects upto $5\hbar$. Hence, this switching of the radius choice from R_t to C_t along with the dependence of angular momentum with the increase in number of neutrons of parent nucleus, specifically in the SHE mass region provides an interesting case of investigation for further understanding of nuclear behavior.

Further, the comparison of R_t and C_t radius configurations is carried out on the respective fragmentation profile of ^{238}U nucleus. Despite the use of different radii, Fig. 5.3(a) clearly shows that ^{106}Mo is the most probable fission fragment, showing strongest minimum in PES with corresponding ^{132}Sn daughter. In other words, the status of the preferred fragment remains intact independent of the choice of radius used. Except for the change in magnitude, no noticeable change in the structural profile is observed. The above results can also be interpreted in terms of the preformation factor $P_0(A_i)$, plotted in Fig. 5.3(b). P_0 being a relative quantity, its calculation depends not only on the decay products but also on all other possible fragmentation of the parent nucleus. Interestingly, $P_0(A_i)$ are found to be nearly independent of the choice of radius, indicating asymmetric fission mass distribution around A_2=106 (plus complementary heavy fragments) for both the approaches. Apparently, the minima in PES and hence the maxima in preformation

yield corresponds generally to a closed shell nucleus which in turn provides further insight regarding the understanding of nuclear structure effects. One can clearly see from Table 5.1 (and Fig. 5.3) that the shell effects, in all the lighter systems resulting into asymmetric fragments, arise due to doubly magic shell ^{132}Sn or its neighboring daughter fragment. Whereas for the heavier systems decaying via symmetric fission, this effect is mainly attributable to the magicity effect around light fragment charge Z_1=50 and spherical doubly magic around heavy fragment ^{132}Sn having charge Z_2=50 and neutron number N_2=82. Such nuclear shell structure effects are of extreme interest in overall understanding of fission dynamics of the nuclear systems.

Here, it is essential to state that the fragmentation potential used in Fig. 5.3(a) when normalized with respect to binding energy, gives us the scattering potential which is used to calculate the barrier penetrability. The quantum tunnelling penetration probability in a dynamical investigation depends exponentially on the action integral, in which the integral contains a square root of the product of mass parameter B_{RR} and deformation energy. This exponential dependence within the quasi-classical WKB approximation suggests that this approach of the action integral containing the tensor of inertia is necessary in calculation. However, it has been suggested in ref. [28] that the use of effective mass B_{RR} is almost analogous to reduced mass for incompressible irrotational approach. Hence, instead of using B_{RR}, the reduced mass μ is employed for calculating the WKB penetrability P as described in Chapter 2.

Further, in order to see the influence of R_t and C_t on barrier characteristics, it is observed in Fig. 5.3(c) that at a fixed ΔR value, the scattering potential is significantly influenced for the use of different choices of radius. This means that the barrier height V_B and position R_B alter considerably thereby influencing the penetrability. Since the calculated decay $T_{1/2}$ in PCM depends on penetrability P, and hence consequently on the choice of radius, this implies that the use of R_t or C_t approach plays a significant role in investigating half lives and hence on the spontaneous disintegration of a specific nucleus.

One more interesting parameter is the variation of barrier lowering term ΔV_B, plotted

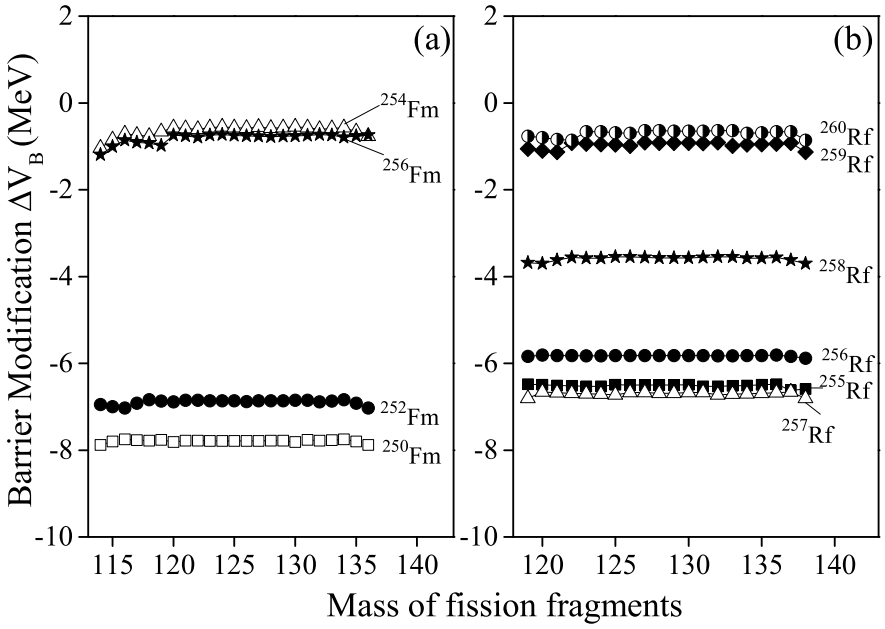

Figure 5.4 Variation of barrier lowering parameter ΔV_B (MeV) with the mass of fission fragments on x-axis for (a) even $^{250-256}$Fm isotopes and (b) $^{255-260}$Rf isotopes.

in Fig. 5.4 for various isotopes of Fm and Rf. This property of "barrier lowering" effects is an intrinsic characteristic of the PCM which has a straight dependence on the corresponding values of ΔR optimized to address the measured data. For a given parent, the variation of ΔV_B is almost independent of the mass of fission fragment and a precise observation of Fig. 5.4 reveals direct isospin (N/Z) dependance of ΔV_B. In other words, the magnitude of barrier modification is observed to be least for heavier isotopes, ^{256}Fm and ^{260}Rf in both the cases, and increases further on decreasing the neutron number of mother nucleus. However, such a systematics is not followed by ^{254}Fm and ^{257}Rf nuclei, shown respectively in panels (a) and (b) of Fig. 5.4, possibly because of the large variation in the observed half life values w.r.t its neighboring isotopes. This behavior of ΔV_B is found to be consistent for majority of the systems studied here as depicted clearly in Table 5.1.

The only parameter used in PCM is the neck length ΔR[=R_a-R_1-R_2 or =R_a-C_1-C_2], shown in Fig. 5.5, optimized for the best possible addressal of the experimental [15] SF decay half-lives data. Apart from providing information regarding the reaction time scale,

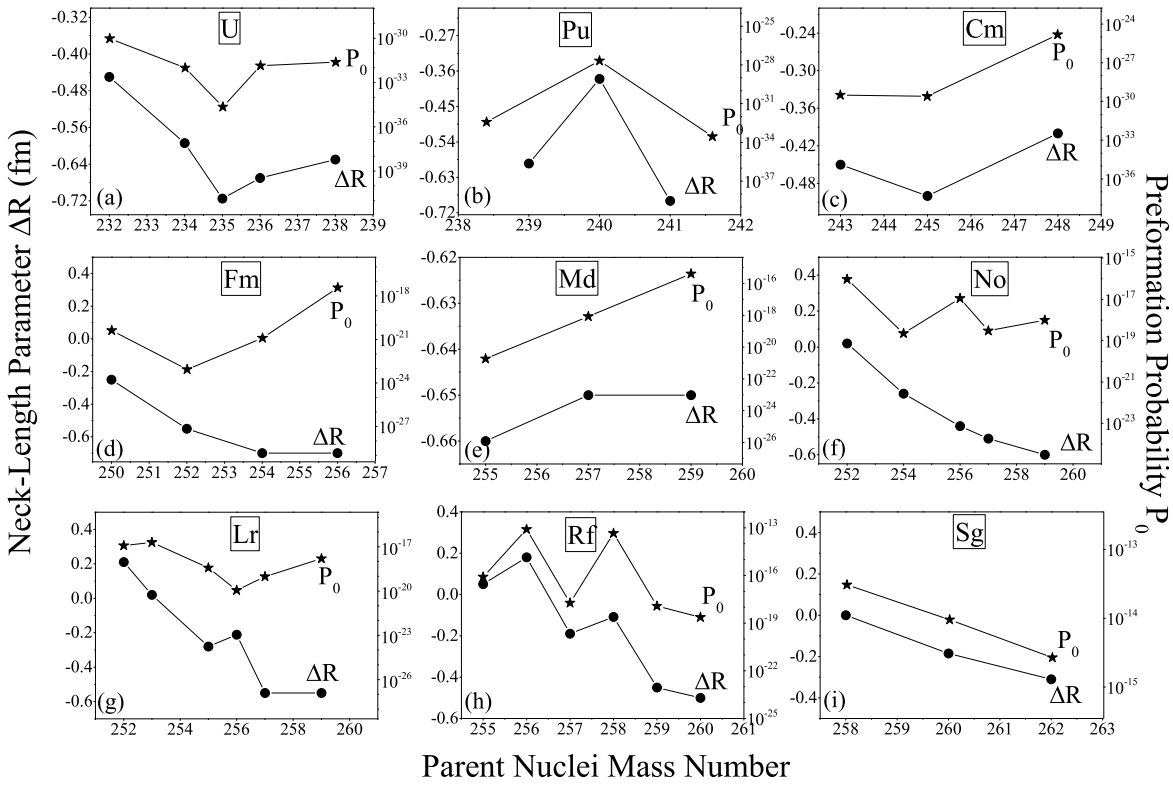

Figure 5.5 The best fit neck-length parameter ΔR in fm (left Y-axis) and preformation probability P_0 (right Y-axis), plotted as a function of parent nuclei mass number A calculated on the basis of PCM for the most favored decays of the parents with Z=92, 94, 96, 100, 101, 102, 103, 104 and 106.

the significance of ΔR lies in the fact that it refers to the barrier position where tunnelling process starts, and hence accordingly influences the barrier penetrability and preformation probability of decaying fragments. The positive ΔR illustrated in Fig. 5.5 indicates that the entrance is shifted towards the barrier position while negative ΔR indicates that the entry level is shifted below the touching configuration R_t. It is noted that the small values of ΔR are used which lie between -0.7 to 0.21 fm for all the studied spontaneous fissioning systems. This variation in ΔR could also be analyzed using polynomial fitting of degree one or two, which in turn could be used to make predictions by extrapolating/interpolating the used values of ΔR. The resulting information could possibly provide directions for new experiments. Similarly, the preformation probability P_0 gives us the probability of pre-born fragments prior to the decay process, and hence accounts for the structure effects of a nuclear system. The observed correlation between ΔR and P_0 for all the chosen 45 cases corresponding to different isotopes of U, Pu, Cm, Fm, Md, No, Lr, Rf and Sg systems in Fig. 5.5 suggests that ΔR is a vital parameter in governing the fission dynamics in heavy and SHE mass region.

As a next step, using the P_0 and P calculated in reference to fragmentation potential $V(A_i)$ (Fig. 5.3(a)) and scattering potential V(r) (Fig. 5.3(c)) respectively for all the chosen parent nuclei, the estimated SF half-lives $T_{1/2}^{SF}$ are illustrated in Fig. 5.6 and presented in Table 5.1 as well. The comparison is made with experimental half-lives [15] and the ones computed with WKB approximation [24]. Except for the ^{256}Fm, ^{257}Md, ^{259}Md, ^{259}No and ^{259}Lr parents, Fig. 5.6 reveals that the PCM evaluated $T_{1/2}$ values find good agreement with the observed numbers, which consequently, provides a confidence that this approach may report the reasonable estimates of the favorable fission fragment. Note that, no such information on the individual fragments has been provided in the available [15] experiment. On the other hand, the reported PCM calculations of SF half lives here correspond to the choice of most preferred fragment in the SF decay of all the parent nuclei, which in turn can allow a testing ground for the future experimental studies. For the sake of comparison, the standard rms deviation is also calculated with

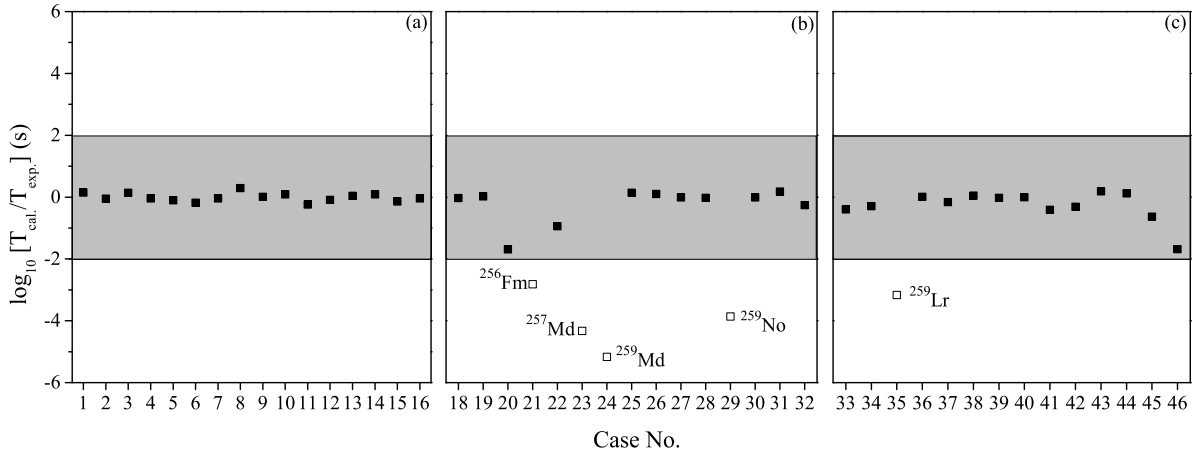

Figure 5.6 Deviations between the logarithms of the PCM calculated half-lives and the experimental ones corresponding to different cases of spontaneous fissioning nuclei, mentioned in Table 5.1.

respect to experimental data using equation below:

$$\sigma = \sqrt{\sum_{i=1}^{n} [log_{10}(T_i/T_{exp.})]^2/(n-1)} \tag{5.1}$$

The magnitude of standard rms deviation σ comes out as 1.958, that seem to suggest that PCM provides reasonable estimates of SF phenomenon along with the various other ground state processes analyzed earlier in the previous [16–20] works.

5.2.2 Competition of α, cluster, heavy cluster and SF decays of U isotopes.

Here, the possible decay modes of even A $^{232-238}$U parents have been explored using collective clusterization approach. This study has been carried out to analyze the competition of SF (reference to Section 5.2.1) with alpha and other possible cluster emissions for the ^{232,234,236,238}U parents. Based on the availability of α, cluster and SF experimental half-life data [15, 22, 23], the present study is limited to only isotopes of U. An effort has been made to accomplish a thorough investigation of shell closure effect of decay fragments, corresponding to different mass regions or else the isospin (N/Z ratio) effect of various

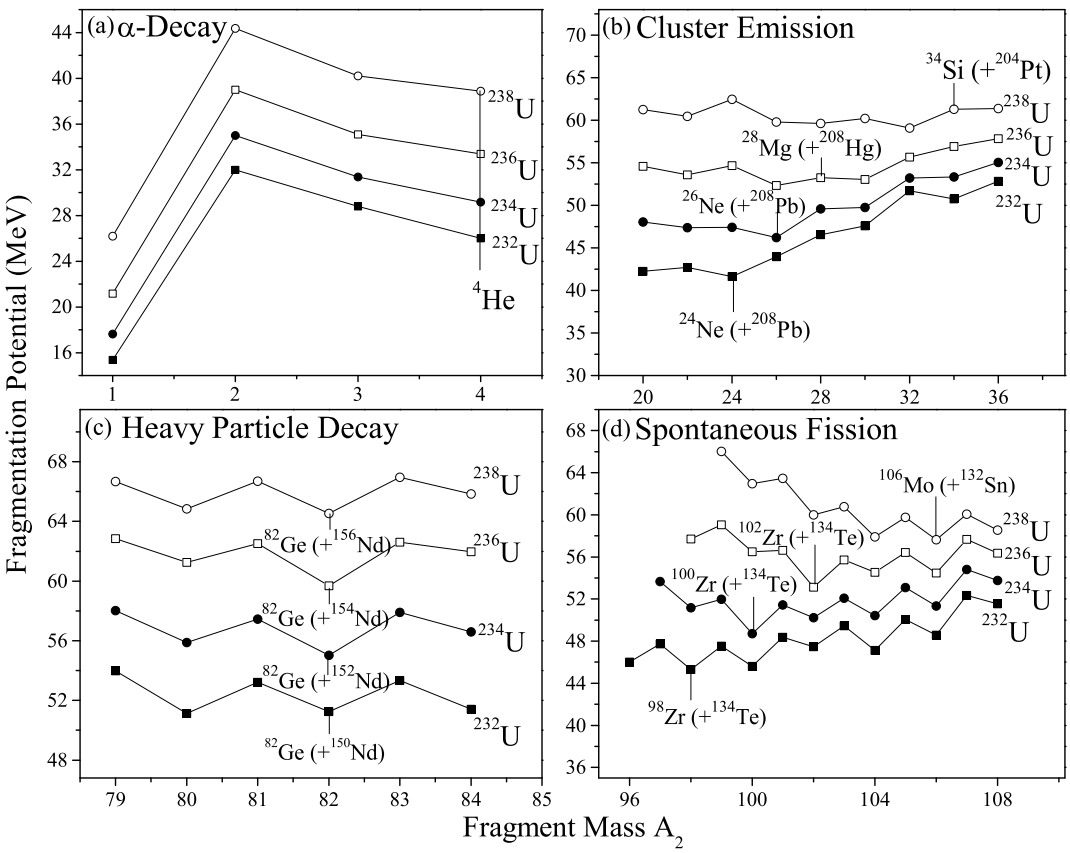

Figure 5.7 Comparative behavior of fragmentation potential for even $^{232-238}$U parents for different decay paths namely (a) alpha radioactivity (b) cluster emission (c) heavy particle decay and (d) spontaneous fission. The choice of most preferred fragment is identified by solid arrows.

mass distributions and related characteristic quantities in the decay of $^{232-238}$U isotopes.

Fig. 5.7 shows comparative behavior of fragmentation potentials, corresponding to different mass regions of the decaying fragments, calculated at a fixed R value for the chosen ^{232,234,236,238}U isotopes. Apart from the α's minima, it is noticed in Fig. 5.7 that in each case, there is a minima corresponding to cluster region (panel (b)) in addition to at least two other minima referring to heavy mass (panel (c)) and asymmetric mass fragments (panel (d)) which allow us to extract significant information regarding the structural aspects in decay of U isotopes. The same result has been analyzed earlier in Fig. 5.3 for ^{238}U only, though the calculated fragment preformation distribution P_0 in Fig. 5.3(b) was illustrated for the spontaneous fissioning region only. In addition to the α-particle (Fig. 5.7(a)), the potential energy minima in Fig. 5.7(b) show a clear preference

for experimentally observed clusters ^{24}Ne, ^{26}Ne, ^{28}Mg and ^{34}Si thereby suggesting the probable occurrence of possible cluster emission, respectively from ^{232}U, ^{234}U, ^{236}U and ^{238}U parents. Also, the appearance of heavy cluster ^{82}Ge and the complementary daughter fragment in Fig. 5.7(c) is found equally favored for all the chosen parents which further indicates that HPR is competing with $\alpha-$ and cluster decay processes. Note that the stability of heavy fragment ^{82}Ge can be accredited to the neutron magicity at N=50, which may be verified via future experiments, and may provide useful information regarding further understanding of related aspects.

In reference to the analysis of fission region from Fig. 5.7(d), it is noticed that the fragments in the mass range A_2= 98-106 show their contribution towards SF half lives of $^{232-238}$U nuclei, however such identification is not exercised in experiments so far. The behavior of potential energy surfaces (PES) is clearly asymmetric for ^{232}U, however the contribution of symmetric fragments starts dominating as we increase the mass of U isotopes. In other words, symmetric fragmentation is preferred for neutron rich isotopes. These differences in the fission valley structure of fragmentation potentials or, equivalently, in preformation yields suggest the presence of a fine structure or substructure effects among the fission fragments.

Clearly for ^{232}U nucleus, the closed shell effects of doubly magic ^{208}Pb on ^{24}Ne, ^{134}Te on ^{98}Zr fragments are clearly depicted here in terms of strong minima in Figs. 5.7(b) and 5.7(d) of fragmentation characteristics $V(A_2)$ (or equivalently, as a shoulder in P_0, shown explicitly for ^{238}U in Fig. 5.3(b) for both light and heavy mass region). The same result holds well for different ^{234,236,238}U parents, thereby providing much needed information regarding the structural behavior of these exotic nuclei.

Similarly, the barrier characteristics in terms of barrier height, barrier position and frequency are found to be significantly affected for the choice of different decay channels. It is clear from Fig. 5.8 that the scattering potential varies significantly for alpha, cluster, heavy cluster and SF decay paths of ^{232}U, thereby affecting penetrability P, and hence the decay half-life $T_{1/2}$ also. The barrier penetration path is also shown in the same

Table 5.2 PCM estimated preformation probability P_0, penetrability P and half-life times $T_{1/2}$ for α, cluster, heavy fragment and SF decays. The relevant comparison is made with the available data. The choice of the outgoing channel for each decay mode is based on the most probable fragment having highest preformation probability factor. Note that in each case, we refer here to calculations with $\ell = 0\hbar$ and consider spherical choice of fragments. For best fit to α-decay, cluster emission and SF data, ΔR values are respectively 0.8fm, 0.5fm and -0.5fm for $^{232-238}$U whereas ΔR=-0.25 fm is chosen for heavy particle decay paths for all the U isotopes, by assuming that it lies in between that for the cluster and SF.

Decay	Decay	P_0	P	$log_{10}T_{1/2}(s)$	
Modes	Channel			PCM	Expt.
Alpha(α)	^{232}U $\rightarrow$ ^{4}He+^{228}Th	$1.99X10^{-10}$	$2.46X10^{-24}$	11.81	9.34 [22]
Cluster	^{232}U $\rightarrow$ ^{24}Ne+^{208}Pb	$1.08X10^{-25}$	$3.84X10^{-19}$	21.73	21.14 [23]
HPR	^{232}U $\rightarrow$ ^{82}Ge+^{150}Nd	$1.02X10^{-33}$	$1.29X10^{-17}$	28.26	-
SF	^{232}U $\rightarrow$ ^{98}Zr+^{134}Te	$9.57X10^{-31}$	$7.47X10^{-14}$	21.54	21.39 [15]
Alpha(α)	^{234}U $\rightarrow$ ^{4}He+^{230}Th	$1.68X10^{-10}$	$7.64X10^{-27}$	14.41	12.88 [22]
Cluster	^{234}U $\rightarrow$ ^{26}Ne+^{208}Pb	$3.08X10^{-28}$	$8.25X10^{-23}$	27.97	25.92 [23]
HPR	^{234}U $\rightarrow$ ^{82}Ge+^{152}Nd	$1.48X10^{-34}$	$2.10X10^{-17}$	28.90	-
SF	^{234}U $\rightarrow$ ^{100}Zr+^{134}Te	$9.91X10^{-33}$	$6.10X10^{-14}$	23.62	23.67 [15]
Alpha(α)	^{236}U $\rightarrow$ ^{4}He+^{232}Th	$8.85X10^{-11}$	$2.44X10^{-28}$	16.19	14.86 [22]
Cluster	^{236}U $\rightarrow$ ^{28}Mg+^{208}Hg	$6.47X10^{-32}$	$1.16X10^{-22}$	27.80	27.58 [23]
HPR	^{236}U $\rightarrow$ ^{82}Ge+^{154}Nd	$6.93X10^{-34}$	$2.08X10^{-17}$	29.00	-
SF	^{236}U $\rightarrow$ ^{102}Zr+^{134}Te	$1.36X10^{-32}$	$2.63X10^{-14}$	23.85	23.89 [15]
Alpha(α)	^{238}U $\rightarrow$ ^{4}He+^{234}Th	$8.38X10^{-11}$	$6.62X10^{-30}$	17.80	17.14 [22]
Cluster	^{238}U $\rightarrow$ ^{34}Si+^{204}Pt	$6.99X10^{-32}$	$2.31X10^{-21}$	29.15	29.04 [23]
HPR	^{238}U $\rightarrow$ ^{82}Ge+^{156}Nd	$7.10X10^{-35}$	$1.22X10^{-17}$	29.45	-
SF	^{238}U $\rightarrow$ ^{106}Mo+^{132}Sn	$2.43X10^{-32}$	$5.23X10^{-14}$	23.31	23.41 [15]

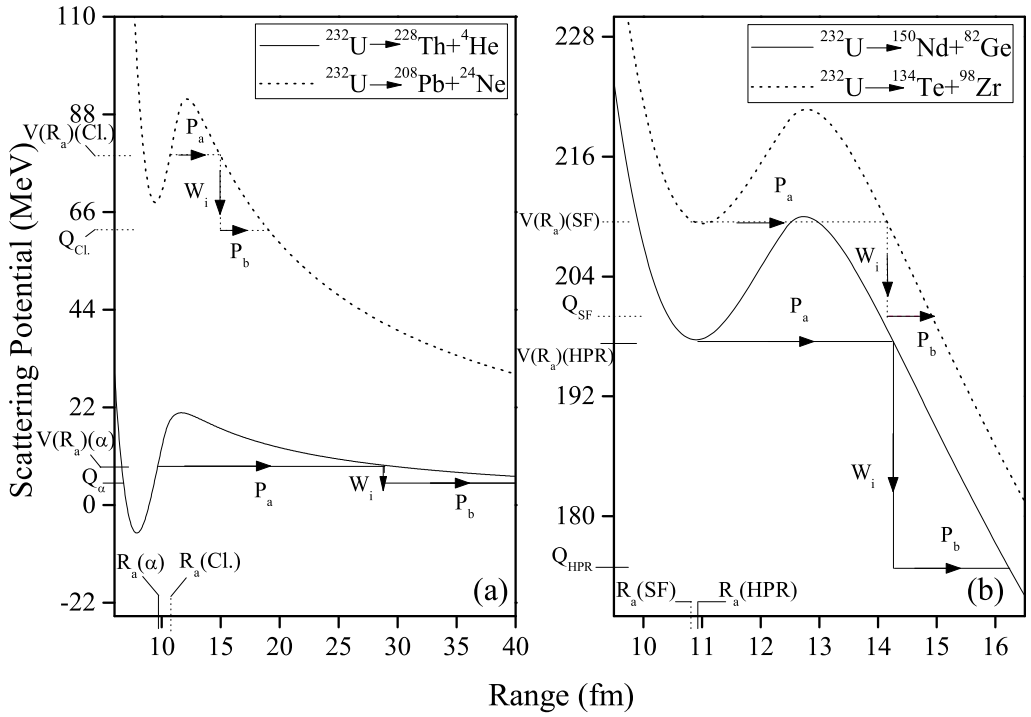

Figure 5.8 The scattering potential for the four possible decay modes occurring in ^{232}U showing steps of barrier penetration with both the daughter and cluster taken as spherical only. The path of barrier tunnelling is also depicted.

figure. Note that, the penetration between two turning points in PCM is divided into three different processes in order to account for the decay into the ground state of the daughter nucleus and the emitted cluster.

Next, the investigation of the dependence of the penetrability on the Q-value is accomplished as illustrated in Fig. 5.9 plotted as a function of asymmetry of daughter and cluster mass numbers. As smaller Q-value indicates relative decrease in penetration probability, the same result is presented here. It is seen that the penetrability follows the trend of Q-value and hence decreases on increasing the mass asymmetry of the decay channel. In other words, the decay probability is strongly influenced and found to be larger for SF followed by HPR, cluster and alpha decay processes. This observation implies that Q-value of emitting fragments plays important role in studying the binary clusterization process of a nucleus.

The consequences of the above results, in terms of P_0 and P are shown explicitly

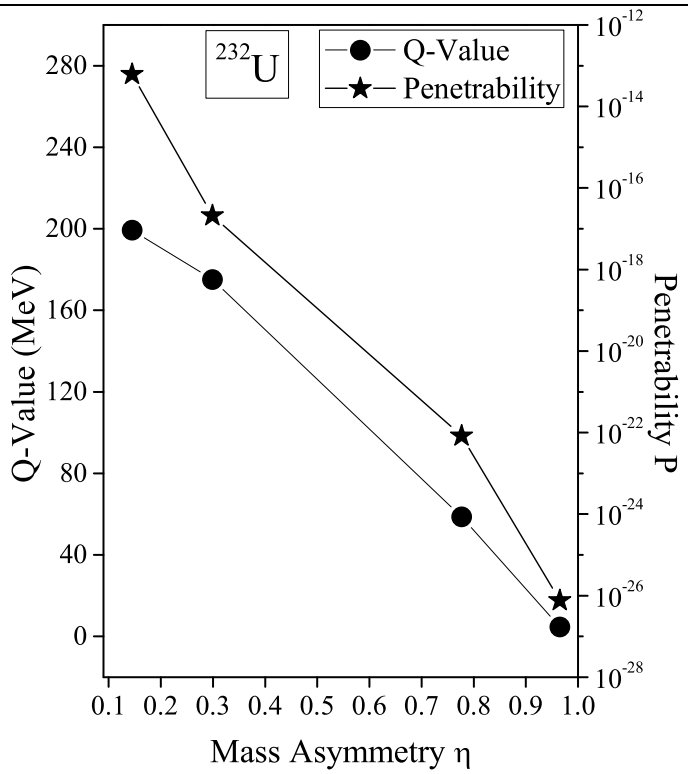

Figure 5.9 Variation of Q-value (MeV)(left Y-axis) and penetrability P (right Y-axis) with the mass asymmetry of the emitted fragments for the parent nucleus ^{232}U.

in Fig. 5.10 and Table 5.2 along with the decay half life $T_{1/2}$ for α-emission, SF and the most preferred clusters emitted from even mass $^{232-238}$U parents. The extracted half-lives in Table 5.2 find decent comparison with observed experimental data for all the probable decay modes in even mass $^{232-238}$U isotopes. Irrespective of the choice of parents, the measured half-lives are attained at a fixed neck value of 0.8fm, 0.5fm and -0.5fm respectively for alpha, cluster decay and SF processes. In other words, for a given parent, the different decay products are observed to form at different time scales and thus the use of different ΔR values seems justified. For the case of heavy cluster decays, no experimental measurement is available till date, therefore the choice of neck length (=-0.25fm) is made on the basis of assumption that ΔR for HPR lies in between the cluster and the SF decays.

Moreover, for all the considered parents, the closed shell effects of daughter/cluster seem to play crucial role in investigating the spontaneous decays and the related structural effects in case of U isotopes. The calculated decay half-lives in Fig. 5.10 present some

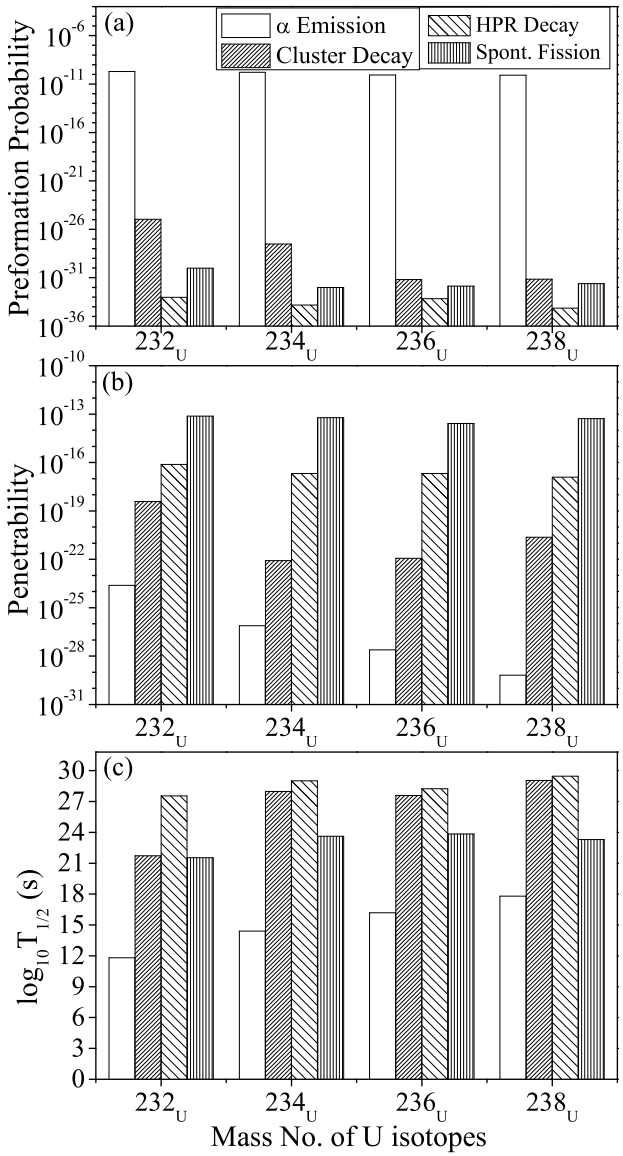

Figure 5.10 Histogram representation of (a) preformation probability (b) penetrability and (c) logarithm of decay half-lives for the four different decay modes (α-, cluster, heavy particle and SF) of ground state parent nuclei ^{232}U, ^{234}U, ^{236}U and ^{238}U.

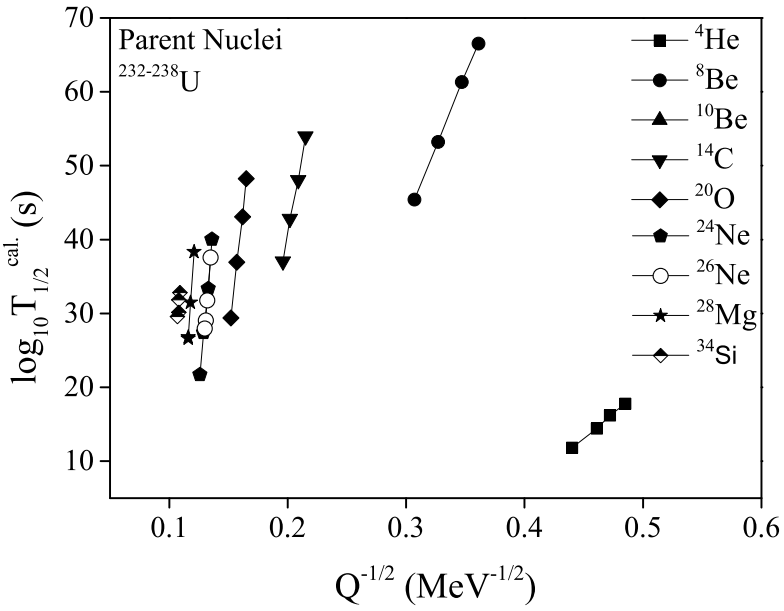

Figure 5.11 Geiger-Nuttal plots of $log_{10}T_{1/2}^{PCM}$ (s) vs $Q^{-1/2}$ for various clusters emitted from $^{232-238}$U.

interesting results: (i) ^{4}He is always preformed having largest probability in all parent nuclei, though its corresponding P values are significantly small. Such a result is important since $T_{1/2}$ is a combined effect of both P_0 and P (ν_0 being a constant). (ii) alpha decay $T_{1/2}$ for ^{238}U is higher in comparison to ^{232}U, ^{234}U and ^{236}U parents, which mean that ^{238}U nuclear system is comparatively stable against alpha-decay than others. (iii) the heavy cluster ^{82}Ge, seems to be preformed with larger P_0 value, compared to ^{24}Ne, ^{26}Ne, ^{28}Mg, ^{34}Si respectively, in ^{232}U, ^{234}U, ^{236}U and ^{238}U parents. The calculated half-lives for ^{82}Ge heavy clusters lie within the present limits of experiments, thereby presenting themselves as future fascinating cases of cluster decay measurements. Thus, one may consider the possibility of heavy fragment in addition to alpha emission, cluster or fission fragmentation of nuclear systems.

In view of the fact that fragments appearing at minima in the potential $V(\eta)$ (Fig. 5.7) correspond to the probable configuration w.r.t. its neighboring clusters, an effort has been made in Fig. 5.11 to examine the Geiger-Nuttal (GN) plot for different clusters decaying from $^{232-238}$U. Some of the clusters like ^{8}Be, ^{10}Be, ^{14}C are not shown in Fig. 5.7 because the present calculations are directed more towards the exotic decays appearing

in different mass regions of the chosen $^{232-238}$U parents. However, the same could be seen clearly preferable in terms of the minima in complete fragmentation plot shown for ^{238}U in Fig. 5.3(a). It is observed in Fig. 5.11 that the $\log_{10}T_{1/2}$ vs $Q^{-1/2}$ plot for each cluster exhibits nearly a straight line but with different slopes and intercepts. In other words, the equation of the straight line (the GN law) for each cluster comes out to be different. This difference of slope and intercept for each cluster is probably associated with their different preformation P_0 and penetration factor P. Such studies might be of extreme interest in exploring cluster dynamics and its related aspects for better understanding of nuclear behavior involved in such processes.

5.3 Summary

Summarizing, 45 cases of spontaneous fission of various parent nuclei have been studied, varying from ^{232}U - ^{264}Hs using PCM with spherical choice of decay products. Although PCM has been applied earlier for spontaneous emission studies like alpha decay, cluster emission and heavy particle radioactivity in recent past; the same is being implemented here in view of spontaneous fission (SF) process and its competing analysis with other spontaneous decay mechanisms such as $\alpha-$, cluster, HPR, etc. Various issues related to shell effects, fine structure/sub-structure of fission fragments, isospin effect, etc. have been addressed. The reported SF half-lives for all these nuclei are nicely addressed using PCM calculations performed in the framework of different choice of radius, namely effective sharp radius and S*ü*ssmann's central radius. The most probable decay fragments are identified, and the fragments in range A_2 = 98-130 appear as the leading contributors in SF half-life times for the considered cases. Apart from this, an effort is made to explore the decay path of even mass nuclei $^{232-238}$U, in terms of α-emission along with most probable cluster decay(s), with a way to identify the magic or near magic daughter(s) in the exotic emission process. Such a study offers two important results: firstly, the appearance of heavy cluster ^{82}Ge and its complementary daughter is observed in all the chosen parents,

thereby pointing out some future possibilities with such exotic emissions in ground state decay. Secondly, the behavior of neck length parameter indicates that a particular decay mode occurs almost simultaneously in the decay of different U isotopes. Such a result seems interesting to analyze various spontaneous decays and provide new directions for future measurements.

Apart from various ground state decay mechanisms as studied in the previous chapters, heavy-ion induced fission of compound nuclear systems is also worked out in Chapter 6 of this thesis. The induced fission of heavy ^{181}Re* and ^{244}Pu* compound nuclei is worked out in the framework of dynamical cluster-decay model (DCM). Beside this, the comparison of excited and the spontaneous fission is analyzed so as to extract the useful information regarding the structural behavior involved in these decay paths.

Bibliography

[1] K. Sharma, G. Sawhney and M. K. Sharma, Phys. Rev. C **96**, 054307 (2017).

[2] N. Bohr, J. A. Wheeler, Phys. Rev. **56**, 426 (1939); G. N. Flerov, K. A. Petrjak, Phys. Rev. **58**, 89 (1940).

[3] H. J. Rose and G. A. Jones, Nature (London) **307**, 245 (1984).

[4] A. Sandulescu, D. N. Poenaru and W. Greiner, Sov. J. Nucl. **11**, 528 (1980).

[5] D. N. Poenaru, R. A. Gherghescu, W. Greiner, Phys. Rev. Lett. **107**, 062503 (2011).

[6] D. N. Poenaru, R. A. Gherghescu, W. Greiner, Phys. Rev. C **85**, 034615 (2012).

[7] D. N. Poenaru, M. Ivascu, A. Sandulescu and W. Greiner, Phys. Rev. C **32**, 572 (1985).

[8] G. Royer, R. K. Gupta and V. Yu Denisov, Nucl. Phys. A **632**, 275 (1998).

[9] B. Buck and A. C. Merchant, J. Phys. G **15**, 615 (1989).

[10] R. K. Gupta, in Proceedings of the 5th International Conference on Nuclear ReactionMechanisms, Varenna, edited byE. Gadioli (Ricerca Scientifica ed Educazione Permanente, Milano, 1988), p. 416.

[11] S. Kumar and R. K. Gupta Phys. Rev. C **55**, 218 (1997).

[12] S. S. Malik and R. K. Gupta Phys. Rev. C **39**, 1992 (1989).

[13] S. K. Arun, R. K. Gupta, S. Kanwar, B. B. Singh and M. K. Sharma, Phys. Rev. C **80**, 034317 (2009).

[14] D. N. Poenaru and W. Greiner, Phys. Scr. **44**, 427 (1991).

[15] N. E. Holden, D. C. Hoffman, Pure Appl. Chem. **72**, 1525 (2000).

[16] G. Sawhney, M. K. Sharma and R. K. Gupta, Phys. Rev. C **83**, 064610 (2011).

[17] R. Kumar and M. K. Sharma, Phys. Rev. C **85**, 054612 (2012).

[18] R. Kumar, K. Sandhu, M. K. Sharma and R. K. Gupta, Phys. Rev. C **87**, 054610 (2013).

[19] G. Sawhney, K. Sandhu, M. K. Sharma, and R. K. Gupta, Eur. Phys. J. A **50**, 175 (2014).

[20] Niyti, G. Sawhney, M. K. Sharma and R. K. Gupta, Phys. Rev. C **91**, 054606 (2015).

[21] G. Sawhney, K. Sharma, M. K. Sharma and R. K. Gupta, EPJ Web of Conf. **117**, 04013 (2016).

[22] G. Audi, F. G. Kondev, M. Wang, B. Pfeiffer, X. Sun, J. Blachot and M. MacCormick, Chin. Phys. C **36**, 1157 (2012).

[23] R. Bonetti and A. Guglielmetti, Rom. Rep. Phys. **59**, 301 (2007).

[24] X. Bao, H. Zhang, G. Royer and J. Li, Nucl. Phys. A **906**, 1 (2013).

[25] G. S*ü*ssmann, Z. Phys. A **274**, 145 (1975).

[26] G. Audi, A. H. Wapstra, Nucl. Phys. A **595**, 4 (1995).

[27] P. Möller, J. R. Nix, W. D. Myers, W. J. Swiatecki, At. Nucl. Data Tables **59**, 185 (1995).

[28] D. N. Poenaru, R. A. Gherghescu and W. Greiner, Eur. Phys. J. A **24**, 355 (2005).

Chapter 6

Induced fission analysis of heavy nuclei

Chapter 5 of the thesis was devoted to the mechanism of spontaneous fission of actinide and trans-actinide nuclei. The probable emitting fragments were identified and the respective half-lives were calculated in reference to the experimental data. An exclusive analysis was made to compare the spontaneous fission with other competing radioactive decay modes studied in the previous Chapters 3 and 4. Further, after exploring spontaneous fission in heavy and super-heavy mass region in Chapter 5, the heavy-ion induced fission of two compound nuclear systems is presented in this chapter. Firstly, the fission decay dynamics of $^{181}Re^{*}$ nucleus is studied at various projectile energies. The fission cross-sections are calculated and are compared with the available experimental data. The predictions on fission emission times and the decay widths of the probable fission fragments are made. Secondly, the decay dynamics of compound nucleus $^{244}Pu^{*}$ formed via $^{6}He+^{238}U$ reaction is explored. The fission cross-sections are calculated and compared with the experimental data. Further, due to the availability of fission half-life data of some other isotopes (i.e. $^{236-244}Pu$) of Pu, an attempt has been made to address the spontaneous fission of these isotopes in order to compare both the fission mechanisms occurred via ground state and excited state mode in view of their preformation probability

and barrier characteristics. Additionally, the structural profile of ^{244}Pu is compared in view of induced and spontaneous fission so as to pin point the role of temperature and energy on the mass distribution and barrier profile of the considered nuclear system.

6.1 Introduction

The fission of heavy nuclei, both spontaneous and induced, is one of the most important field of investigation, both experimentally and theoretically. Basically the phenomenon of nuclear fission corresponds to the subdivision of a heavy nucleus, which may take place spontaneously in some radioactive nuclei or may be induced by the excitation of the nucleus with a variety of particles, like neutrons, protons, deuterons, or α-particles, the heavy-ions, or with electromagnetic radiations in the form of γ rays. Generally, it is the fission process that determines the boundaries of the Periodic system of elements for heavy nuclei. It is important to note that the phenomenon of induced fission is different from that of spontaneous fission (SF) (already presented in Chapter 5). In case of SF, both heavy and light fragments are observed concurrently, as compared to the induced-fission phenomenon where, just the light-fragment half-life times are determined. In latter case, in addition to the fission fragments, it is observed that there is possibility of emission of intermediate mass fragments (IMFs, $5 \leq A \leq 20$, $3 \leq Z \leq 10$) and multiple light particles (LPs, like n, p, and α), called evaporation residues (ER, $A \leq 4$, $Z \leq 2$), at a given excitation energy E^*.

Concentrating only on the fission dynamics of heavy-ion induced reactions, one of the interesting topics of low-energy nuclear dynamics is the investigation of fission mass distribution of nuclei formed in heavy ion induced reactions. Mass distribution has a close relationship with the potential-energy landscape of the fissioning nuclei as demonstrated in saddle- and scission-point models [1, 2]. The understanding of mass distributions of fissioning nuclei gives useful inputs regarding nuclear properties and related dynamics, and hence one needs to explore it on an experimental as well as theoretical front. Re-

cently, experiments [3–6] have generated mass distributions of heavy compound nuclei to analyze the influence of entrance channel parameters, projectile energy, angular momentum, etc. Some of these studies have attempted to identify the fission fragments emitting in the process. But the proper knowledge of these emitting fission fragments is not yet fully understood. Also, the precise understanding of the emitting fragments is of extreme importance, as it gives the information regarding various decay characteristics such as emission times of the emitting fragments, their respective barrier parameters, etc. Significant efforts have been put forward to measure the fission emission times (τ_f) using various experimental as well as theoretical techniques. Where one experimental technique suggests the fission lifetime of the order of attosecond (10^{-18}s) using crystal blocking measurements [7, 8], on the other hand, it is found to be $\approx 10^{-20}$s with the use of pre-scission particle multiplicities [9, 10]. However, according to the recent dynamical model calculations [11], this lifetime is found to be more than attosecond for super-heavy nucleus Z=120. In view of the large range of fission time scales obtained from the different techniques, it will be interesting to investigate the τ_f of fission fragments decaying from compound nuclei in various mass zones of periodic table, as it is expected to vary with the mass range of the compound systems.

The process of heavy-ion induced fission has been explored broadly for extremely fissile actinide nuclei, still it needs further investigations in between the lanthanide and actinide region. An experiment has been performed recently on the pre-actinide compound system ^{181}Re* [3] in which the mass distributions of fission fragments are analyzed in addition to the cross sectional analysis of the individual fission fragments. Motivated by the work of [3], an effort has been made to explore the dynamics of ^{12}C+^{169}Tm reaction forming compound system ^{181}Re* at three beam energies $E_{Lab.}$=77.18 MeV, 83.22 MeV and 89.25 MeV using Dynamical Cluster-decay Model (DCM) [12–16] which is framed under Quantum Mechanical Fragmentation Theory (QMFT) [17–19], and the results obtained from the same are presented in section 6.2.1 of the present chapter. The barrier characteristics and the mass distributions of fissioning nuclei depend upon the deformations and orienta-

tions, therefore such effects are duly incorporated. Further, the total fission cross sections have been addressed by optimizing the value of neck-length parameter ΔR at maximum angular momentum (ℓ_{max}) value. The cross sections evaluated for the emitting clusters of the compound nucleus reveals the probability of occurrence of a specific decay channel. In DCM, the cross-sections are extracted via using the two kinds for probabilities viz. preformation probability (P_0) and barrier penetration probability (P). The cross-sectional yield is expected to reflect the preformation distributional yield/mass distributions shown via P_0. The comprehensive investigation of fragmentation potential, preformation factor, barrier penetrability, and barrier modification effects has been worked out to obtain better picture of the dynamics involved. Moreover, the fission emission times (τ_f) of the fragments emitting from compound system ^{181}Re* are also predicted and presented in this section, which may be validated via future experiments on heavy-ion induced fission.

Furthermore, moving towards the next section 6.2.2 of this chapter, the fission dynamics of ^{244}Pu* formed in ^{6}He+^{238}U reaction is examined. The fission cross-sections are estimated while considering spherical and deformed shape of decaying fragments. As the spontaneous fission half-life data of some Pu isotopes is available, so an effort is made to explore the ground state fission of Pu isotopes, so that both the fission mechanisms be compared in view of their structural and barrier distributions.

Section 6.2.1 and 6.2.2 give, respectively, the details of the calculations and results obtained for ^{181}Re* and ^{244}Pu* compound nuclei. Finally, the conclusions are summarized in Section 6.3.

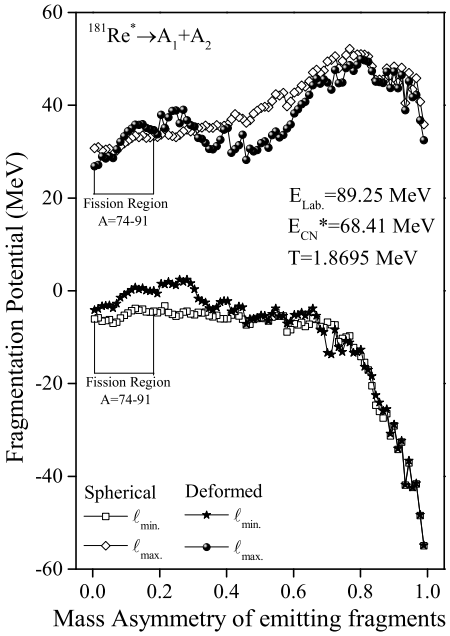

Figure 6.1 Variation of fragmentation potential as a function of mass asymmetry of emitting fragments η at highest energy for extreme values of angular momentum ($\ell_{min.}$ and $\ell_{max.}$) considering spherical and deformed choices of fragmentation.

6.2 Calculations and Results

6.2.1 Fission dynamics and related aspects of $^{181}Re^{*}$ nucleus formed in ^{12}C induced reaction

In this section, an effort has been made to investigate the fission mechanism of $^{181}Re^{*}$ nucleus formed via $^{12}C+^{169}Tm$ reaction at three lab energies with respect to the data of [3]. The calculations are performed using Dynamical Cluster-decay Model (DCM). In the current study, the key focus is to analyze mass distribution of the fission fragments at projectile energies 77.18, 83.22 and 89.25 MeV. For this purpose, the preformation probabilities of emitting fission fragments have been calculated. The barrier characteristics such as barrier height, scattering potential, penetration probability, etc. of the various fission fragments have been examined so as to understand the specifics of fission mech-

anism. The total fission cross sections are calculated and are compared in reference to available experimental data [3]. The predictions on the fission emission times (τ_f) and decay widths (Γ_f) of the emitting fragments are made at three beam energies. Beside this, the preformation profiles for spontaneous and induced fission of compound system ^{181}Re nucleus are analyzed to compare the mass distribution of fission fragments in both the fission paths.

Firstly, to examine the decay of compound system ^{181}Re*, fragmentation potential (V(η)) is plotted in Fig. 6.1 at the highest compound nucleus excitation energy (CN) energy i.e. E^*_{CN}=68.41 MeV at two extreme values of angular momentum (ℓ). For spherical fragmentation, ℓ_{min}=37$\hbar$ and ℓ_{max}=124$\hbar$ whereas for the deformed approach, the ℓ_{min}=33$\hbar$ and ℓ_{max}=113$\hbar$. It is to be noted that the present study is focussed on the fission decay mode, therefore, mass asymmetry η close to zero will be of interest in this case. Fig. 6.1 demonstrates the role of angular momentum on the emergence of light and heavy mass fragments emitted together with the usual fission contribution. It is worth mentioning that minimum in fragmentation potential corresponds to the higher preformation probability of that binary pair. It is seen that fission dominates at higher ℓ-values while evaporation residues (ERs) and intermediate mass fragments (IMFs) are more prominent at lower values of angular momentum. Beside this, the fission mode competes with the heavy mass fragments (HMFs) at the higher ℓ-values. It is important to note here that the IMFs are the fragments/clusters in the mass range 5$> A \geq$20 while HMFs represent probable fragments in between IMF and fission and generally read as 20$> A \geq (A/2)$-20. It is evident from Fig. 6.1 that deformation of decaying fragments plays significant role at lower as well as higher ℓ-values. Interestingly, the deformation effects seem more prominent in IMF and HMF region (η-large) than for fission fragments (η-small). Further, since the minima in fragmentation potential for fission region lies at A$\sim$74-91, thus it is clear from Fig. 6.1 that fission region at the ℓ_{max} value ranges from A$\sim$74-91 for both spherical as well as deformed choice which is in agreement with the observed experimental results [3]. In the methodology of DCM, cross-sections σ reflect behavior of preforma-

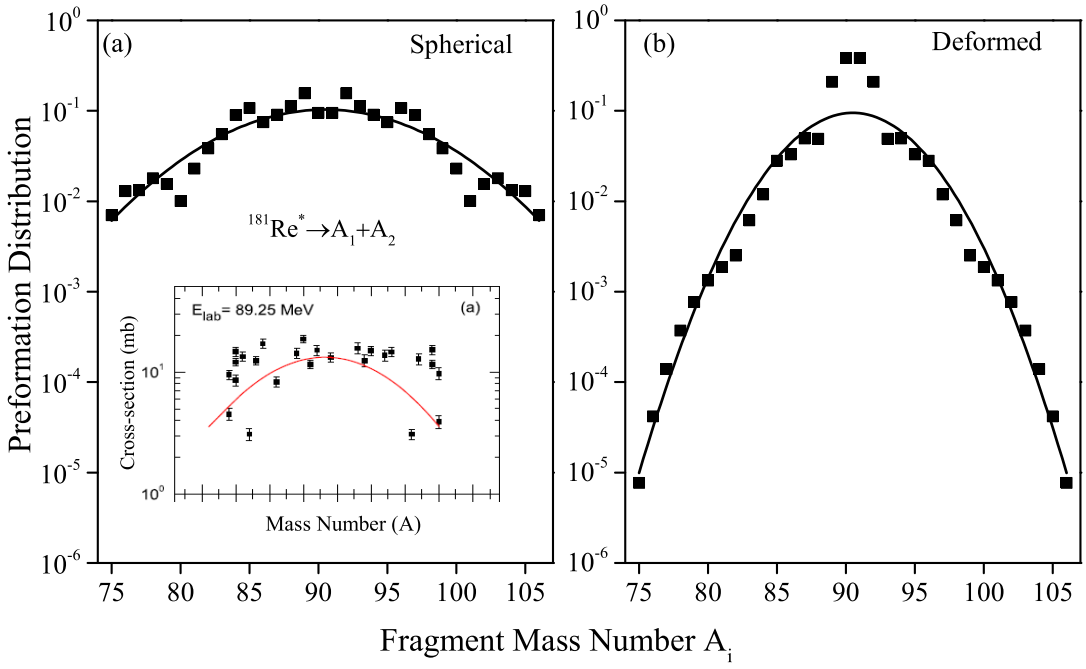

Figure 6.2 Preformation distributions plotted for different masses of fission fragments at the highest energy E^*_{CN} for (a) spherical and (b) deformed approaches. The experimental cross-sectional distribution is also shown as inset of panel (a) taken from [3].

tion probability P_0, therefore, an attempt has been made to compare the DCM evaluated preformation distribution with the available experimental cross-section distribution.

The role of spherical vs deformed fragmentation can be further investigated in terms of preformation probability P_0 as shown in Fig. 6.2. This figure exhibits the mass distribution of fission fragments with respect to mass number of outgoing fission fragment at ℓ_{max}-value for the E_{Lab}=89.25 MeV. Since, for both the spherical and deformed approaches of fragmentation, fragments contributing in the fission process are considered in mass range $A_2\sim$74-91 (see Fig. 6.1), thus the mass distribution of these fragments is shown in Fig. 6.2. The figure clearly reveals that the difference between the two choices of fragmentation lies in the nature of the gaussian curve obtained by fitting the mass distributions of fission fragments decaying from parent system $^{181}Re^*$. The spherical approach exhibits the bell curve that is broad and flat, on the other hand, a narrow and tall bell curve is obtained for the deformed approach of fragments. The experimental cross-sectional distribution [3] is plotted as inset of Fig. 6.2 (a). As the calculated prefor-

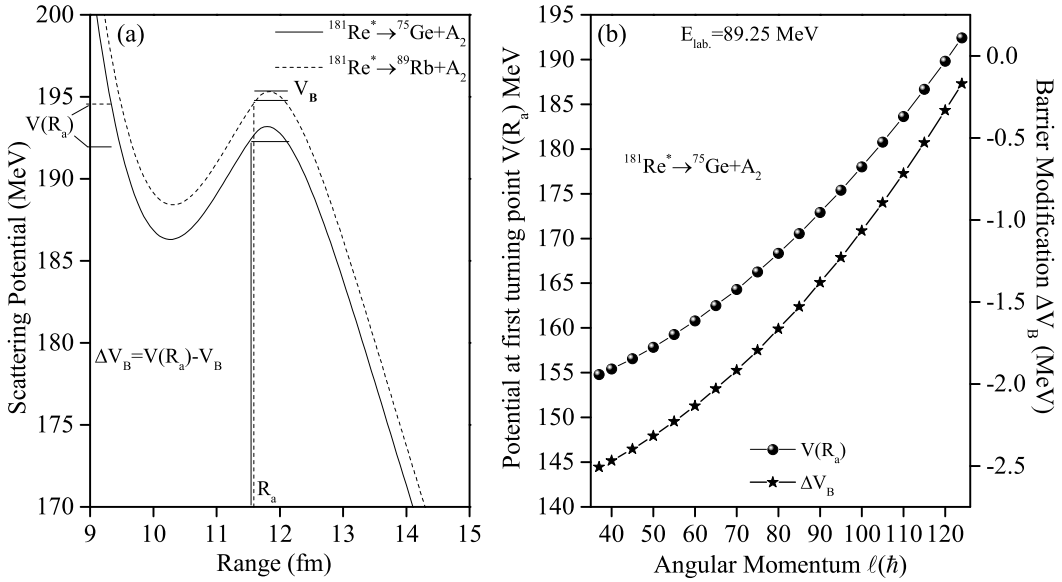

Figure 6.3 (a) Scattering potential plotted as a function of range R for two outgoing channels- asymmetric (^{75}Ge+^{106}Tc) and symmetric (^{89}Rb+^{92}Sr) at the highest energy and $\ell_{max.}$ value. (b) Variation of V(R_a) (left panel) and ΔV_B (right panel) with the change in angular momentum value at $E_{Lab.}$=89.25 MeV for ^{181}Re$^{*}\rightarrow^{75}$Ge+^{106}Tc outgoing channel.

mation distribution for spherical fragmentation seems to follow the experimental trend, so further calculations are executed for spherical choice of fragmentation only. Besides the structure of the mass distribution curve, the fission fragments emitting from ^{181}Re* are also identified with respect to the available data [3]. Most of the outgoing fission fragments (depicted in Table 6.2 later) are found to be same as the ones identified in experiment [3].

After exploring the P_0, the behavior of penetration probability P is also explored. To calculate P within DCM, scattering potential (V=V_P+V_C+V_ℓ) is calculated and is used as an input to compute the penetrability using WKB approximation. In the next figure 6.3, scattering potential is plotted as a function of internuclear distance at the beam energy E_{Lab}=89.25 MeV for the two outgoing channels i.e. ^{181}Re$^{*}\rightarrow^{75}$Ge+A_2 (asymmetric) and ^{181}Re$^{*}\rightarrow^{89}$Rb+A_2 (symmetric) at ℓ_{max} value. Fig. 6.3(a) shows the penetration paths for the two selected outgoing channels along with their corresponding potentials at first turning points (V(R_a)). The barrier height V_B in case of symmetric channel is higher than

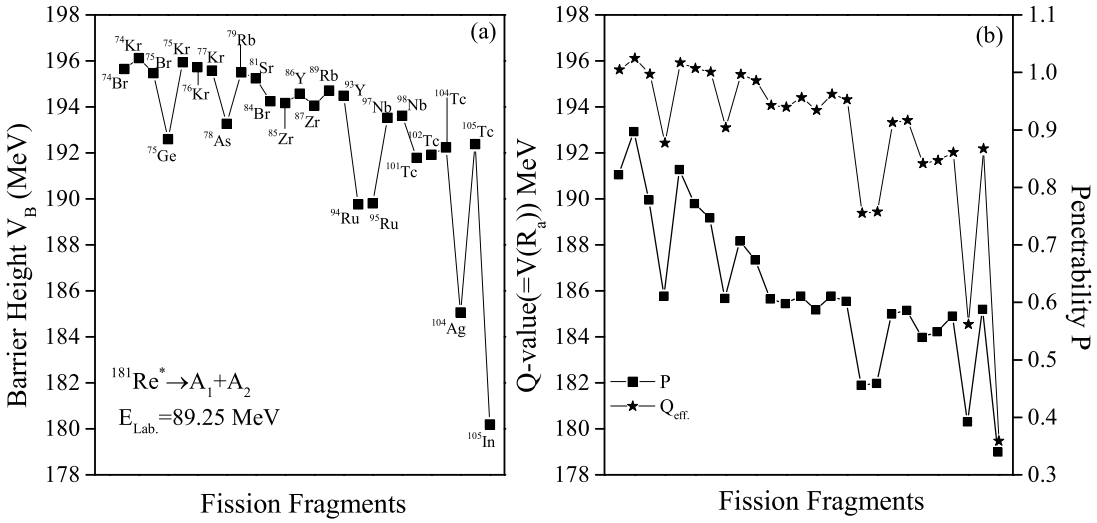

Figure 6.4 (a) Barrier height V_B and (b) $V(R_a)$ (left Y-axis) and penetrability (right Y-axis) plotted at the highest beam energy and $\ell_{max.}$ values for various emitting fission fragments. Note the the fragments in panel (b) are exactly same as marked in panel (a).

that for the asymmetric one. However, the path covered from first (R_a) to second turning point (R_b) for both the channels is almost same i.e. R_b-R_a=0.522fm. Further, Fig. 6.3(b) is plotted to analyze the behavior of potential required to penetrate the barrier i.e. V(R_a) and barrier modification ΔV_B [=V(R_a)-V_B] with respect to angular momentum ℓ for asymmetric channel ^{181}Re$^{*}\rightarrow^{75}$Ge+A_2 at the highest beam energy. The barrier lowering parameter ΔV_B is defined in chapter 2 by Eq. (2.58). It is observed from Fig. 6.3(b) that on increasing the magnitude of angular momentum, the V(R_a) increases for a particular decay channel. On the other hand, ΔV_B decreases (in magnitude) with increase in ℓ-values which means that at the larger ℓ-values, the barrier modification requirement is rather small as compared to that at lower ℓ-values. It is to be reminded here that Fig. 6.1 reveals the dominance of fission at higher angular momentum values. So, in accordance to the above result, it can be said that smaller magnitude of barrier modification is required to have appropriate barrier penetration of fission fragments.

Next, the barrier height V_B is plotted in Fig. 6.4(a) for the various emitting fission channels. As expected, with the change in the fission fragment, barrier height changes.

Table 6.1 DCM calculated total fission cross-sections in (mb) at the given three lab energies for spherical and deformed choices of fragmentation. The respective neck length values and $\ell_{max.}$ numbers are also mentioned in the table.

E_{Lab}	E^*_{CN}	Temp.	ΔR (fm)		ℓ_{max} ($\hbar$)		$\sigma_{fiss.}$ (mb)		
(MeV)	(MeV)	(MeV)	Sph.	β_2	Sph.	β_2	Sph.	β_2	Expt. [3]
77.18	57.14	1.710	1.149	1.27	122	111	179	178	178.9
83.22	62.78	1.792	1.205	1.30	123	112	264	259	262.1
89.25	68.41	1.869	1.225	1.315	124	113	301	300	304.1

The behavior of barrier heights shown in this figure depends primarily on the mass number and atomic number of the decaying fragments. As an instance, there are 3 isobars for A=75 i.e. ^{75}Ge, ^{75}Br and ^{75}Kr, due to the difference in their atomic numbers, the Coulomb potential changes and V_B gets accordingly modified. Next, with the help of above mentioned barrier parameters, penetration probability P along with the Q-value of the various emitting fragments (same as marked in Fig. 6.4), is calculated and plotted in Fig. 6.4(b).

Since smaller Q-value must indicate relative decrease in penetration probability, the same result is observed here also. It is clear that the penetration probability follows the trend of barrier height and Q_{eff}-value of the fission fragments. The penetrability corresponding to ^{105}In is lowest since it is possessing the lowest barrier height (from Fig. 6.4(a)) among all the decaying fragments. This observation implies that Q-value of emitting fragment plays an essential role in deciding the fragmentation behavior of compound nucleus. To analyze the non-uniform behavior of barrier height and penetrability obtained in Fig. 6.4, the mass and charge dependence on V_B is explored in Fig. 6.5. This figure shows that the irregularity in the penetrability pattern is due to the combined effect of A and Z of the emitting fragment. It is seen that the barrier height decreases on increasing the mass of Kr which might be due to the proximity and centrifugal potential that basically depend

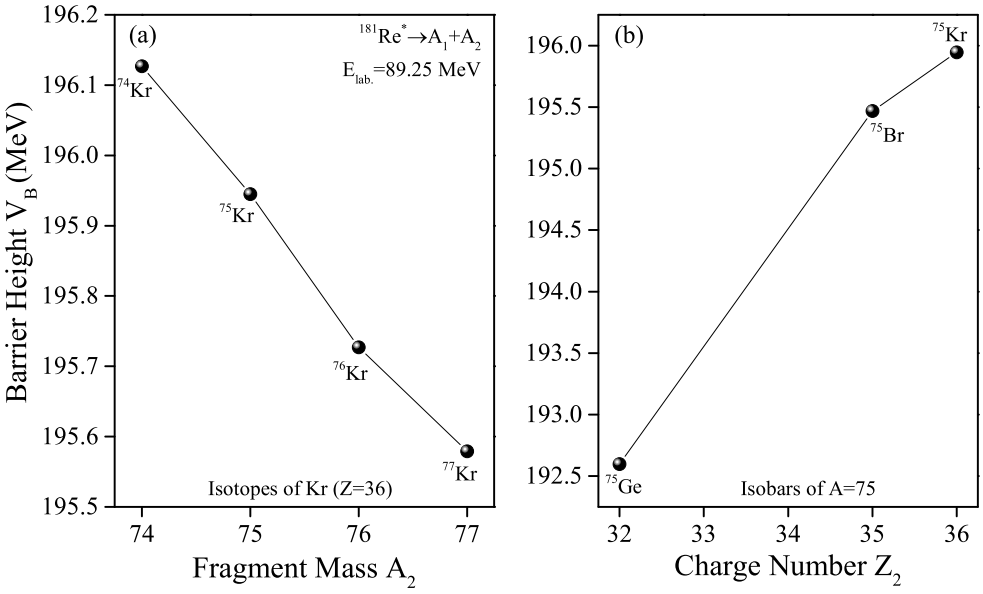

Figure 6.5 Barrier height V_B plotted as a function of (a) fragment mass number for various isotopes of Kr (Z=36) and (b) charge number for various isobars of A=75.

on the mass of the nucleus. On the other hand, right panel of Fig. 6.5 indicates that barrier height increases with the charge number which clearly reveals the role of Coulomb potential in the present work. Same result has been obtained for penetrability (not shown here). Therefore, due to the combined effect of isotopes (mass dependence) and isobars (charge dependence) studied in above figure, a non-uniform pattern of barrier height and the corresponding penetrability of the fission fragments is observed in Fig. 6.4.

After investigating the behavior of P_0 and P, the total fission cross-sections $\sigma_{fiss.}$ have been evaluated. The calculations are performed for the three beam energies i.e. E_{Lab}=77.18, 83.22 and 89.25 MeV upto their respective ℓ_{max} values using both spherical and deformed approaches of fragmentation. Table 6.1 displays the σ_{fiss} values along with their respective neck parameters ΔR, optimized with respect to observed available data [3]. It is clear that the DCM calculated total fission cross sections find nice comparison with the experimental cross-sections [3] for spherical as well as deformed approaches of fragmentation.

Finally, the decay constant λ or fission emission time τ_f is calculated, which in turn provides the useful information on emergence of fission fragments. It is relevant to mention

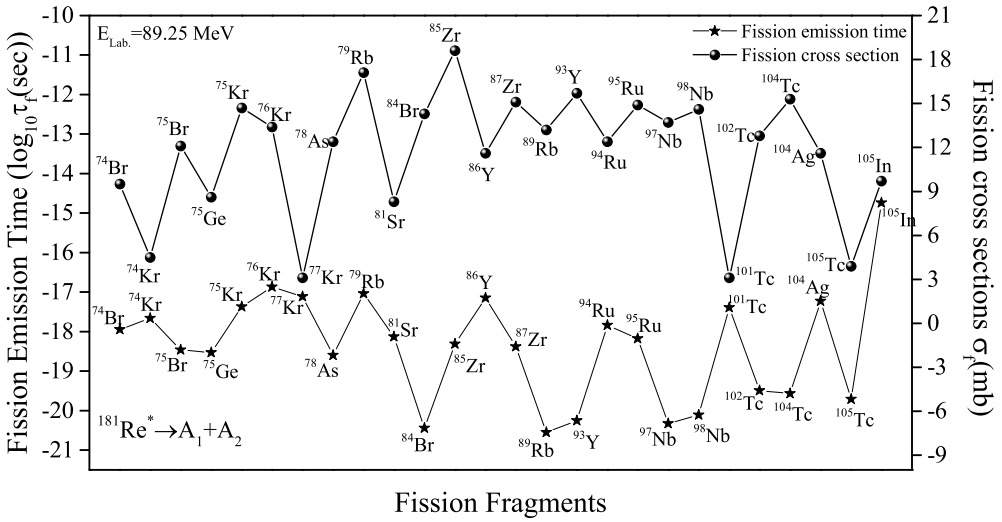

Figure 6.6 The DCM predicted fission emission times (left y-axis) calculated at $E_{lab.}$=89.25 MeV for all the identified fission fragments ranging from A=74-105. The τ_f behavior is also compared with the experimental cross-sectional curve (right y-axis).

here that within DCM, λ comprises of three quantities viz. preformation probability P_0, penetrability P and impinging frequency ν_0. Using P_0, P and ν_0, decay constant and consequently fission emission times of the various probable emitting fragments are calculated at the highest energy E_{Lab}=89.25 MeV for the fixed value of ΔR (1.225 fm) as mentioned in Table 6.1. Fig. 6.6 represents the predicted τ_f values along with the individual fission fragment cross-sections taken from the experimental data [3]. It can be noticed that the fission times are in the range of 10^{-21} to 10^{-17} seconds which is in accordance with previous studies [7–10]. Additionally, it is to be noticed that the behavior of experimental cross-sections of different fragments plotted in the same figure (right y-axis) is exactly opposite to that of the fission times baring few exceptions such as ^{105}In (probably due to the exceptionally low barrier height of ^{105}In in comparison to other fission fragments). This result suggests that DCM provides reasonable estimates of heavy ion induced fission emission time. Similar behavior is observed at two lower energies (not shown here to avoid repetition).

The predicted fission emission times of 34 fission fragments at all the lab energies are displayed in Table 6.2. It is to be noted that these 34 fragments include all the 26

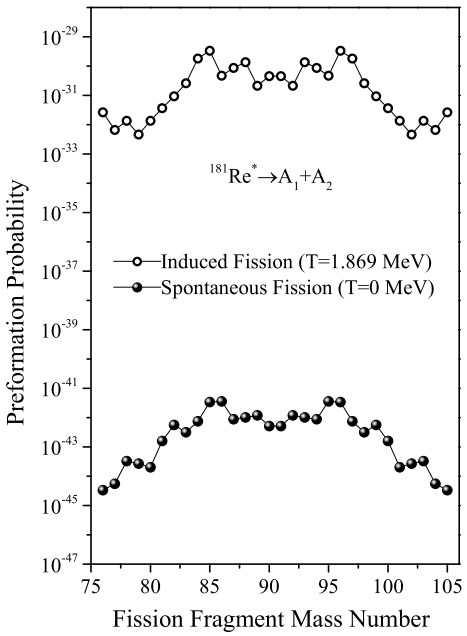

Figure 6.7 Comparison of spontaneous and induced fission of ^{181}Re in terms of preformation distribution. Note that induced fission here corresponds to E_{Lab}=89.25 MeV.

fragments identified experimentally [3] and the additional ones which find comparable contributions in DCM analysis. It is observed that τ_f values lie in the range 10^{-21} to 10^{-17} seconds which gives an useful input for future experiments. It is also noted that the emission time decreases as we increase the beam energy and this result is consistent for all the identified fission fragments. Furthermore, the comparison of induced fission dynamics is made with spontaneous fission of ^{181}Re nucleus, in terms of preformation probability distribution at lowest value of angular momentum at the highest beam energy as shown in Fig. 6.7. It is clear that for both the spontaneous and induced fission of ^{181}Re, the mass distribution is found to be almost similar, although a large variation in their respective magnitudes is observed. This result is in accordance with our work [20] on spontaneous and induced fission of ^{244}Pu which concludes that the structural profile remains similar when one moves from ground state to excited state fission dynamics. The detailed discussion on the same is presented in the next subsection.

Table 6.2 The fission emission times and decay widths predicted within DCM at the three given lab energies for all the identified fission fragments.

Sr. No.	Fission Fragment	Fission Emission Time τ_f (s)			Decay Width Γ (MeV)		
		E_{Lab}=77.18 MeV	E_{Lab}=83.22 MeV	E_{Lab}=89.25 MeV	E_{Lab}=77.18 MeV	E_{Lab}=83.22 MeV	E_{Lab}=89.25 MeV
		ΔR=1.15 fm	ΔR=1.205 fm	ΔR=1.225 fm	ΔR=1.15 fm	ΔR=1.205 fm	ΔR=1.225 fm
1.	^{74}Br	$3.55\text{x}10^{-18}$	$1.78\text{x}10^{-18}$	$1.12\text{x}10^{-18}$	$1.29\text{x}10^{-4}$	$2.56\text{x}10^{-4}$	$4.06\text{x}10^{-4}$
2.	^{74}Kr	$7.24\text{x}10^{-18}$	$4.79\text{x}10^{-18}$	$2.19\text{x}10^{-18}$	$6.29\text{x}10^{-5}$	$9.53\text{x}10^{-5}$	$2.08\text{x}10^{-4}$
3.	^{75}Br	$1.00\text{x}10^{-18}$	$5.50\text{x}10^{-19}$	$3.47\text{x}10^{-19}$	$4.56\text{x}10^{-4}$	$8.30\text{x}10^{-4}$	$1.32\text{x}10^{-3}$
4.	^{75}Ge	$7.76\text{x}10^{-19}$	$5.89\text{x}10^{-19}$	$2.95\text{x}10^{-19}$	$5.87\text{x}10^{-4}$	$7.74\text{x}10^{-4}$	$1.55\text{x}10^{-3}$
5.	^{75}Kr	$2.34\text{x}10^{-17}$	$1.10\text{x}10^{-17}$	$4.27\text{x}10^{-18}$	$1.95\text{x}10^{-5}$	$4.16\text{x}10^{-5}$	$1.07\text{x}10^{-4}$
6.	^{76}Kr	$3.89\text{x}10^{-17}$	$2.82\text{x}10^{-17}$	$1.35\text{x}10^{-17}$	$1.17\text{x}10^{-5}$	$1.62\text{x}10^{-5}$	$3.38\text{x}10^{-5}$
7.	^{77}Kr	$1.86\text{x}10^{-17}$	$1.35\text{x}10^{-17}$	$7.76\text{x}10^{-18}$	$2.45\text{x}10^{-5}$	$3.38\text{x}10^{-5}$	$5.87\text{x}10^{-5}$
8.	^{78}As	$5.25\text{x}10^{-19}$	$3.98\text{x}10^{-19}$	$2.51\text{x}10^{-19}$	$8.69\text{x}10^{-4}$	$1.15\text{x}10^{-3}$	$1.82\text{x}10^{-3}$
9.	^{79}Rb	$1.91\text{x}10^{-17}$	$1.48\text{x}10^{-17}$	$9.12\text{x}10^{-18}$	$2.39\text{x}10^{-5}$	$3.08\text{x}10^{-5}$	$5.00\text{x}10^{-5}$
10.	^{80}As	$3.78\text{x}10^{-20}$	$2.92\text{x}10^{-20}$	$1.85\text{x}10^{-20}$	$1.20\text{x}10^{-2}$	$1.92\text{x}10^{-2}$	$2.45\text{x}10^{-2}$
11.	^{81}Se	$2.76\text{x}10^{-20}$	$1.69\text{x}10^{-20}$	$1.27\text{x}10^{-20}$	$1.65\text{x}10^{-2}$	$2.69\text{x}10^{-2}$	$3.57\text{x}10^{-2}$
12.	^{81}Sr	$1.70\text{x}10^{-18}$	$1.02\text{x}10^{-18}$	$7.41\text{x}10^{-19}$	$2.69\text{x}10^{-4}$	$4.46\text{x}10^{-4}$	$6.15\text{x}10^{-4}$
13.	^{82}Se	$1.94\text{x}10^{-20}$	$1.20\text{x}10^{-20}$	$9.20\text{x}10^{-21}$	$2.34\text{x}10^{-2}$	$3.77\text{x}10^{-2}$	$4.95\text{x}10^{-2}$
14.	^{83}Br	$1.32\text{x}10^{-20}$	$8.35\text{x}10^{-21}$	$6.40\text{x}10^{-21}$	$3.43\text{x}10^{-2}$	$5.45\text{x}10^{-2}$	$7.11\text{x}10^{-2}$
15.	^{84}Br	$7.41\text{x}10^{-21}$	$4.68\text{x}10^{-21}$	$3.63\text{x}10^{-21}$	$6.15\text{x}10^{-2}$	$9.75\text{x}10^{-2}$	$1.26\text{x}10^{-1}$
16.	^{85}Br	$6.45\text{x}10^{-21}$	$4.35\text{x}10^{-21}$	$3.57\text{x}10^{-21}$	$7.04\text{x}10^{-2}$	$1.05\text{x}10^{-1}$	$1.27\text{x}10^{-1}$
17.	^{85}Zr	$9.77\text{x}10^{-19}$	$6.31\text{x}10^{-19}$	$4.90\text{x}10^{-19}$	$4.67\text{x}10^{-4}$	$7.23\text{x}10^{-4}$	$9.31\text{x}10^{-4}$
18.	^{86}Y	$1.45\text{x}10^{-17}$	$8.91\text{x}10^{-18}$	$7.08\text{x}10^{-18}$	$3.15\text{x}10^{-5}$	$5.12\text{x}10^{-5}$	$6.44\text{x}10^{-5}$
19.	^{87}Kr	$9.34\text{x}10^{-21}$	$6.09\text{x}10^{-21}$	$4.86\text{x}10^{-21}$	$4.88\text{x}10^{-2}$	$7.44\text{x}10^{-2}$	$9.34\text{x}10^{-2}$
20.	^{87}Zr	$8.32\text{x}10^{-19}$	$5.13\text{x}10^{-19}$	$4.17\text{x}10^{-19}$	$5.48\text{x}10^{-4}$	$8.89\text{x}10^{-4}$	$1.09\text{x}10^{-3}$
21.	^{88}Rb	$9.22\text{x}10^{-21}$	$6.01\text{x}10^{-21}$	$4.79\text{x}10^{-21}$	$4.94\text{x}10^{-2}$	$7.57\text{x}10^{-2}$	$9.48\text{x}10^{-2}$
22.	^{89}Rb	$5.25\text{x}10^{-21}$	$3.47\text{x}10^{-21}$	$2.82\text{x}10^{-21}$	$8.69\text{x}10^{-2}$	$1.32\text{x}10^{-1}$	$1.62\text{x}10^{-1}$
23.	^{90}Rb	$6.34\text{x}10^{-21}$	$4.11\text{x}10^{-21}$	$3.22\text{x}10^{-21}$	$7.17\text{x}10^{-2}$	$1.11\text{x}10^{-1}$	$1.41\text{x}10^{-1}$
24.	^{93}Y	$1.12\text{x}10^{-20}$	$6.92\text{x}10^{-21}$	$5.62\text{x}10^{-21}$	$4.06\text{x}10^{-2}$	$6.59\text{x}10^{-2}$	$8.11\text{x}10^{-2}$
25.	^{94}Ru	$2.75\text{x}10^{-18}$	$1.78\text{x}10^{-18}$	$1.45\text{x}10^{-18}$	$1.66\text{x}10^{-4}$	$2.56\text{x}10^{-4}$	$3.15\text{x}10^{-4}$
26.	^{95}Ru	$1.12\text{x}10^{-18}$	$7.59\text{x}10^{-19}$	$6.61\text{x}10^{-19}$	$4.06\text{x}10^{-4}$	$6.01\text{x}10^{-4}$	$6.90\text{x}10^{-4}$
27.	^{97}Nb	$8.32\text{x}10^{-21}$	$5.62\text{x}10^{-21}$	$4.68\text{x}10^{-21}$	$5.48\text{x}10^{-2}$	$8.11\text{x}10^{-2}$	$9.75\text{x}10^{-2}$
28.	^{98}Nb	$1.58\text{x}10^{-20}$	$1.02\text{x}10^{-20}$	$7.76\text{x}10^{-21}$	$2.88\text{x}10^{-2}$	$4.46\text{x}10^{-2}$	$5.87\text{x}10^{-2}$
29.	^{101}Tc	$7.24\text{x}10^{-18}$	$5.50\text{x}10^{-18}$	$4.07\text{x}10^{-18}$	$6.29\text{x}10^{-5}$	$8.30\text{x}10^{-5}$	$1.12\text{x}10^{-4}$
30.	^{102}Tc	$7.94\text{x}10^{-20}$	$4.79\text{x}10^{-20}$	$3.24\text{x}10^{-20}$	$5.74\text{x}10^{-3}$	$9.53\text{x}10^{-3}$	$1.41\text{x}10^{-2}$
31.	^{104}Tc	$6.03\text{x}10^{-20}$	$3.80\text{x}10^{-20}$	$2.69\text{x}10^{-20}$	$7.57\text{x}10^{-3}$	$1.20\text{x}10^{-2}$	$1.69\text{x}10^{-2}$
32.	^{104}Ag	$1.17\text{x}10^{-17}$	$6.92\text{x}10^{-18}$	$5.89\text{x}10^{-18}$	$3.88\text{x}10^{-5}$	$6.59\text{x}10^{-5}$	$7.74\text{x}10^{-5}$
33.	^{105}Tc	$4.79\text{x}10^{-20}$	$2.82\text{x}10^{-20}$	$1.95\text{x}10^{-20}$	$9.53\text{x}10^{-3}$	$1.62\text{x}10^{-2}$	$2.34\text{x}10^{-2}$
34.	^{105}In	$4.07\text{x}10^{-15}$	$2.24\text{x}10^{-15}$	$1.82\text{x}10^{-15}$	$1.12\text{x}10^{-7}$	$2.04\text{x}10^{-7}$	$2.51\text{x}10^{-7}$

6.2.2 Decay of Plutonium isotopes via spontaneous and induced fission

In this section, first the dynamics of an excited compound nucleus ^{244}Pu* is analyzed within the methodology of the DCM to explore the behavior of heavy-ion induced reactions. The fission cross-sections are extracted for a broad range of center of mass energy varying from $E_{c.m.}$=15.0-28.8 MeV by using different neck-length parameters. Note that ΔR is the only parameter of the model, that decides the entry point of barrier penetration as well as the fragment's preformation. The calculations are done for spherical and the quadrupole (β_{2i}) deformed choice of fragmentation.

Based on the availability of experimental data on spontaneous fission of Pu, the half-lives of experimentally observed spontaneous decays of $^{236-244}$Pu nuclei are calculated, using the PCM. Here, the energetically favored fragments in the decay channel are identified for $^{236-244}$Pu parents and their behavior in context of the preformation probability P_0, penetrability P and decay barrier heights is studied. Then, by extrapolating the neck-length parameters, optimized in view of experimental data of $^{236-244}$Pu parents, the half-lives of ^{234}Pu and ^{246}Pu are estimated. Finally, the comparative study of induced versus spontaneous fission process is investigated in terms of potential energy surfaces and barrier modification effects.

First of all, to explore the dynamics of heavy-ion induced fission process, the Dynamical Cluster-decay Model (DCM) has been implemented to analyze the decay pattern of excited ^{244}Pu* compound nuclear system produced in ^{6}He+^{238}U reaction. The calculations are done at five different excitation energies ranging from E^{*}=20.53-34.33 MeV. Using β_{2i}-deformed shapes, the DCM evaluated fission cross-sections at all reported energies find nice agreement (see Table 6.3) with the respective experimental data [21] over a range of neck values. However, the spherical choice of decay fragments fail to reproduce the experimental data at the higher energies. In addition, an attempt has also been made to investigate the contribution of light-particle cross sections σ_{LPs}, which is found to be

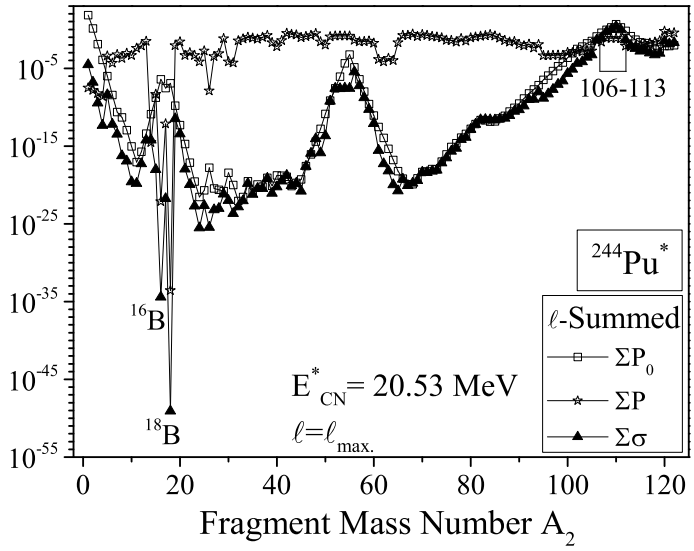

Figure 6.8 Decay cross section σ, penetration probability P and preformation probability P_0, summed over ℓ, plotted as a function of light mass fragments for the compound nucleus ^{244}Pu* formed in the ^{6}He+^{238}U reaction for deformed choice of fragments having "hot compact" configurations.

negligibly small ($\sim 10^{-5}$ barns) at all energies. Apparently, as expected of a radioactive nucleus, σ_{fiss} is the main contributor towards the total decay cross section.

Now, knowing that σ exhibits a combined effect of both P_0 and P, Fig. 6.8 shows the ℓ-summed preformation probability P_0, penetrability P and cross section σ with summation up to $\ell = \ell_{max}$, as a function of the light-mass fragment A_2 at the lowest E^*_{CN}=20.53 MeV (T= 0.889 MeV). It is evident from this figure that (i) σ follows the behavior of P_0, which means that structure effects are contained only in P_0; (ii) P contributes largely to magnitude and has almost no structure effects; (iii) the strongly formed fragments ^{16}B and ^{18}B are shown to have very small P values, and hence their preferential decay get counter balanced by P, which means their contribution to cross section is negligible. Interestingly, the reported fission cross sections correspond to asymmetric fission ($A_{CN}/2 \pm 20$), and hence the fragments in the mass range A_2=106-113 (plus their complementary heavy fragments) seem to contribute towards fission cross sections over a wide range of incident energy. Note that no individual fragments have been identified in the measurements [21].

Next, an attempt has been made to address the available SF half-lives in reference

Table 6.3 The fission cross sections for the decay of ^{244}Pu* formed in a heavy-ion induced reaction, calculated within the DCM at different neck-length parameters ΔR for deformations up to quadrupole β_{2i} alone, at different $E_{c.m.}$ values, compared with the experimental data [21]. Here, the angular momentum ℓ_{max} varies from 131$\hbar$ to 142$\hbar$. Note that, here, the contributing fission region lies between A_2=106-113.

E^*_{CN} (MeV)	T (MeV)	ΔR (fm)	$\sigma_{fission}$ (mb)	
			DCM	Expt.
20.53	0.889	0.892	10.18	10.241
23.03	0.940	0.925	19.50	20.188
27.03	1.017	1.085	197.40	199.255
32.83	1.118	1.210	812.00	821.740
34.33	1.144	1.232	1116.00	1127.020

to $^{236-244}$Pu parent nuclei, by optimizing ΔR within PCM, considering spherical and β_2 deformed fragments. The scattering potential in Fig. 6.9 shows that the barrier characteristics, i.e., barrier height V_B and position R_B get changed significantly after the incorporation of deformations and orientations of the fission fragments, thereby influencing the barrier penetrability P. The choice of the most probable outgoing fragment is based on the minimum in fragmentation potential and thus on the maxima in preformation probability P_0. Note that in PCM, the calculated decay constant λ (or half-life $T_{1/2}$) depends upon both the barrier penetrability and preformation factor, further on the inclusion or non-inclusion (spherical nuclei) of deformation and orientation degrees-of-freedom.

Fig. 6.9 depicts the three steps of barrier tunnelling in PCM with the calculations performed at separation distance (range), starting with the entrance point R_a=R_t+ΔR of the penetration path. The only parameter ΔR of the model is obtained for the best achievable fit of the observed SF decay half-lives data [22, 23]. Note that the orientations are uniquely fixed on the basis of the signs (+ or -) of β_{2i} alone which manifests in the form of 'hot compact' or 'cold elongated' configurations (see Table 1 in [24]). In view

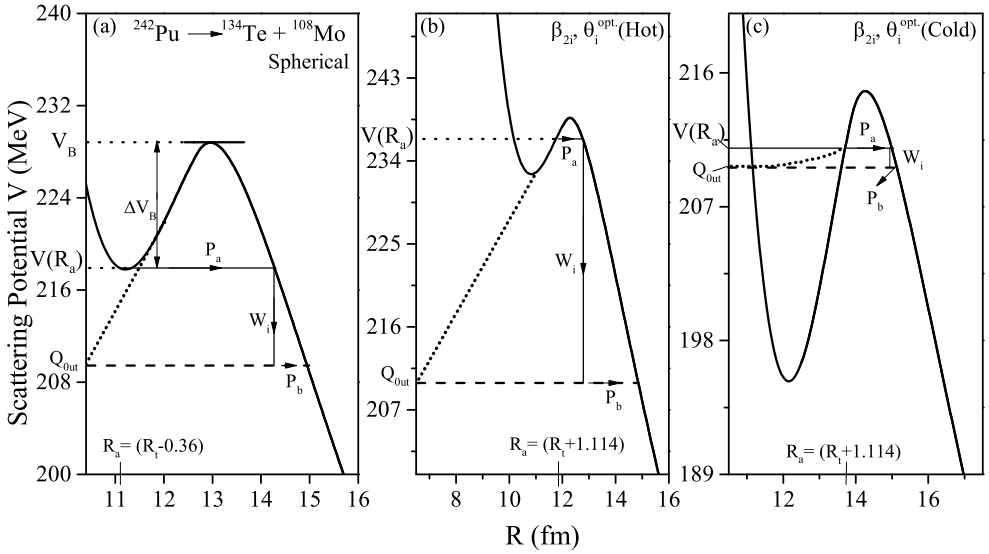

Figure 6.9 Scattering potentials for the spontaneous decay of ^{242}Pu→^{134}Te+^{108}Mo, showing the three steps of barrier penetration, with both the fragments taken as (a) spherical, (b) deformed nuclei with quadrupole deformations β_{2i} alone having optimum "hot" and (c) optimum "cold" orientations $\theta_i^{opt.}$ of Table 1 of Gupta *et al.* in Ref. [24]. The deformations, kept fixed, are included by using the tables of Möller *et al.* [25]. The dotted lines joining the Q-value to V(R) in the neighborhood of $R = R_t$ represent the polynomial of degree two in R for both the spherical and deformed cases.

of this, the comparative behavior of hot compact and cold elongated configurations is presented in Figs. 6.9 (b) and 6.9 (c). The 'hot compact' configuration corresponds to smallest interaction radius and highest barrier, whereas the 'cold elongated or non-compact' corresponds to largest interaction radius and lowest interaction barrier [24].

First of all, it is important to check that the potential $V(R_a)$, corresponding to first turning point R_a, should be greater than the Q_{out} value for the penetration of the barrier to occur. Fig. 6.10 reveals the comparison of the difference $V(R_a) - Q$, of potentials $V(R_a)$ at entrance point and Q-values calculated by using the binding energies of Möller *et al.* [25], as a function of mass number of Pu parent nucleus, at fixed R_a=R_t (filled square) and R_a=R_t+1.114 fm (open squares), for both the "hot compact" and "cold elongated" configurations. It is noticed that for both the choices of ΔR (=0 and 1.114 fm), the difference comes out to be positive in case of 'hot' configuration. For 'cold elongated' considerations, however, in case of ΔR=0, the touching configuration, Fig. 6.10 (b) depicts clearly that the value of potential $V(R_a)$ is lesser than Q-value of the

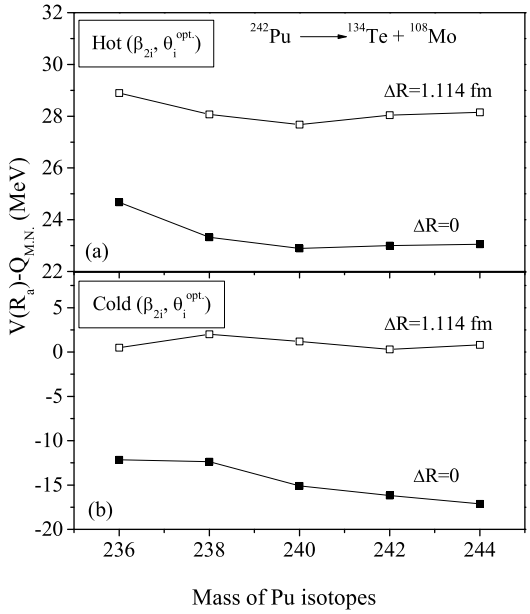

Figure 6.10 (a) Difference of the potential $V(R_a)$ at the first turning point R_a and the Q-value calculated from binding energies [25] is plotted as a function of the mass number of parent nuclei for $\ell = 0\hbar$ case at different first turning points, i.e., at R_a=R_t (filled squares) and R_a=R_t+1.114 fm (open squares) (a)"hot compact" and (b) "cold elongated" configuration.

decay, for $^{236-244}$Pu nuclear systems investigated here. Note that although the situation corresponding to 'cold' choice improves significantly at $R_a \geq R_t$+1.114, but then the PCM calculated half-lives are found to overestimate the available SF data. In other words, the comparison of PCM calculations comes out to be better with spherical and optimum 'hot' choice of configurations which was considered to address the induced fission of ^{244}Pu* previously. The standard RMS deviation from experimental data is also evaluated which is found to be minimum (~ 0.22) for spherical fragments, and 3.36 and 35.72, respectively, for 'hot' and 'cold' configurations. Therefore, one may conclude that 'cold elongated' consideration is certainly not the best option to study the spontaneous decays specially in the fission region, or, in other words, the spherical or 'hot compact' configurations of the "optimum" orientations may be preferred for investigating the SF half-lives, which we do in the following.

The other interesting quantity in the calculation of λ or $T_{1/2}$ is the preformation factor P_0, whose value depends on the fragmentation potential $V(A_2)$, depicted in Fig. 6.11 for the respective ^{236}Pu parent nucleus at ℓ=0 $\hbar$. The definite role of deformations is explored

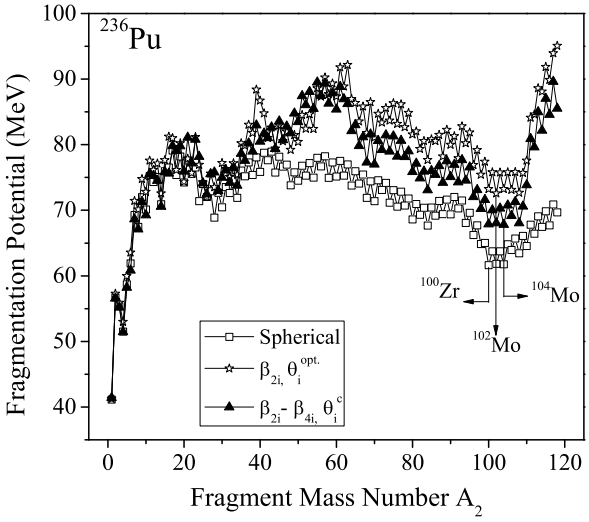

Figure 6.11 Fragmentation potential $V(A_2)$ for the decaying parent nucleus ^{236}Pu, at a fixed value of ΔR (=1.105 fm) and ℓ=0, taking the two fragments as spheres, with β_{2i} alone and (β_{2i}, β_{3i}, β_{4i}) deformations with appropriate orientations.

here and the calculations are made considering the spherical approach, quadrupole deformed (β_{2i} alone) as well as higher multipole (β_{2i}-β_{4i}) deformed approach of fragments. It is to be noticed here that "compact" orientations θ_i^c [26] have been used, instead of "optimum", for investigating the role of higher multipole deformations up to hexadecapole (β_{4i}). Note that the neck parameter is taken same (=1.105 fm) for all the three cases, so as to analyze the exclusive role of deformations, chosen in reference to fitted ΔR value for β_2 deformed case, although the measured decay half-life [$log_{10}T_{1/2}$(s)=16.67] for the spontaneous decay of ^{236}Pu is attained at ΔR=-0.15, 1.105 and 1.10 fm, respectively, for spherical, β_{2i} deformed and β_2-β_4 deformed choice of fragments. It is observed in Fig. 6.11 that, although the magnitudes of fragmentation potential are different, the pattern of potential energy surfaces (PES) is similar for all the three choices of shapes of fragments. Interesting enough, spherical considerations seem to be energetically most preferred, specifically with reference to fission analysis in a spontaneous decay process. A solid vertical line is marked in Fig. 6.11, to indicate/designate the most probable (energetically most favored) fragment as ^{100}Zr, ^{102}Mo or ^{104}Mo for (a) spherical (b) with β_{2i} alone and (c) with β_{2i}-β_{4i} fragments, respectively. The above result/statement implies that the choice of deformation and orientation effects is a vital input quantity in

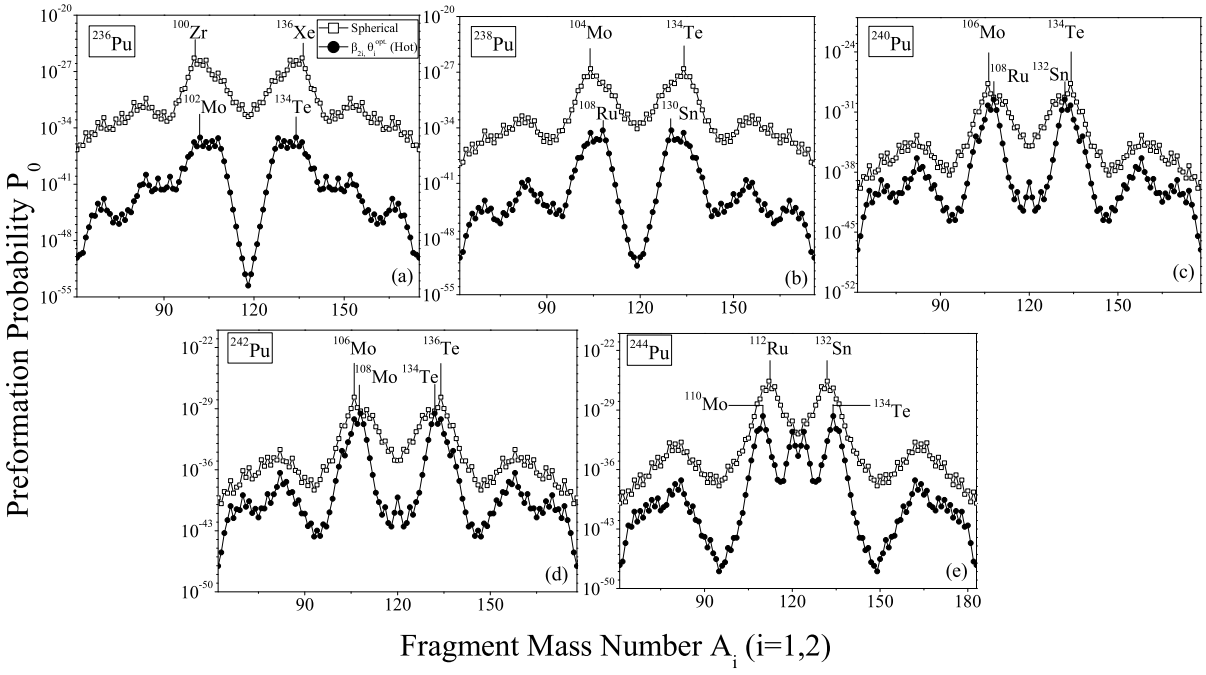

Figure 6.12 Preformation probability P_0 for the decay of (a) ^{236}Pu, (b) ^{238}Pu, (c) ^{240}Pu, (d) ^{242}Pu, and (e) ^{244}Pu parents calculated at the best fitted neck-length values (depicted in Fig. 6.15) for spherical and deformed (up to β_{2i}) choice of fragments, showing the presence of shell effects in all cases.

deciding favorable fragment for the SF process. It may be pointed out here that the reported PCM calculations of SF half-lives here correspond to the choice of most preferred fragments in mass region ∼80-A/2 (and corresponding heavy fragments) for the decay of $^{236-244}$Pu parents, although no such individual fragments have been identified in the reported experiments [22, 23].

The above results are further explored in view of preformation probability P_0 plotted with respect to fragment mass number A_i in Fig. 6.12 (shown for the fission mass region 80-A/2 and the corresponding heavy fragments) for all the five ^{236,238,240,242,244}Pu parents considered in the present study. It is relevant to remind here that P_0 is the probability with which the fragment is preformed before it comes out of the parent nucleus by penetrating the potential barrier. Note that it is a relative quantity, i.e., a slight change in the potential $V(A_2)$ for any one of the fragments leads to redistribution of P_0 among all the fragments. Importantly, a minimum in fragmentation potential corresponds to the maximum in preformation probability and vice versa, illustrated for example for the ^{102}Mo

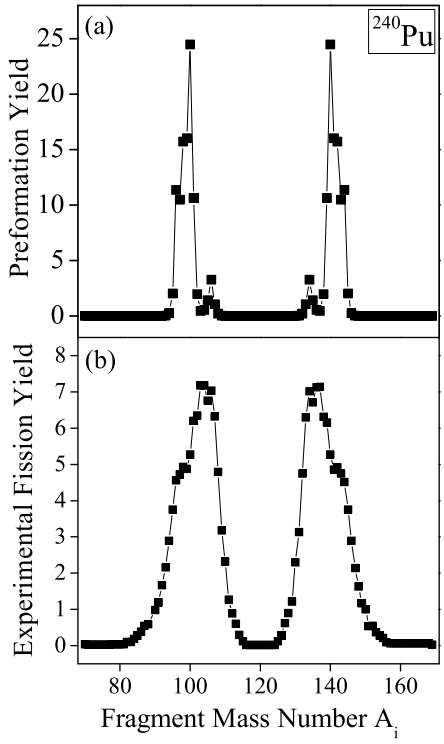

Figure 6.13 Comparison of mass distribution yield (equivalently, preformation probability P_0) with the experimental fission yield for decay of spontaneous fission of ^{240}Pu.

fragment emitted in the fission of ^{236}Pu nucleus in Fig. 6.12 (a). Besides the shift in magnitude, the preformation pattern remains quite similar for all Pu isotopes, regardless of spherical or β_2 deformed choice of fragmentation and specifies asymmetric fission in the heavy mass fragment region. Interestingly, the emergence of most favorable fragment, explicitly marked in terms of strong maxima in P_0, depends on the choice of fragmentation potential and further on the inclusion or non-inclusion of deformation effects. The nuclear shell structural effects are also visible in preformation part, as the magnitude is larger for fragments referring to spherical shell closures around heavy fragment charge Z_1=50 and neutron number N_1=82. This result holds good despite the use of different shape configurations, thereby providing relevant information for overall understanding of SF dynamics of nuclear systems.

Additionally, it will be of great interest to compare with experiments, the calculated mass distribution yields for the spontaneous fission fragments. Since the experimental data on SF distribution is available for ^{240}Pu isotope, so we decided to do corresponding

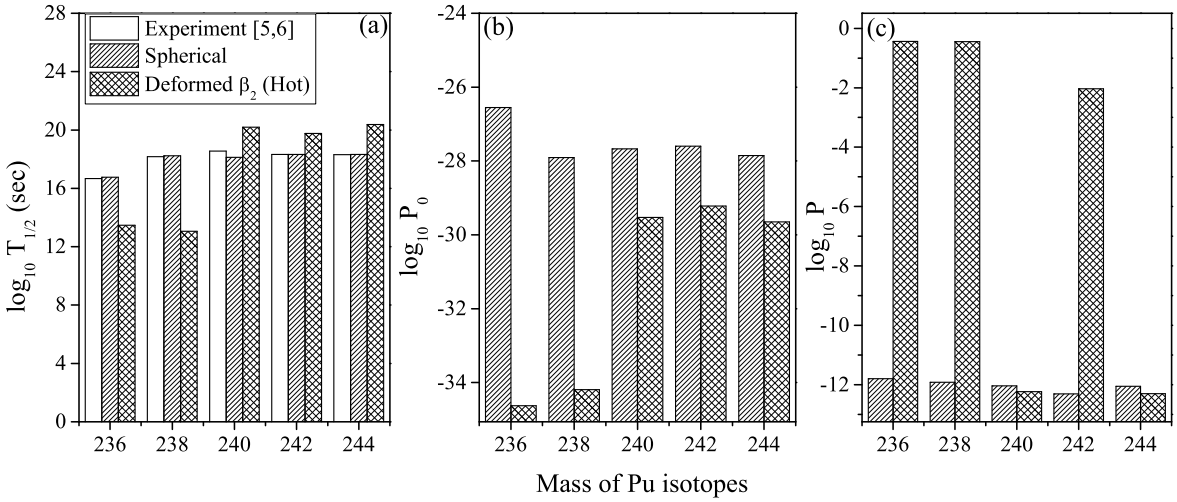

Figure 6.14 The logarithm of (a) decay half-lives (b) preformation and (c) penetration probability for the most preferred fragment in spontaneous decay of even mass $^{236-244}$Pu parents for cases of spherical and β_2 deformed nuclei with optimum "hot" orientations, compared with experimental data.

calculations for this nucleus. As the structural effects are contained mainly in the preformation probability P_0, in Fig. 6.13 we compare our PCM estimated mass yield P_0, with experimental mass yields [27] in reference to spontaneous fission. Interestingly, asymmetric fission mass distribution yield is obtained in Fig. 6.13 (a), which is in agreement with the experimentally measured [27] mass distributions for the SF as depicted in Fig. 6.13 (b).

The calculated P_0, P and $log_{10}T_{1/2}$ are presented in Fig. 6.14 and Table 6.4. One can clearly see that PCM calculations agree nicely with experiments, more so for the spherical case, for all the studied even mass $^{236-244}$Pu parents, which in turn, emphasize the applicability of our formalism for fission analysis of spontaneous decays. This observation signifies that PCM provides reasonable estimation of the most preferred decay fragments in reference to spontaneous decays mechanism, and hence could possibly provides relevant inputs for future measurements on SF. For majority of the parents studied, we observe from Figs. 6.14 (b) and 6.14 (c) that preformation factor P_0 decreases and penetrability P increases while shifting from spherical to deformed approach. Whereas, assault frequency ν_0 remains almost constant ($\sim 10^{21}\ s^{-1}$), independent of choice of deformation

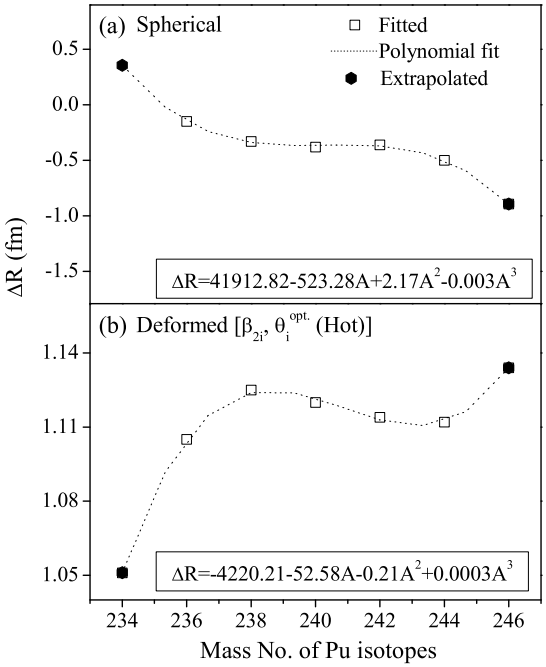

Figure 6.15 Variation of the neck length parameter ΔR with atomic mass number of Pu isotopes obtained for (a) spherical and (b) β_2-deformed decay products. Open symbols are fitted value and filled symbols are extrapolated values via the polynomial fits.

effects. Apparently, as both P_0 and P are affected by the incorporation of deformation and orientation effects, the calculated $T_{1/2}$ or λ-values show significant dependence on deformations and orientation effects.

Note that the PCM calculations are extremely sensitive to the choice of ΔR, which is further found to be a vital parameter in the calculation of decay half-life. Keeping this in mind, an effort has been made in Fig. 6.15 to estimate half-lives of ^{234}Pu and ^{246}Pu isotopes to accomplish a comprehensive analysis of the best preformed fragment and other characteristics quantities in the spontaneous decay of $^{234-246}$Pu parents. In order to estimate the decay half-lives for ^{234,246}Pu nuclei, the fitted ΔR values of $^{236-244}$Pu nuclei are extrapolated via a polynomial fitting. Fig. 6.15 shows the extrapolated neck-length values as a function of the mass number of Pu isotopes, with both choices of spherical and deformed treatment of decay products. Here the open symbols show ΔR values for PCM fitted ^{236,238,240,242,244}Pu decay half-lives in reference to experimental data [22, 23] and filled symbols represent extracted ΔR values for ^{234,246}Pu, using the polynomials

Table 6.4 PCM-calculated decay half-lives along with the relevant preformation and penetration quantities for the spontaneous fission of even $^{234-246}$Pu isotopes for both spherical as well as β_2 deformed nuclei. The choice of most probable fragment is decided on the basis of preformation factor, in accordance with Fig. 6.12. The measured decay half-lives for $^{236-244}$Pu isotopes are also shown. For ^{234,246}Pu isotopes, the ΔR values are obtained by extrapolation in reference to Fig. 6.15.

Parent nucleus	Decay channel	$\triangle R$ (fm)	$\triangle V_B$ (MeV)	$log_{10}P_0$	$log_{10}P$	$log_{10}T_{1/2}$ (sec)	
						DCM	Expt.
			Spherical				
^{234}Pu	^{98}Zr+^{136}Xe	0.356	-8.062	-23.15	-9.44	10.99	-
^{236}Pu	^{100}Zr+^{136}Xe	-0.150	-10.557	-26.55	-11.80	16.76	16.67
^{238}Pu	^{104}Mo+^{134}Te	-0.330	-10.500	-27.91	-11.92	18.24	18.17
^{240}Pu	^{106}Mo+^{134}Te	-0.360	-10.549	-27.67	-12.04	18.13	18.56
^{242}Pu	^{106}Mo+^{136}Te	-0.360	-10.707	-27.60	-12.31	18.32	18.32
^{244}Pu	^{112}Ru+^{132}Sn	-0.500	-10.261	-27.85	-12.05	18.32	18.31
^{246}Pu	^{114}Ru+^{132}Sn	-0.894	-6.285	-33.13	-11.06	22.62	-
			β_2-Deformed (Hot)				
^{234}Pu	^{100}Mo+^{134}Te	1.051	-1.304	-33.06	-11.71	23.17	-
^{236}Pu	^{102}Mo+^{134}Te	1.105	-0.486	-34.63	-0.44	13.47	16.67
^{238}Pu	^{108}Ru+^{130}Sn	1.125	-0.494	-34.19	-0.45	13.06	18.17
^{240}Pu	^{108}Ru+^{132}Sn	1.120	-0.563	-29.53	-12.23	20.19	18.56
^{242}Pu	^{108}Mo+^{134}Te	1.114	-0.456	-29.22	-2.03	19.77	18.32
^{244}Pu	^{110}Mo+^{134}Te	1.112	-0.552	-29.65	-12.30	20.38	18.31
^{246}Pu	^{112}Mo+^{134}Te	1.134	-0.687	-30.56	-12.89	21.89	-

$\Delta R^{Sph.}$ = 41912.82-523.28A+2.17A^2-0.003A^3

$\Delta R^{Def.}$ = -4220.21-52.58A-0.21A^2+0.0003A^3

The results so obtained are also given in Table 6.4 for the cases of spherical and β_{2i} deformations, where one may see that the PCM predicts decay half-life times for ^{234,246}Pu with in the range of observed data for even mass $^{236-244}$Pu parents, thereby providing a testing ground for the future experimental studies on spontaneous fission.

The relevant details on preformation P_0 and penetration P probabilities are also given in Table 6.4 for the preferred fragments in the SF decay of $^{234-246}$Pu parents. Again the choice of most probable fission fragments for all the parents indicate the significance of shell closure effects. Hence, the present study reveals the significance of shell effects of emitting fragments in all even-mass $^{234-246}$Pu isotopes.

Finally, a comparative study of heavy-ion induced versus spontaneous fission is investigated for decay of ^{244}Pu nucleus. In Fig. 6.16 (a), we compare the calculated fragment formation yields P_0 for ℓ=0 $\hbar$ case to see the role of magic shells in mass distributions. Both processes are found to show a similar pattern in terms of the emission of most probable fragments, thereby indicating shell closure property of decay fragments. In other words, the shell effects again arise here due to spherical closed shell at heavy fragment with Z_1=50 and N_1=82. The enhanced preformation factor for ^{110}Mo (and the corresponding heavy ^{134}Te fragment) confirms that it is the most favorable decay channel, independent of the type of fission process. Note that despite the change in magnitude, the fission valleys in both cases correspond to asymmetric mass fragments which in turn provide us the information concerning the structural aspects in decay of ^{244}Pu.

Next, in order to analyze the relative effect of the two fission mechanisms, the barrier lowering parameters ΔV_B as a function of mass of fission fragments are illustrated in Fig. 6.16 (b) for the decay of ^{244}Pu with deformation effects incorporated up to quadrupole

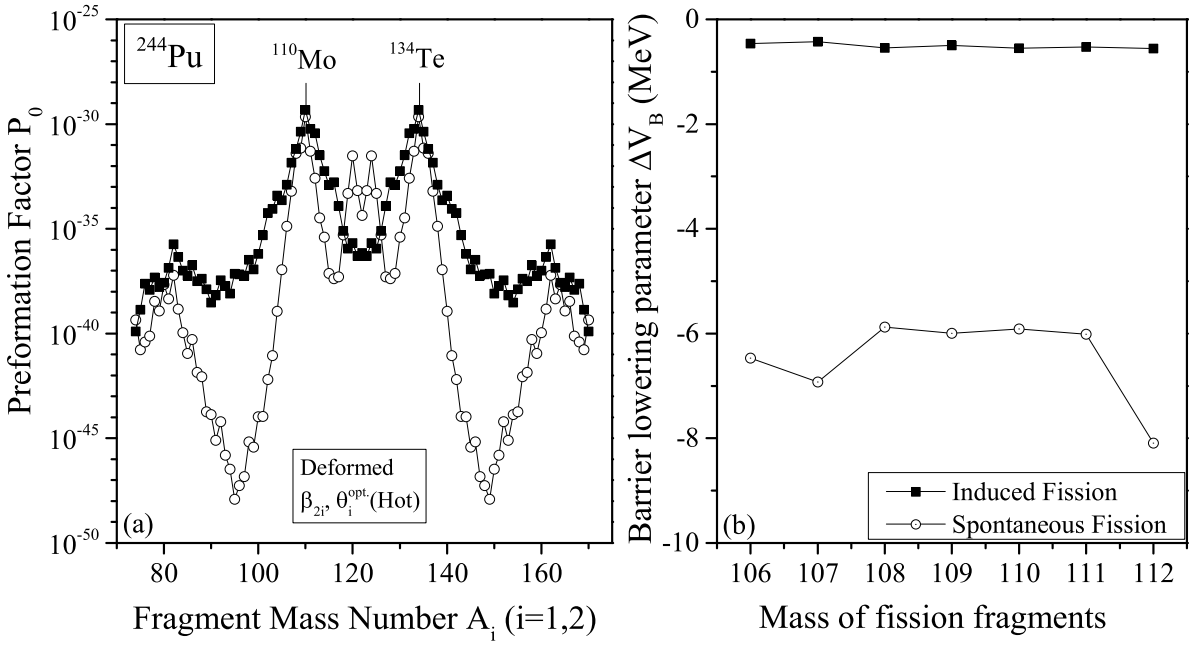

Figure 6.16 (a) Comparison of preformation factor for the spontaneous and the heavy-ion induced fission decays using hot compact configuration of β_2 deformed fragments. (b) Variation of barrier lowering parameter as a function of mass of emitted fission fragments for ℓ=0 $\hbar$ case.

deformation β_2. Note that barrier modification effect described in chapter 2 refers to an intrinsic feature of the fitting parameter ΔR, the neck-length. It is relevant to mention that the different magnitudes of ΔR's for induced and spontaneous fission processes, indicate that these processes occur at different time scales. It is evident from Fig. 6.16 (b) that, relatively larger barrier modification is needed for spontaneous fission, in comparison to that of induced one, possibly because in spontaneous decay, the fragments are in the ground state (T=0). Hence, the present study provides an ideal case to probe the explicit role of ΔV_B in fission dynamics.

6.3 Summary

The fission dynamics of two excited compound nuclei viz. ^{181}Re and ^{244}Pu are studied within the methodology of DCM. The results related to decay of these systems are divided into two parts as follows:

(i) The fission dynamics of ^{181}Re* nucleus produced in ^{12}C+^{169}Tm reaction, is ana-

lyzed and the calculations are performed for both spherical and β_2-deformed approaches of decay fragments which means that the mass distribution of $^{181}Re^*$ nucleus is worked out using spherical and deformed approaches of fragmentation and is compared with the experimental cross-sectional yield, suggesting that spherical approach gives closer comparison with the experimental data. Moreover, the fission fragments identified within DCM are in good agreement with the ones identified in experiment. The barrier characteristics such as barrier height, penetrability, etc. of the various fission fragments are investigated in terms of the isotopic and isobaric analysis so as to analyze the role of proximity, Coulomb and centrifugal potentials. The total fission cross-sections have been evaluated for both spherical and deformed choices and are found to be in agreement with the experimental data. At optimized neck-length values, the fission emission times τ_f and the respective decay widths of the identified fragments have been predicted at the three lab energies. It is observed that the value of τ_f lies in the range of 10^{-21} to 10^{-17} seconds, in agreement with the previous results. Finally, in order to analyze the comparative behavior of spontaneous and induced fission, the dynamics of ^{181}Re is examined on the basis of structural analysis of decaying fragments. Both the spontaneous fission and induced-fission dynamics show similar mass distribution. The above analysis in terms of the preformation probability, cross-section and emission time gives an overview of the decay dynamics of $^{181}Re^*$ nucleus.

(ii) The dynamics of heavy-ion induced fission is examined for the decay of excited $^{244}Pu^*$ compound nucleus. Using the DCM, the fission cross-sections are calculated over a broad range of incident energy and are found to exhibit nice comparison with the available data for the use of deformed choice of fragments. Also, the contribution of light-particles cross section σ_{LPs} is estimated with in the DCM, which comes out to be negligibly small ($\sim 10^{-5}$ barns) at all energies, as expected. Apart from the induced fission decay, we have further addressed the phenomenon of spontaneous fission (SF), i.e., to identify the most preferred fission fragments emitted in the spontaneous decays of even mass $^{236-244}Pu$ parents on the basis of PCM. The PCM estimated SF half-life times find good comparison

with the experimental data with choices of both spherical and quadrupole deformed (β_2) decay products, more so for the spherical products. In addition, the predicted SF decay half-life times for ^{234,246}Pu parents are found to lie within the range of measured values for $^{236-244}$Pu, thereby presenting new possibilities for future experiments on SF studies. The behavior of the fragmentation potential and preformation probability is also studied, which clearly stresses the significance of shell effects of emitting fragments in all the even mass Pu isotopes. Finally, in order to pin-point the comparison of spontaneous versus induced fission, the dynamics of ^{244}Pu is examined on the basis of structural analysis together with barrier characteristics. Whereas both SF and induced-fission show almost identical shell structure effects, the SF requires a larger barrier modification as compared to the heavy-ion induced fission.

Bibliography

[1] C. F. Tsang and J. B. Wilhelmy, Nucl. Phys. A **184**, 417 (1972).

[2] B. D. Wilkins, E. P. Steinberg, and R. R. Chasman, Phys. Rev. C **14**, 1832 (1976).

[3] A. Sood *et al*, Phys. Rev. C **96**, 014620 (2017).

[4] S. Sodaye, R. Tripathi, K. Sudarshan, and R. Guin, Phys. Rev. C **87**, 044610 (2013).

[5] T. N. Nag *et al*, Phys. Rev. C **96**, 044608 (2017).

[6] S. Sodaye, R. Tripathi, B. V. John, K. Ramachandran, and P. K. Pujari, Phys. Rev. C **95**, 014612 (2017).

[7] J. U. Andersen *et al*, Phys. Rev. Lett. **99**, 162502 (2007).

[8] M. Morjean *et al*, Phys. Rev. Lett. **101**, 072701 (2008).

[9] K. Kapoor *et al*, Phys. Rev. C **96**, 054605 (2017).

[10] K. Ramachandran, A. Chatterjee, A. Navin, K. Mahata, A. Shrivastava, V. Tripathi, S. Kailas, V. Nanal, R. G. Pillay, A. Saxena, R. G. Thomas, S. Kumar, and P. K. Sahu, Phys. Rev. C **73**, 064609 (2006).

[11] M. T. Senthil Kannan, J. Sadhukhan, B. K. Agrawal, M. Balasubramaniam and S. Pal, Phys. Rev. C **98**, 021601(R) (2018).

[12] R. K. Gupta, M. Balasubramaniam, R. Kumar, D. Singh, S. K. Arun, and W. Greiner, J. Phys. G: Nucl. Part. Phys. **32**, 345 (2006).

[13] R. K. Gupta, S. K. Arun, R. Kumar, and Niyti, Int. Rev. Phys.(IREPHY) **2**, 369 (2008).

[14] B. B. Singh, M. K. Sharma, and R. K. Gupta, Phys. Rev. C **77**, 054613 (2008).

[15] M. K. Sharma, S. Kanwar, G. Sawhney, R. K. Gupta, and W. Greiner, J. Phys. G: Nucl. Part. Phys. **38**, 055104 (2011); D. Jain, R. Kumar, M. K. Sharma, and R. K. Gupta, Phys. Rev. C **85**, 024615 (2012).

[16] B. B. Singh, M. K. Sharma, R. K. Gupta, and W. Greiner, Int. J. Mod. Phys. E **15**, 699 (2006).

[17] R. K. Gupta, R. Kumar, N. K. Dhiman, M. Balasubramaniam, W. Scheid and C. Beck, Phys. Rev. **68**, 014610(2003).

[18] M. Balasubramaniam, R. Kumar, R. K. Gupta, C. Beck and W. Scheid, J. Phys. G **29**, 2703 (2003).

[19] R. K. Gupta, M. Balasubramaniam, R. Kumar, D. Singh and C. Beck, Nucl. Phys. A **738**, 479c (2004).

[20] K. Sharma, G. Sawhney, M. K. Sharma and R. K. Gupta, Nucl. Phys. A **972**, 1 (2018).

[21] R. Raabe *et al*, Nature **431**, 823 (2004).

[22] P. Salvador-Castiñeira *et al*, Phys. Rev. C **88**, 064611 (2013).

[23] N. E. Holden, D. C. Hoffman, Pure Appl. Chem. **72**, 1525 (2000).

[24] R. K. Gupta, M. Balasubramaniam, R. Kumar, N. Singh, M. Manhas, W. Greiner, J. Phy. G: Nucl. Part. Phys. **31**, 631 (2005).

[25] P. Möller, J. R. Nix, W. D. Myers and W. J. Swiatecki, At. Data Nucl. Data Tables **59**, 185 (1995).

[26] R. K. Gupta, M. Manhas, W. Greiner, Phys. Rev. C **73**, 054307 (2006).

[27] H. Thierens, A. De Clercq *et al*, Phys. Rev. C **23**, 5 (1981).

Chapter 7

Summary and outlook

The present thesis is mainly focussed on the study of various radioactive decay mechanisms for a wide range of parent nuclei (with A$\sim$105-265). These ground state decay processes include α-decay, cluster emission, Heavy Particle Radioactivity (HPR) and Spontaneous Fission (SF), the details of which are explained extensively in this thesis. The whole study on ground state decays is carried out within the framework of Preformed Cluster Model (PCM). Further, the heavy-ion induced fission of fissile nuclei is also investigated with the help of Dynamical Cluster-decay Model (DCM). Both the PCM and DCM are worked out on the principle of Quantum Mechanical Fragmentation Theory (QMFT) with the deformation and orientation effects included.

The general introduction related to the mentioned decay processes is presented in Chapter 1. The regions of the periodic table which are favorable to such kind of decays are depicted in terms of Island of stability representation. In addition to this, a brief description of heavy-ion induced fission phenomenon is presented in this chapter. The role of deformations and orientations along with the applications of nuclear science to mankind is also discussed. The description of the formalism used for the fulfillment of the objectives of this thesis is given in Chapter 2. This chapter provides the information on PCM and DCM along with some relevant references of QMFT. The basic difference between PCM and DCM lies in the fact that latter is the extended version of the former

i.e. DCM is equivalent to PCM with the temperature and angular momentum effects incorporated in it.

As a first application, collective clusterization approach is employed to explore the phenomenon of α-radioactivity in Chapter 3. In this chapter, the addressal of α-cluster emission in the ground state as well as excited state decays of some trans-Sn nuclei lying near N=Z line is accomplished. First of all, the triple α-decay chain ^{114}Ba$\xrightarrow{\alpha}$^{110}Xe $\xrightarrow{\alpha}$^{106}Te $\xrightarrow{\alpha}$^{102}Sn is investigated, within the binary fragmentation approach of dynamical cluster decay model. The calculations are performed for both spherical as well as quadrupole deformed (β_2) choices of decay products. It is observed that ^{106}Te$\rightarrow$^{102}Sn+α is the most probable decay channel among the three parent nuclei in the successive α-decay chain due to the magicity of its daughter fragment. Therefore, ^{106}Te is observed as the most unstable nucleus among the three considered parent systems. Furthermore, while comparing the preformation profile of ^{114}Ba for T=0 and T$\neq$ 0, it has been observed that the spontaneous α-emission (T=0 case) exhibit symmetric fission distribution whereas the induced α-decay (T$\neq$0 case) shows relatively asymmetric mass distribution in the fissioning region. Moreover, the most probable fragment in lower mass region changes from ^{4}He to ^{6}Li as one moves from ground state to excited state decays possibly because of the dissipation of shell effects at higher temperature values. Next, the α-decay half-lives of some parent nuclei lying in the trans-Sn region are calculated using different nuclear proximity potentials. The barrier profiles investigated for the use of six different proximity potentials, concluded that Prox77, Prox00 and ProxNgo80 acquire the higher barrier heights in comparison to that of other considered potentials. On analyzing the potential energy surfaces using Prox77, Prox00 and Prox Ngo80, it is observed that, although some change in magnitude of fragmentation potential is evident, the structure remains almost similar for the use of above mentioned interaction potentials. ^{4}He is found to compete with ^{1}H for all the ground state nuclei considered in the present study. The reported α half-lives for nuclei from ^{105}Te to ^{112}Xe find nice agreement using Prox00, whereas Prox Ngo80 seems to provide a favorable option for the decay of nuclei above ^{112}Xe.

After exploring α-decay within the framework of PCM, cluster emission in view of Sn-radioactivity is explored using collective clusterization approach of PCM in Chapter 4. Here, the effect of deformations and orientations is investigated in reference to the ground-state clusterization of $^{108-116}$Xe, $^{112-120,146}$Ba, $^{116-124,152}$Ce, $^{120-130,156}$Nd, $^{124-130,160,162}$Sm and $^{128-136,166}$Gd nuclei using the PCM. Since, cluster radioactivity is a spontaneous decay process, the deformations are used upto quadrupole (β_2) with optimum cold orientations. The deformations and orientations seem important for the study of Sn-radioactivity because after incorporation of such effects, the fragmentation and scattering potentials get modified considerably. It is found that cluster half lives reduce significantly after the inclusion of deformation effects. Hence, it is observed that the consideration of deformed choice seems to provide a favorable option to deal with the decays leading to ^{100}Sn and ^{132}Sn daughter nuclei. The neutron-deficient parents have been observed to emit $\alpha-$like, A_2=4n clusters (for complementary daughter fragment ^{100}Sn), whereas the neutron-rich radioactive nuclei decay via emission of A_2=4n+2 clusters (non $\alpha-$like) independent of the choice of fragmentation. In addition to this, it is also concluded that the decays forming ^{100}Sn as daughter product are more probable as compared to the decays leading to ^{132}Sn daughter fragment in view of cluster radioactivity phenomenon, possibly because of their higher P_0 and P values and corresponding lower half-lives. Apart from the quadrupole (β_{2i}) deformations, an attempt is made to study the effect of higher-multipole deformations (upto hexadecapole i.e. β_{2i}, β_{3i}, β_{4i}) with cold compact orientations of nuclei in context of fragmentation path and barrier characteristic behavior. The spherical and β_2-deformed approaches acquire minima at 4n or 4n+2 clusters but large variation/fluctuations are seen in the potential energy surfaces for the consideration of the deformations upto β_{4i}. This clearly indicates the importance of deformation effects in cluster decays of nuclei involved in Sn-radioactivity process. Further, the effect of different nuclear proximity potentials is also analyzed in reference to fragmentation potential representing the nuclear structure effects. It is observed that Prox77, Prox88 and Prox00 exhibit similar structural pattern in the fragmentation profile. Additionally, in order to extract the further descrip-

tion on the structural behavior involved, the contribution of shell effects is examined via preformation profile which reveals that the shell effects (δU) are one of the vital factor that decides the decay dynamics of cluster emission process.

After analyzing cluster radioactivity of the ground state parent nuclei, the structural aspects and barrier characteristics of parent and daughter nuclei are probed in context of spontaneous fission phenomenon in Chapter 5. Here, spontaneous fission of 45 ground state parent nuclei, varying from ^{232}U to ^{264}Hs is studied using PCM for spherical choice of fragmentation. Here, PCM is applied in reference to spontaneous fission (SF) process and its possible competing analysis with other ground state decays such as $\alpha-$, cluster, HPR, etc. is also explored. The PCM reported SF half-lives for all the considered systems find good agreement with experimental data, while using different choices of radius, namely effective sharp radius and S*ü*ssmann's central radius. The most probable decay fragments have been identified and the fragments in the mass range A_2 = 98-130 (plus complementary heavy fragments) seem to be the prominent contributors towards SF half-lives for all the chosen cases. Various issues related to shell effects, fine structure/sub-structure of fission fragments, isospin effect, etc. have been addressed. Furthermore, the decay path of even mass nuclei $^{232-238}$U, in terms of α-emission along with most probable cluster decay(s) is investigated in order to identify the magic or near magic daughter(s) in the radioactive emission process. This study exhibits two important results: (i) the prominence of heavy cluster ^{82}Ge and its corresponding daughter is found equally favored in all the chosen parents, thereby pointing out some future possibilities for the experiments on heavy-particle radioactivity. (ii) the behavior of neck length parameter indicates that a particular decay mode occurs almost simultaneously in the decay of different U isotopes. Therefore, this result could be of interest to probe various ground state decays and provide new directions for future measurements.

Besides the PCM applications in ground state α-, cluster and fission decays, next the heavy-ion induced fission of heavy nuclei is worked out in Chapter 6. In this chapter, the fission dynamics of two excited compound nuclei viz. ^{181}Re* and ^{244}Pu* are studied within

the methodology of DCM. The results related to decay of these systems are divided into two parts as follows:

(i) Firstly, the fission dynamics of $^{181}Re^*$ nucleus formed in $^{12}C+^{169}Tm$ reaction is addressed for both spherical as well as β_2-deformed choices of fragmentation. The mass distribution of $^{181}Re^*$ nucleus is analyzed for both the spherical and the deformed approaches of fragmentation and then, compared with the experimental cross-sectional yield. It is observed that the spherical approach gives nice comparison with the experimental data. Moreover, the fission fragments identified within DCM are in good agreement with the ones recognized in experiment. The barrier parameters like barrier height, penetrability, barrier modification etc. of the identified fission fragments are evaluated and displayed in terms of the isotopic and isobaric analysis. The total fission cross-sections for both spherical and deformed choices are found to be in agreement with the experimental data. Moreover, the fission emission times τ_f and the respective decay widths of the identified fragments have been predicted at optimized neck-length values. The value of τ_f is found to lie in the range of 10^{-21} to 10^{-17} seconds which is in line with the previous results. Finally, the dynamics of ^{181}Re nucleus is examined on the basis of structural analysis of decaying fragments in order to analyze the comparative behavior of spontaneous and induced fission processes. For both the T=0 and T$\neq$0 dynamics of ^{181}Re nucleus, almost similar fission mass distribution is obtained. This analysis in terms of the preformation probability, cross-sections and emission times gives an overview of the decay dynamics of ^{181}Re nucleus.

(ii) Secondly, we study the dynamics of heavy-ion induced fission for the decay of excited $^{244}Pu^*$ compound nucleus. In this work, the fission cross-sections have been calculated using collective clusterization approach of DCM over a wide range of incident energies and are found to exhibit good comparison with the available data. The contribution of light-particles (Evaporation Residues) cross section σ_{LPs} is also estimated, which comes out to be negligibly small ($\sim 10^{-5}$ barns) at all energies. Beside this, for the fissile nucleus Plutonium, experimental data on spontaneous fission is available in literature,

therefore, SF is also investigated so as to compare the induced and spontaneous fission processes. Another objective to analyze SF of Pu is to identify the most probable fission fragments emitted in the ground state decays of even mass $^{236-244}$Pu parents; which are not detected experimentally yet. The PCM calculated SF half-lives find nice comparison with experimental data with choices of both spherical and quadrupole deformed (β_2) decay products, more so for the spherical products. Due to non-availability of SF half-life data of ^{234,246}Pu parents, predictions are given for these nuclei which are found to lie within the range of measured values for $^{236-244}$Pu; thereby providing the future options for performing corresponding experiments. The structural behavior is also studied via fragmentation potential and preformation probability curves, which clearly imparts the importance of shell effects of decay fragments in all the even mass Pu isotopes. Finally, the dynamics of ^{244}Pu is examined on the basis of structural analysis and barrier characteristics in order to pin-point the comparison of spontaneous versus induced fission. Both SF and induced-fission show similar shell structure effects; the SF requires a larger barrier modification as compared to one for heavy-ion induced fission.

Concludingly, on compiling the above results of PCM and DCM, this thesis presents an extensive and comprehensive analysis of various ground state and excited state decay mechanisms. However, every research work can possibly be extended in many ways by employing new ideas so as to make it more worthwhile and applicable. This work can be further extended by investigating more ground state decay mechanisms such as proton radioactivity and neutron radioactivity. The decay modes (especially α-decay and spontaneous fission) studied in present work can be tested by considering the deformations upto hexadecapole (i.e. β_2 to β_4) within the framework of PCM. The study of α-decay within collective clusterization method (studied here trans-Sn region) can be extended to other mass regions of periodic table as a future assignment. Furthermore, it will be interesting to explore the comparison of ground state and excited state decay processes such as cluster emission versus IMF production and heavy particle radioactivity versus HMF in the excited state decay.